Quantum Dynamics of Condensates, Atomtronic Systems, and Photon Fluids

by

Brian Thomas Seaman

B.S., Rowan University, 2003

A thesis submitted to the

Faculty of the Graduate School of the

University of Colorado in partial fulfillment

of the requirements for the degree of

Doctor of Philosophy

Department of Physics

2008

This thesis entitled:
Quantum Dynamics of Condensates, Atomtronic Systems, and Photon Fluids
written by Brian Thomas Seaman
has been approved for the Department of Physics

Prof. Murray Holland

Prof. Victor Gurarie

Date

The final copy of this thesis has been examined by the signatories, and we find that both the content and the form meet acceptable presentation standards of scholarly work in the above mentioned discipline.

Seaman, Brian Thomas (Ph.D.)

Quantum Dynamics of Condensates, Atomtronic Systems, and Photon Fluids

Thesis directed by Prof. Murray Holland

In the first part of this thesis, the dynamics of interacting ultracold bosonic atomic gases trapped in an optical lattice are examined from the perspective of nonlinear band theory. The mean-field Gross-Pitaevskii equation is used to model the Bloch waves for weakly and strongly interacting gases with a Kronig-Penney potential, i.e. a lattice of delta functions. The appearance of looped swallowtail structures in the energy bands is a highly nonlinear effect. These swallowtails are then related to period-doubled Bloch states by examining a two-color lattice. A stability analysis shows that the effective mass of the atoms is a main feature describing the stability properties of the system.

In the second part of this thesis, the dynamics of atomtronic systems, ultracold atom analogs of semiconductor devices, is examined. Atomtronic systems are first presented from the perspective of the fundamental building blocks needed to create a circuit. An atomtronic battery creates a chemical potential difference. An optical lattice can play the role of a wire in electronics. The combination of N-type and P-type semiconductors lead to an atomtronic diode. The physics behind this device are due to a transition between superfluid and insulating states for the atomic device, contrary to the workings of an electronic diode. An atomtronic transistor is also presented.

In the third part of this thesis, the method of evaporative cooling is applied to a photon fluid confined to a nonlinear Fabry-Perot cavity. A photon fluid is a collection of interacting photons that exhibit fluidic hydrodynamic properties. The effects of photon recombination due to atom-mediated interactions and evaporation with an energy dependent reflectivity of the cavity lead to Bose amplified stimulated emission into the lowest energy mode.

Dedication

To my Rachel, my wife, companion and best friend, without whom this would never have been possible.

Acknowledgements

I would like to take this time to acknowledge all of the people who have helped me to get to where I am. First, my advisor Murray Holland has given me both the independence and the guidance necessary to stimulate my many interests in physics. Many other people have had a hand in contributing to this thesis including Jinx Cooper, Dana Anderson, Hong Ling, Lincoln Carr, Simon Gardiner, Meret Krämer, Dominic Meiser, Rajiv Bhat, Satyan Bhongale, Rob Chiaramonte, Brandon Peden, Josh Milstein, Kang-Kuen Ni, Ron Pepino, Dave Tieri, and Jochen Wacter. Several others have always been available for an engaging conversation that has helped to shape my view of the world including Nrupen Baxi, Amar Doshi, John Ferro, Tom Joad, Glenn Koslowsky, Anthony Leone, and John Lombardini.

Contents

Chapter

Figures

Figure

Chapter 1

An Introduction to Atom-Photon Interactions

With the creation of a Bose-Einstein condensate with a trapped atomic gas in 1995 [6, 39, 19], a new and diverse field of physics reliant on the ultracold properties of bosons was born. The quantum statistics of bosons lead to the occupation of a single quantum state at ultracold temperatures. Many properties, such as superfluidity and phase coherence, become experimentally accessible with these new systems. In this thesis, we examine three areas of this field of ultracold bosonic systems: the nonlinear band structure of interacting atoms confined to an optical lattice potential, the creation of atomtronic systems analogous to electronic semiconductor devices, and the evaporative cooling of a photon fluid to quantum degeneracy. These three works are connected by several over-arching themes. The fundamental particles under examination are ultracold bosons. Each system is inherently dynamical, whether considering the motion of atoms or of photons. And finally, the ability to control the interactions between atoms and light make all three systems possible.

This introduction covers several of the important topics necessary to analyze the three areas of examination. The use of atom and photon interactions to control each of these bosonic species is discussed. The properties and creation of a Bose-Einstein condensate is then examined, followed by an analysis of a trapping optical lattice potential. The system of a photon fluid is then introduced.

1.1 Atom-Photon Interactions

The interactions between atoms and light are fundamental to nearly all fields of physics. It is common to view these interactions through one of two lenses. Either light alters the properties of the atoms or atoms alter the properties of the light. There are several ways of examining the atoms and photons: classically, semiclassically, or quantum mechanically. The system under consideration usually dictates the appropriate method of examination.

For many physical systems, the fields of light do not need to be considered in full quantum mechanical detail and can be instead accurately described as classical fields. Classical fields are characterized solely by Maxwell's equations with the appropriate boundary conditions and this description is generally a valid approximation [83]. The presence of atoms then allows for the light to behave in new ways due to the atoms' polarization or magnetization. For instance, a nonlinear medium instigates the process of four-wave mixing for light driven by strong pump fields [110]. Two pump fields of the same frequency but opposite direction drive a nonlinear medium and with the aid of a weak probe field create a sideband component. The laser is another excellent example of how atoms can be used to enhance the properties of photons [148]. An active gain medium inside a mirrored cavity enhances the effects of stimulated emission and creates a high intensity coherent beam of light.

A fully quantized view of light is necessary to understand many phenomena. For instance, the details of spontaneous and stimulated emission depend crucially on the quantum nature of light [110]. Emission is the process of creation of a photon by loss of energy by an atom. Stimulated emission is the enhancement of photon creation of a particular mode, due to the presence of additional photons in the same mode, with the same phase. The bosonic nature of photons play a large role in this effect. The quantum nature also frequently appears in the noise profile of the light in phenomenon

like resonance fluorescence [91, 90] and squeezing [159].

Atom-field interactions can also lead to mechanical effects on atoms such as the Doppler cooling of atoms [100]. In laser cooling, the moving atoms see a Doppler shifted field of light. For a red-detuned laser, atoms moving against the light's direction will have an enhanced interaction strength. Laser cooling is one of the traditional methods used to cool atomic gases into quantum degeneracy.

The creation of an optical lattice is another example of how light can be used to control the motion of atoms [62]. Counter-propagating lasers create a sinusoidal standing wave intensity pattern and due to the AC Stark shift have the effect of establishing an external periodic potential for the atoms. The use of an optical lattice has led to the experimental verification of the Mott-insulator superfluid transition [85, 64].

This thesis examines the nonlinear interactions of light and atoms from both perspectives. In the first two systems, atom-atom interactions are enhanced by the presence of an optical lattice. The effects of increased interactions on the energy band structure is examined and new features are found. The interactions are also used to create atomic analogs of electronic devices replicating the motion of electrons in a solid. In the final system, a nonlinear atomic medium inserted in a Fabry-Perot cavity creates an effective interaction between photons. This system can reach quantum degeneracy via a process analogous to evaporative cooling of atomic gases.

1.2 Bose-Einstein Condensates

The observation of Bose-Einstein condensation (BEC) of alkali-metal atoms in 1995 [6, 39, 19] confirmed predictions that Bose and Einstein first developed for noninteracting bosons in 1924 [16, 47]. A Bose-Einstein condensate is created when the de Broglie wavelength of the bosons is larger than the average interparticle spacing, leading to a macroscopic occupation of a single quantum state. This is a low temperature phase transition that is only accessible to bosons and not fermions, due to the differences in

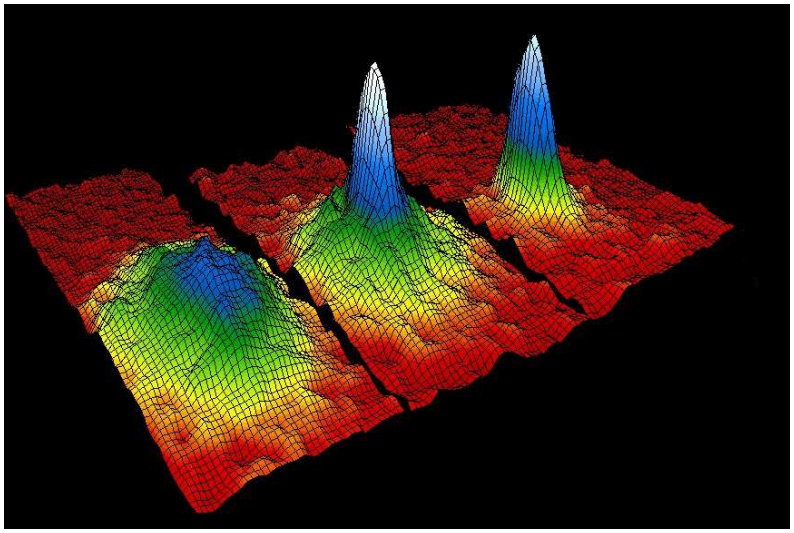

Figure 1.1: The velocity distribution of ultracold rubidium atoms after an expansion performed at JILA [6]. From left to right, the temperature of the system is decreased from $400nK$ to $50nK$, and a condensate - a macroscopic population of the ground state - appears. The left most frame has a negligible condensate fraction since it is just above the transition temperature. In the right most expansion, nearly all of the atoms are condensed, corresponding to the sharp peak.

their quantum statistics.

In atomic systems, Bose-Einstein condensation was first observed for rubidium, sodium, and lithium atoms but has later gone on to include many other atomic species. The atoms are first collected in a magneto-optical trap and then cooled to micro-Kelvin temperatures [100]. Evaporative cooling in a magnetic trap leads to temperatures in the nano-Kelvin range. Condensed atoms can number well into the millions.

After cooling, the velocity distribution of the atoms can be examined by performing a time-of-flight analysis. Figure 1.1 presents the velocity distributions for systems with three different temperatures, just above the transition temperature at $400nK$ and two below the transition temperature at $200nK$ and $50nK$, as presented by the team at JILA [6]. At the lowest temperature, nearly all of the atoms have been condensed and the strong peak corresponds approximately to the velocity distribution of the harmonic oscillator ground state.

Before the examination of atomic gases, superfluid liquid Helium was the first system that was thought to exhibit properties of a Bose-Einstein condensate [87, 3, 103]. As a liquid, the effects of interactions in the superfluid Helium are considerable. This is in contrast to the new atomic gas systems, in which interaction effects can be quite small. This property of weak interactions has allowed for the control of many of the system parameters and examination of interesting new phenomena. Since the atoms are at very low temperatures, a single parameter, the s-wave scattering length, can usually be used to characterize inter-atomic interactions. In several current BEC systems, the interactions can be made repulsion and attraction using magnetically tunable Feshbach resonances [81]. A Feshbach resonance occurs when the energy of a bound state of the interatomic potential equals the kinetic energy of two incoming atoms. The relative energy of the bound state can be controlled by an external magnetic field and has the effect of dramatically increasing the s-wave scattering length. The sign of the scattering length can also be altered.

Bose-Einstein condensates exhibit several interesting properties. For instance, the gases are superfluid and sustain quantized vortices [65]. A superfluid has zero viscosity and sustains frictionless flow. The formation of quantized vortices is another manifestation of superfluidity. Below a critical rotation rate, the condensate will remain stationary. However, a faster rotation causes the superfluid to rotate around vortex cores. Each vortex core can be described by discrete amounts of angular momentum.

Current work is being performed trying to create Bose-Einstein condensation in new systems. Molecular BECs have been created by tuning a Feshbach resonance to create ultracold molecules from condensed atoms [44]. Quantum degenerate fermions have been coaxed into pairing in ways similar to Cooper pairing [131]. Since the fermions are at very low temperatures, the Cooper pairs are also created in a quantum degenerate state. The pairs, however, are effectively bosons and so they create a “fermionic condensate”.

A Bose-Einstein condensate, confined to an optical lattice as described in the following section, will be the primary system of interest for the first two parts of this thesis. The final part describes how methods traditionally associated with atomic condensates, such as evaporative cooling, can be used to create a quantum degenerate set of photons, a condensed and superfluid state of light.

1.3 Optical Lattices

The use of lasers has led to the creation of many new tools to control, manipulate and examine atoms. One such useful tool is an optical lattice that has been developed to examine and alter the properties of ultracold atomic gases [82]. An optical lattice is created by aligning counter-propagating lasers to form a sinusoidal intensity profile. This intensity pattern creates a sinusoidal AC Stark shift that acts as an external periodic potential for the atoms. Since the parameters of the laser, such as intensity and polarization, are easily tuned, the optical lattices that are formed can be easily manipulated [62]. Atoms are generally loaded into an optical lattice by first forming a Bose-Einstein condensate using traditional methods. The lattice is then created by adiabatically turning on and increasing the laser intensity.

Bose-Einstein condensates of atomic gases are generally weakly interacting since they are created at very low densities. Therefore, the effects of interactions are usually not very prominent. An optical lattice can be used to convert the weakly interacting condensate into a strongly correlated gas by simply increasing the laser intensity. This causes a greater localization of the atoms into the lattice wells. The greater localization is able to increase the effects of interactions compared with the kinetic energy associated with moving from one lattice site to the next.

Ultracold atoms in an optical lattice exhibit many interesting properties. They are particles in a periodic potential and so exhibit a gapped energy band structure. The energy structure of a many-particle system can also exhibit a gapped band structure as it

is the condensate wave function that is in the presence of an effective potential due to the lattice and interactions [105]. For large interactions, new features are shown to appear, such as the occurrence of looped swallowtail structures in the energy band [153, 154]. Ultracold atoms in optical lattices allow for the examination of both attractive and repulsive interactions due to the alterability of the sign of the s-wave scattering length with a Feshbach resonance.

The effects of strong interactions and strong correlations present themselves in other ways [85]. For instance, ultracold atoms exhibit a quantum phase transition as the lattice depth is increased. For a shallow lattice, the effects of the potential are negligible and the atoms remain a condensate with a well defined system-wide phase. This is the superfluid phase of the gas. As the depth is increased, the atoms become localized in separate wells. For deep enough lattices, the phase in each well is independent of the others. In addition, the hopping of atoms from one site to the next becomes severely restricted and the Mott-insulator phase is formed. When the atoms are in a Mott insulator state, each well contains on average an integer number of atoms. The number variance on each site decreases quickly as the well depth increases.

The Mott insulator to superfluid transition was clearly demonstrated in an experiment by Greiner, et. al. [64], in which the interference pattern of atoms trapped in an optical lattice shows a transition from a phase coherent state to a state with no global phase coherence, as seen in Fig. 1.2. The figure presents eight different lattice depths, increasing from $0E_R$ to $20E_R$, where E_R is the recoil energy of the photons in the lattice. The interference pattern shows an initially coherent system lose its phase coherence as the superfluid transitions into a Mott insulator. Another feature of the phase transition is that, for a system with a small hopping energy, there is a jump in chemical potential of a system with slightly less than integer filling to a state with slightly higher than integer filling. The gap is on the order of the interaction energy and leads to regions where the system is unaffected by changes in the chemical potential. This transition is

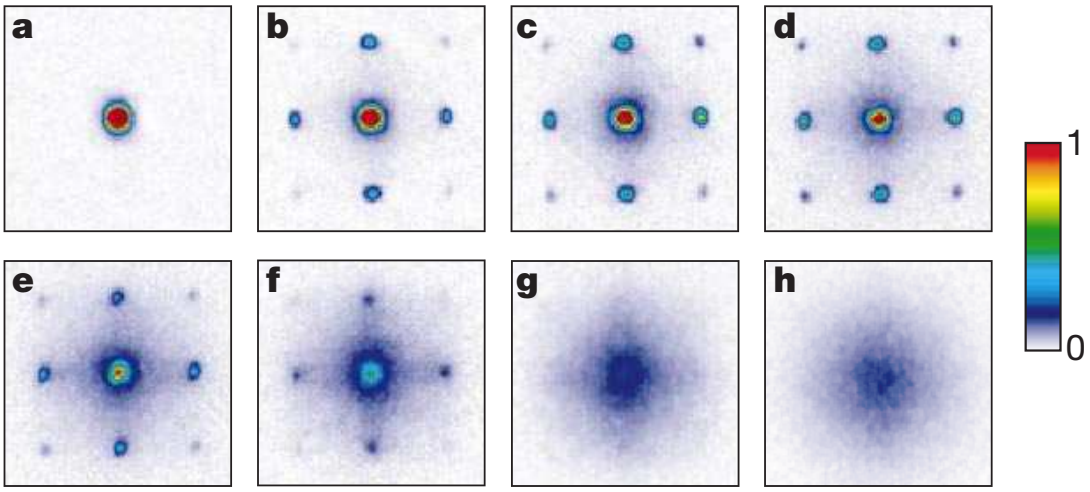

Figure 1.2: The velocity distribution of ultracold rubidium atoms trapped in an optical lattice after an expansion performed by Greiner, et. al. [64]. From (a) to (h), the lattice depth is increased from $0E_R$ to $20E_R$, where E_R is the atomic recoil energy due to the lattice lasers. Initially, the atoms all have a similar momentum and are a collectively a superfluid state. As the lattice depth is increased, additional momentum peaks form due to the interference patterns of partially localized atoms. A single phase still defines the entire system. Further increases in the lattice depth eventually lead to a system with no phase coherence.

an integral component to the workings of the atomtronic devices that will be discussed.

1.4 Photon Fluid

A photon fluid is a way to describe photons with atom-mediated interactions [33] and is in general a system of photons that exhibit hydrodynamic properties. Atom mediated photon-photon interactions can be obtained for light trapped between two parallel mirrors placed close together in the presence of a nonlinear medium. The nonlinear polarizability creates the higher order interaction effect. A linear polarizability creates only an energy shift of the bare modes. The nonlinear medium can be any of a number of substances. For instance, a nonlinear crystal deposited onto the mirrors or a Rydberg gas could be used. The sign of the interactions depends on whether the cavity mode is red or blue shifted relative to the closest atomic transition. The mirrors

forming the cavity cannot be perfectly reflecting so the system must be continuously pumped. The pumping rate and loss rates set the number of photons in the system.

A photon fluid, or weakly interacting photon gas in the nonlinear Fabry-Perot cavity, is an effectively two dimensional system if excitations to higher longitudinal modes are minimized. The reduced dimensionality and small transverse momenta lead to an effective mass, $m \equiv \hbar\omega/c^2$, determined by the frequency of the lowest longitudinal mode. This effective mass is due to the tight confinement in one direction and the relatively free movement in the other directions and will be presented in more detail in Chapter 5. A photon fluid can have interesting properties, especially at low temperatures. Although the system is composed of photons, the chemical potential does not vanish due to the interactions. The energy required to put a photon in the cavity depends on the number of photons already in the cavity. This is in stark contrast to the traditional Planck blackbody photon system in which the chemical potential vanishes.

For low temperatures, since the system is composed of weakly interacting bosons, the photons should populate the lowest energy mode with a macroscopic occupation. The number of photons in this mode will be determined by the intensity of the pumping. The excitation spectrum for the ground state of the fluid is given by the Bogoliubov dispersion relation [100]. For small momenta, the dispersion relation is linear. This implies that elementary excitations are phonon modes, i.e. that sound-like waves can propagate through the photon fluid. The presence of phonon modes means that different long wavelength excitations can propagate together without distortion. For larger momenta, the dispersion relation becomes quadratic. These excitations behave like free nonrelativistic particles with a finite mass. For a completely non-interacting system, the dispersion relation does not have the linear component and is instead only quadratic in nature. The interactions are critical to the linear aspect of the dispersion relation. The Bogoliubov form of the dispersion relation implies that the system is superfluid and should support dissipationless flow and quantized vortices [38].

In this thesis, it is shown how a quantum degenerate photon fluid can be created using the method of evaporative cooling in which the highest energy photons leave the system.

1.5 Overview

Chapter 2 presents the theory of an optical lattice. It is shown how the AC Stark shift due to the interference pattern of counter-propagating electromagnetic fields can create a periodic lattice potential. The energy band structure of non-interacting atoms is described. The many-atom second-quantized Hamiltonian is introduced and two models or approaches, the Bose-Hubbard Hamiltonian and the Gross-Pitaevskii equation, are presented.

Chapter 3 examines the properties of interacting atoms confined to a periodic potential. This study uses the mean-field Gross-Pitaevskii equation with a Kronig-Penney potential to model the system. The complete set of stationary solutions to the single boundary problem, step potential or localized delta function potential are presented. These states are the nonlinear equivalents to transmitted and reflected waves. The Bloch states calculated from the Kronig-Penney potential are compared to other methods for calculating stationary states in lattices. The presence of swallowtails is then connected to period-doubled states of a two-color lattice.

Chapter 4 presents the concept of atomtronics, in which ultracold atom analogs play the role of traditional semiconductor devices. The tight binding Bose-Hubbard model is used to model the dynamics of the atoms as they flow through the lattice configurations. The quantum phase transition between the Mott insulator and superfluid phase is a key component to the workings of the atomtronic devices. Key electronic analogs are presented, such as the connection between electronic charge and presence of atoms. Atomtronic semiconductors are connected to form an atomtronic diode and transistor.

Chapter 5 presents a Hamiltonian that describes the atom-mediated photon-photon interactions that occur in a Fabry-Perot cavity filled with a nonlinear medium. The presence of the photons polarizes the nonlinear medium, which then has a back effect on the photons. The interactions lead to the concept of a photon fluid in which the presence of Bogoliubov excitations implies the existence of a superfluid state of light.

Chapter 6 presents a method for evaporatively cooling a photon fluid to quantum degeneracy. The five key processes that occur in the system are described in detail. The cavity is constantly pumped by an incoherent broad spectrum source. Photons trapped in the cavity slowly decay through the mirrors. Photons self-interact to create a mean field energy shift. Photons recombine to form new photon modes. Finally, high energy photons quickly leave the cavity either out the cavity sides or due to a frequency dependent reflectivity of the mirrors. The photons quickly populate the ground state mode and possess a nearly Poissonian number distribution. The spectral width of the system is analyzed to show a narrow spectrum and long coherence time.

Chapter 2

Interacting Atoms in an Optical Lattice

In current experiments with Bose-Einstein condensates, the densities, ρ, are generally low compared to interaction scattering lengths, a_s, $\rho a_s^3 \ll 1$, so that the system is weakly interacting. Many interesting properties of condensates, however, occur for large interactions and strong correlations. There are several ways in which the effects of interactions can be enhanced. The use of a Feshbach resonance, in which an external magnetic field can be used to tune the two-body interactions, has provided many new avenues of exploration [81]. The confinement of atoms in an optical lattice, formed by the AC Stark shift due to counter-propagating lasers, has also allowed for the effects of interactions to be enhanced [85]. The quantum phase transition between the Mott insulator and superfluid phases observed in optical lattices has been an impressive demonstration of the effects of strong interactions [52, 64]. Atoms are usually loaded into optical lattices by first condensing the atomic system into a condensate and then adiabatically increasing the intensity of the lasers that form the optical lattice. Optical lattices have also been used to trap and cool atoms and ions [75, 66]. The use of ions in an optical lattice present an interesting opportunity to create a quantum registry for a quantum computer.

Atoms confined in optical lattices open many possibilities for exploration. The similarity of cold atoms in an optical lattice to electrons in a solid can be leveraged to explore phenomena associated with condensed matter systems. Optical lattices have

several advantages over electronic systems. The structure and geometry of an optical lattice can be very well controlled and are largely free of unintended defects. These properties are utilized in the following two chapters to describe the nonlinear band structure of atoms in a lattice and to reinterpret electronic systems in the context of ultracold atoms.

This chapter first presents the Hamiltonian of a single atom in the presence of a monochromatic field and introduces the origin of an optical lattice. The energy structure of the atom is presented. This Hamiltonian is then extended to a many-body system and a second-quantized Hamiltonian is presented. It is difficult to directly perform calculations with the second-quantized Hamiltonian, and so several approaches are commonly taken. This chapter then presents two models that are used to describe the properties, both stationary and dynamic, of a dilute gas of atoms confined in an optical lattice. The Gross-Pitaevskii equation, a mean field theory that well describes the condensate wave function for large particle numbers, is presented, as well as the Bose-Hubbard model which describes atoms in well separated lattices sites for large lattice depths.

2.1 Single Atom Hamiltonian

An optical lattice is created by interactions between atoms and light. A gas of neutral atoms, traditionally alkali-metal due to ease of manipulation, loaded into sets of counter-propagating laser beams experience a sinusoidal potential. The primary mechanism controlling the potential is the AC Stark shift between a single atom and the field of light. This section explores the Hamiltonian of a single atom interacting via the optical dipole potential with a monochromatic field of a large number of photons.

2.1.1 AC Stark Shift

The atom is considered a two-level system with a dipole moment between the internal states and is confined to a fixed volume V. The internal atomic states are labeled

$|g\rangle$ and $|e\rangle$ for the ground and excited states, with energies $\hbar\omega_g$ and $\hbar\omega_e$, respectively. The electric field will be considered classically, and given by a monochromatic plane wave,

$$\vec{E}(\vec{r},t) = \vec{\varepsilon}E(\vec{r})\cos(\omega t)\,, \tag{2.1}$$

where $\vec{\varepsilon}$ is the polarization of the field, $E(\vec{r})$ contains the spatial dependence of the field and ω is the frequency of the field. The Hamiltonian that describes the internal states of the atom, with a position of $\vec{r}$, and the electric field is given by

$$\hat{H}_0 = \hbar\omega_g|g\rangle\langle g| + \hbar\omega_e|e\rangle\langle e| - dE(\vec{r})\cos(\omega t)\,, \tag{2.2}$$

where $d \equiv \langle e|e\hat{r}|g\rangle \cdot \vec{\varepsilon}$ is the dipole moment of the atom in the direction of the electric field. Note that the dipole approximation has been employed which is valid as long as the wavelength of the field is much larger than the size of the atom. The frequency difference between the internal states is defined as $\omega_0 \equiv \omega_e - \omega_g$. The detuning of the photon frequency with the atom energy difference is given by $\Delta \equiv \omega - \omega_0$.

When the photons are near resonant with the atom energy difference, $|\Delta| \ll \omega_0$, the rotating wave approximation can be used to eliminate off-resonant interactions. The Hamiltonian in the interaction picture becomes

$$\hat{H}_I \approx \frac{\hbar\Omega(\vec{r})}{2}|e\rangle\langle g|e^{i\Delta t} + \frac{\hbar\Omega^*(\vec{r})}{2}|g\rangle\langle e|e^{-i\Delta t}\,, \tag{2.3}$$

where the Rabi frequency is given by,

$$\Omega(\vec{r}) = \frac{dE(\vec{r})}{\hbar}\,. \tag{2.4}$$

The lack of a permanent electric dipole moment means that there is no first order energy shift. However, the field can induce a dipole, which in term interacts with the light to create the energy shift. If the detuning is large compared to the Rabi frequency, $|\Omega| \ll |\Delta|$, then second order perturbation theory can be used to determine the AC Stark shift,

$$\Delta E = \pm\frac{|\langle e|H_I|g\rangle|^2}{\hbar\Delta} = \pm\hbar\frac{|\Omega(x)|^2}{4\Delta}\,. \tag{2.5}$$

The plus sign of the energy shift corresponds to the energy change of the ground state, while the minus refers to the excited state energy shift. It is the spatial dependence of the Rabi frequency, and hence the spatial intensity of the light, that allows for a spatially dependent external potential. This is utilized to create an optical lattice. Note that for blue detuning, $\Delta > 0$, the ground state atoms will prefer to occupy a minimum in the laser intensity, while for red detuning, $\Delta < 0$, the atoms will prefer the maximum intensity.

2.1.2 Dissipation

In addition to the conservative processes that lead to the AC Stark shift, additional dissipative processes can also occur. Dissipation can be caused by spontaneous emission from the excited state. For a lattice with many atoms, interactions can also cause decay to the ground state. The effective spontaneous emission rate, due to partial occupation of the excited state, is given by

$$\Gamma_{eff} = \frac{|\Omega(x)|^2 \Gamma_{se}}{8\Delta^2}\,, \tag{2.6}$$

where Γ_{se} is the linewidth of atoms in the excited state. The effects of dissipation are therefore mitigated when the population of the excited state is kept to a minimum, and so a blue shifted lattice is preferred since this configuration places atoms in the low intensity portions of the lattice. Since the dissipation scales as Δ^{-2} and the lattice potential scales as Δ^{-1}, an off-resonant, but high intensity, laser optimizes the effects of the lattice while minimizing the effects of dissipation.

2.1.3 Optical Lattice

An optical lattice is created by aligning sets of counter propagating laser beams. The beams create a standing wave interference pattern with sinusoidal intensity and

Rabi frequency. In one dimension, the Rabi frequency becomes,

$$|\Omega(x)| = 2\Omega_0 \sin(kx)\,, \tag{2.7}$$

where $k = 2\pi/\lambda$ is the wavenumber of the light and λ is the wavelength of the light. This leads to a corresponding external potential,

$$V(x) = \frac{\hbar\Omega_0^2}{\Delta}\sin^2(kx)\,. \tag{2.8}$$

Two and three dimensional lattices can be created by using multiple sets of counter propagating lasers. In addition to the intensities, the relative polarizations of the beams can also influence the structure of the optical lattice. It is possible to create triangular, trapezoidal and rectangular lattice configurations.

A single set of counter-propagating beams can be used to create a series of flat pancake-like structures in which atoms may easily move in two dimensions but are restricted in the third. The use of two sets of beams can create a set of interacting tube-like structures in which only one direction allows easy motion. If a third set of weak intensity beams is added, an effectively one-dimensional system with a periodic potential can be created. If the beam intensity is increased, a true three dimensional lattice can be created.

2.1.4 Band Structure

One of the many important features of particles in a periodic potential is that the single-particle energy spectrum takes the form of a band structure where bands of allowable energy are separated by finite gaps. This is a feature common to all systems in which particles move in a periodic potential. There is a well-developed theory describing these effects [9].

In the case of a one dimensional system, it is possible to solve for the stationary states analytically. The Hamiltonian of an atom in an optical lattice is given by

$$\hat{H} = \frac{\hat{p}^2}{2m} + V_0 \sin^2(kx)\,, \tag{2.9}$$

where the kinetic energy of the atom has been specifically included and the periodicity of the lattice is $a \equiv \pi/k = \lambda/2$. According to Bloch's theorem [9], the eigenstates of such systems can be written as the product of a plane wave and a function periodic in the lattice spacing, as follows:

$$\phi_q^{(n)}(x) = e^{iqx} u_q^{(n)}(x)\,, \tag{2.10}$$

where

$$u_q^{(n)}(x) = u_q^{(n)}(x+a)\,. \tag{2.11}$$

The stationary Schrödinger equation, $\hat{H}\phi = E\phi$, then yields

$$\left(\frac{(\hat{p}+\hbar q)^2}{2m} + V_0 \sin^2(kx)\right) u_q^{(n)}(x) = E u_q^{(n)}(x)\,. \tag{2.12}$$

This leads to the interpretation of $\hbar q$ as the quasi-momentum of the atom since it is associated with the discrete translational symmetry of the lattice just as momentum is associated with translational symmetry of a free particle. The Schrödinger equation is simply a form of the Mathieu equation and the Bloch waves are, therefore, given by Mathieu functions [1].

The eigen-energy structure exhibits periodicity with respect to the quasi-momentum given by the reciprocal of the lattice spacing, $K = 2\pi/a$. According to Bloch's theorem, states given by $\phi_q^{(n)}(x)$ and $\phi_{q+K}^{(n)}(x)$ have the same energy $E_q^{(n)}$. Therefore, it is only necessary to examine the energy diagram in the restricted quasi-momentum domain of $-\pi/a < q < \pi/a$. All other quasi-momenta map back into this restricted region.

Figure 2.1 presents the band structure for various lattice depths of a one dimensional lattice and tight confinement in the remaining two directions. For a vanishingly small lattice, the atoms possess the traditional quadratic free particle spectrum. As the lattice depth is increased, a gap appears between bands. Initially the gap at the edges of the Brillouin zone of the first band is given by $V_0/2$. The gap increases as the lattice depth increases and the energy band width shrinks. Interesting new features will appear for interacting systems.

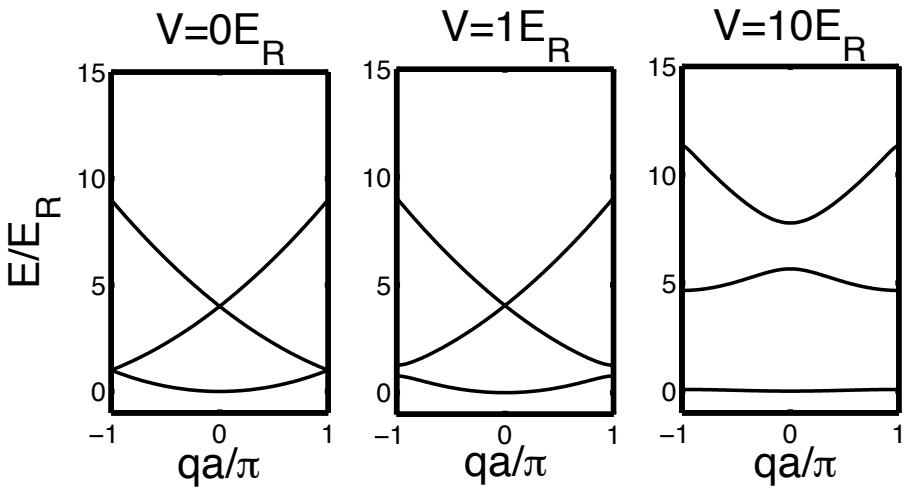

Figure 2.1: Band structure for an atom confined to a one dimensional optical lattice. For small lattice depths the energy structure has a nearly free-particle quadratic spectrum. Increased lattice depth creates gaps between bands, which themselves become increasingly flat. Note that $E_R \equiv \hbar^2\pi^2/2ma^2$.

2.2 Many-Atom Second-Quantized Hamiltonian

The AC Stark shift is an effect between a single atom and the field of light. There are also the interactions between the atoms themselves. The formalism of second quantization is useful to describe these features. The second-quantized many-body Hamiltonian in grand canonical ensemble is given by

$$\hat{H} = \int dx \hat{\Phi}^\dagger(x) \left(-\frac{\hbar^2}{2m}\nabla^2 + V_L(x) \right) \hat{\Phi}(x) \tag{2.13}$$

$$+ \int dx \hat{\Phi}^\dagger(x)(V_E(x) - \mu)\hat{\Phi}(x) \tag{2.14}$$

$$+ \frac{1}{2} \int dx dx' \hat{\Phi}^\dagger(x')\hat{\Phi}^\dagger(x) V_I(x - x')\hat{\Phi}(x)\hat{\Phi}(x') \,, \tag{2.15}$$

where $\hat{\Phi}(x)$ is the boson field annihilation operator for a boson at position x, $V_L(x)$ is the lattice potential, $V_E(x)$ is an arbitrary external potential, μ is the chemical potential, and $V_I(x-x')$ is the two-body interaction potential of atoms at positions x and x'. The

two-body interaction can be accurately described by an effective contact potential [38],

$$V_I(x - x') \approx \frac{4\pi a\hbar^2}{m}\delta(x - x')\,, \tag{2.16}$$

where a is the s-wave scattering length and m is the mass of the atoms. The assumption of a contact interaction characterized solely by the s-wave scattering length is valid as long as the temperature of the atoms is low enough to ignore p-wave and higher interaction terms. In this regime, the specifics of the interatomic potential are only a small perturbation to the s-wave scattering length. The interaction can be either repulsive or attractive depending on the sign of the scattering length. As described previously, the interaction strength and sign can be altered by the use of a Feshbach resonance.

2.3 Gross-Pitaevskii Equation

Exact calculations with the full second-quantized Hamiltonian can be impracticable for more than a small number of atoms. In cases where a large number of atoms are present, a mean-field theory can be used to describe the system using physically meaningful quantities as parameters [38].

The atomic field annihilation operator can be expanded exactly as

$$\hat{\Phi}(x) = \sum_i \Phi_i(x)\hat{a}_i\,, \tag{2.17}$$

where the set $\{\Phi_i(x)\}$ is a complete basis of single particle wave function, and $\{\hat{a}_i\}$ are the corresponding bosonic annihilation operators. The annihilation operators are defined such that

$$\hat{a}_i|N_i\rangle = \sqrt{N_i}|N_i - 1\rangle\,, \tag{2.18}$$

where N_i are the eigenvalues of the $\hat{a}_i^\dagger\hat{a}_i$ operator and give the number of atoms in the i state. The annihilation operators obey the usual Bosonic commutation relations. In a Bose-Einstein condensate, most of the atoms are in a single state, so that $N_0 \gg N_i$ for

all $i \neq 0$. Therefore, $N_0 \approx N_0 \pm 1$ and the approximation $\hat{a}_0 \approx \hat{a}_0^\dagger \approx \sqrt{N_0}$ can be made. For a uniform gas confined to a volume V, the wave function can then be expressed as

$$\hat{\Phi}(x) = \sqrt{N_0/V} + \delta\hat{\Phi}(x)\,. \tag{2.19}$$

The correction $\delta\hat{\Phi}(x)$ corresponds to excitations of the system out of the condensate mode. With a nonuniform system, the field operator can be expanded in a more general form as

$$\hat{\Phi}(x) = \phi(x) + \delta\hat{\Phi}(x) \tag{2.20}$$

where $\phi(x) \equiv \langle\hat{\Phi}(x)\rangle$ is a complex number called the condensate wave function, $\rho(x) = |\phi(x)|^2$ is the density of condensed atoms at position x, and $\langle\delta\hat{\Phi}(x)\rangle = 0$. The condensate function also has a well-defined phase. Note that for a finite system, the wave function $\phi(x)$ corresponds to the eigenstate with the largest eigenvalue of the single-particle density matrix, $\langle\hat{\Phi}^\dagger(x')\hat{\Phi}(x)\rangle$.

The equations that determine the dynamic motion of the condensate wave function are found by calculating the Heisenberg equation of motion for the $\hat{\Phi}$ operator

$$i\hbar\frac{\partial\hat{\Phi}(x)}{\partial t} = [\hat{\Phi}, \hat{H}] \tag{2.21}$$

$$= \left(-\frac{\hbar^2}{2m}\nabla^2 + V_L(x) + V_E(x) + \frac{4\pi a\hbar^2}{m}\hat{\Phi}^\dagger(x)\hat{\Phi}(x)\right)\hat{\Phi}(x)\,. \tag{2.22}$$

To zeroth order, one can replace $\hat{\Phi}(x) \to \phi(x)$ to give

$$i\hbar\frac{\partial\phi(x)}{\partial t} = \left(-\frac{\hbar^2}{2m}\nabla^2 + V_L(x) + V_E(x) + \frac{4\pi a\hbar^2}{m}|\phi(x)|^2\right)\phi(x)\,, \tag{2.23}$$

which is known as the Gross-Pitaevskii (GP) equation [65, 127], or the nonlinear Schrödinger (NLS) equation. The GP equation is valid when the interparticle spacing is much greater than the s-wave scattering length, the number of condensed atoms is much greater than one, and the temperature is low so that the number of condensed atoms is much greater than the number of atoms in any of the excited states. However, the theory is only

strictly valid for $\delta\hat{\Phi}(x) = 0$ which corresponds to zero temperature. Although the system is dilute, $\rho|a|^3 \ll 1$, interactions can have large effects on the system when the interaction energy is comparable in size to the kinetic energy of the atoms.

The Gross-Pitaevskii equation will be used to describe the nonlinear band structure of atoms in a periodic potential.

2.4 Bose-Hubbard Model

Another method used to describe the motion of atoms in a periodic potential is given by the Bose-Hubbard Hamiltonian. This model focuses on the relative influence of the interaction energy of two-body collisions and the kinetic energy associated with motion between lattice sites. The use of the Bose-Hubbard Hamiltonian is very common in condensed matter and solid state systems in which the motion of electrons is examined. The presence of a quantum phase transition between Mott insulator and superfluid states has been shown theoretically and experimentally [52, 64]. The details of this quantum phase transition will be described in a later chapter.

As with the examination of the GP equation, the Bose-Hubbard Hamiltonian is derived from the second-quantized many-body Hamiltonian,

$$\begin{aligned} \hat{H} &= \int dx \hat{\Phi}^\dagger(x) \left(-\frac{\hbar^2}{2m}\nabla^2 + V_L(x) \right) \hat{\Phi}(x) \\ &\quad + \int dx \hat{\Phi}^\dagger(x)(V_E(x) - \mu)\hat{\Phi}(x) \\ &\quad + \frac{1}{2}\int dx dx' \hat{\Phi}^\dagger(x')\hat{\Phi}^\dagger(x)V_I(x-x')\hat{\Phi}(x)\hat{\Phi}(x') \,. \end{aligned} \tag{2.24}$$

The difference lies in the way in the approximations used to decompose the bosonic annihilation operator. The operator will be decomposed into a set of site localized Wannier states that are related to the Fourier transform of the Bloch states. This decomposition is valid as long as the interactions are smaller than the band gap and the lattice is strong enough to prevent next-to-nearest neighbor hopping between sites.

The creation operator can be expanded in any complete set of basis states. Although the Bloch states may seem the most direct basis states to use, there is a set of localized states that often proves more convenient. The Wannier states are defined as

$$w_n(x - x_i) = \frac{1}{N} \sum_q e^{-iqx_i} \psi_q^{(n)}(x) \,, \tag{2.25}$$

where N is the total number of lattice sites, the sum is over all states in the first Brillouin zone, x_i is positioned in the center of site i, and $\psi_q^{(n)}(x)$ is the Bloch state solution of a single particle in the lattice with quasi-momentum q in the n^{th} band. With the use of the Wannier states, the annihilation operator can be given by,

$$\hat{\Phi}(x) = \sum_{in} \hat{a}_i^{(n)} w_n(x - x_i) \,, \tag{2.26}$$

where $\hat{a}_i^{(n)}$ is the annihilation operator of an atom at site i in the n^{th} band. If the chemical potential is less than the energy required for a single particle excitation to the second band, only the states from the lowest band need to be considered. The annihilation operator then simplifies to

$$\hat{\Phi}(x) = \sum_i \hat{a}_i w_0(x - x_i) \,, \tag{2.27}$$

which will be used in describing the Bose-Hubbard Hamiltonian. These are not the only way of defining Wannier states. For instance, a phase gradient can be applied to each Wannier state to better describe the effects of rotation [13].

The expansion of annihilation operator in terms of Wannier states can be inserted into the Hamiltonian to find

$$H = -J \sum_{\langle n,m \rangle} \hat{a}_n^\dagger \hat{a}_m + \frac{1}{2} U \sum_n \hat{a}_n^\dagger \hat{a}_n^\dagger \hat{a}_n \hat{a}_n + \sum_n (V_n - \mu) \hat{a}_n^\dagger \hat{a}_n \,, \tag{2.28}$$

where

$$J = -\int dx w_0^*(x - x_n) \left(-\frac{\hbar^2}{2m} \frac{\partial^2}{\partial x^2} + V(x) \right) w_0(x - x_{n+1}) \,, \tag{2.29}$$

$$U = \frac{4\pi a \hbar^2}{m} \int dx |w_0(x)|^4 \,, \tag{2.30}$$

$$V_n = \int dx |w_0(x)|^2 V(x) \,, \tag{2.31}$$

and $\langle n, m \rangle$ indicates a sum over nearest neighbors. It should be noted that only terms in which the overlap integral of Wannier states that are at most one lattice site in separation are considered since the remaining terms are much smaller. The higher order terms are often approximately two orders of magnitude smaller than the nearest neighbor terms. This is called the tight-binding approximation and assumes that the atoms are primarily described by a set of atoms in separate lattice sites with a small correction due to hopping between lattice sites. The tight-binding regime occurs when the lattice depth becomes approximately $V_0 > 5E_R$, where $E_R \equiv \hbar^2 k^2 / 2m$ is the atomic recoil energy.

The interaction strength can be characterized by the parameter U while the kinetic energy can be characterized by the hopping parameter J. In an optical lattice it is possible to alter the ratio J/U by adjusting the laser intensity. The hopping rate decreases exponentially as the intensity is increased while the interaction strength increases according to a power law. The alteration of the ratio J/U changes the relative effects of the kinetic energy and the interaction energy. Therefore, it is possible to have a dilute system, $\rho a_s^3 \ll 1$, with large effects due to interactions, $J/U \approx 1$. The assumptions of the Bose-Hubbard model are valid as long as the interaction energy UN is much smaller than the gap between the first and second bands.

A mean field approximation can be applied to the Bose-Hubbard model in which the bosonic operators are replaced with a c-number, as was done in the GP equation. If interactions are neglected, $U = 0$, the Hamiltonian can be used in what is called the discrete Schrödinger equation or tight-binding Schrödinger equation. If interactions, are not excluded, the discrete nonlinear Schrödinger equation can be used.

The Bose-Hubbard Hamiltonian with a site dependent external potential, will be the basis for the model of an atomtronic system.

Chapter 3

Nonlinear Band Structure

The nonlinear Schrödinger equation (NLS), as introduced in the previous chapter, models many kinds of wave phenomena. The NLS appears in diverse fields such as nonlinear optics [167], gravity waves on deep water [73], magneto-static spin waves [151], solitons in liquid crystals [36], and magneto-sonic solitons in the atmospheric magneto-pause boundary layer [160]. It also describes the dynamics of the mean field of a weakly interacting atomic or molecular Bose-Einstein condensate (BEC) [6, 39, 19, 18], where it is known as the Gross-Pitaevskii equation [65, 127].

Periodic potentials are ubiquitous in physics, appearing in electron transport in metals [4], Josephson junction arrays [171], nonlinear photonic crystals and waveguide arrays [35], and Bose-Einstein condensates (BEC's) [63]. With the realization of BEC's of alkali atoms in a sinusoidal optical lattice, there has been an explosion in studies of BEC's in these potentials, both experimentally and theoretically [64, 49, 46, 48, 45, 50]. BEC's in optical lattices have been used to study phase coherence of atom lasers [5, 70] and matter-wave diffraction [121]. Therefore, in the context of the BEC, the study of periodic potentials provides an excellent connection between condensed matter physics and atomic physics. In contrast to other physical contexts, the lattice geometry and strength, as well as the interatomic interactions [136, 81], are all tunable parameters for the BEC.

Experimentally, in order to create a BEC in a lattice, alkali atoms are first cooled

to a quantum degenerate regime by laser cooling and evaporation in harmonic electromagnetic traps [6, 39]. A sinusoidal optical lattice is then made by the interference of two counter-propagating laser beams, which creates an effective sinusoidal potential proportional to the intensity of the beams [64]. The potential is due to the AC Stark shift induced by the dipole interaction with the electromagnetic field on the atoms' center of mass [110]. For large detuning of the optical field from the atomic transition, dissipative processes, such as spontaneous emission, can be minimized and the potential becomes conservative. Nonzero quasi-momentum can be examined by slightly detuning the two lasers by a frequency $\delta\nu$ [50]. The resulting interference pattern is then a traveling wave moving at the velocity $v = (\lambda/2)\delta\nu$, where λ is the wavelength of the first beam. This produces a system with quasi-momentum $q = mv/\hbar$, where m is the atomic mass. Note that this is not necessarily the velocity and momentum of the atoms in the lattice since dragging may occur. The actual velocity is derived from the dispersion relation of the band structure. After a given evolution time, the traps are switched off. The BEC is allowed to expand and the density is then imaged.

With the experimental demonstration of Feshbach resonances in BEC's of dilute atomic gases [136, 81], it is possible to alter the s-wave scattering length and, hence, the nonlinearity of the NLS. Near a Feshbach resonance, the scattering length becomes a function of a uniform background magnetic field. By altering the magnetic field, the effects of the nonlinearity can be experimentally controlled. It is therefore important to be able to characterize the complete set of solutions as a function of the interaction strength.

The complete set of stationary solutions to the NLS with a constant potential on the infinite line were discovered by Zakharov and Shabat [177, 178]. The stationary solutions of the NLS under periodic and box boundary conditions has also been solved analytically [26, 27], as well as the finite well [30]. The parabolic potential has been solved numerically [93]. The potential step has been examined theoretically and

experimentally for the linear Schrödinger equation with a constant [172, 118] and oscillating [51] step. Klein examined similar problems experimentally by deflecting neutron beams with a vibrating crystal [96]. In addition, symmetric steady-state solutions with a point-like impurity potential have been studied by Hakim [71] and Taras-Semchuk [168] in certain limiting cases. Point-like impurity potentials have been studied extensively, such as with helium impurities in a BEC [25, 72], BEC formation initiated by point like impurities [32] and impurity scattering in a BEC of sodium [34]. The superfluid transmission of matter waves across various potentials has been studied [99, 122]. In addition, bound solutions to the NLS are the one-dimensional analog to the pinned vortex solutions which occur when a discontinuity is present in a two dimensional system, such as in a two dimensional high-T_c superconducting system.

The case of a BEC trapped in a sinusoidal potential has been studied theoretically in great detail by a number of researchers [101, 174, 175, 23, 24, 28, 164, 165, 43, 117, 173, 40, 107, 108, 105, 134, 169, 120, 133, 129]. In addition, a subset of the solutions to the Kronig-Penney potential has been found [170, 55, 168, 2, 102]. Recently, for example, Li and Smerzi [102] investigated generalized Bloch states for constant phase and zero current. In contrast, we present the full set of Bloch wave stationary solutions for both repulsive and attractive BEC's. An important point is that the sinusoidal optical lattice potential is composed of a single Fourier component. If more counter-propagating laser beams of different frequencies are added as is experimentally possible, more Fourier components are introduced, and the potential becomes a lattice of well separated peaks. In the limit that the width of the these peaks becomes much smaller than the healing length of the BEC, the potential effectively becomes a Kronig-Penney lattice. However, we show that the Kronig-Penney potential serves as a good model even for experiments with a single Fourier component.

Here, we consider the steady state response of the mean field of a BEC to a constant potential, a potential step, a delta function potential, and a Kronig-Penney

potential as modeled by the NLS. These potentials may be easily produced in present experiments on the BEC. The step potential may be realized by a detuned laser beam shined over a razor edge to make a sharp barrier, where the diffraction-limited fall-off of the laser intensity is smaller than the healing length of the condensate, so that the potential is effectively a step function. The delta function potential models the response of the condensate to an impurity of a length scale smaller than the healing length, which could be realized by a tightly focused laser beam, by another spin state of the same atom, or by any other object, as for instance another alkali atom, confined in an optical trap.

The delta-function lattice is an approximation to the easily created optical lattice potential. Specifically, we consider the steady state response of the mean field of a BEC to a Kronig-Penney potential using the Bloch ansatz. We first obtain the full set of stationary solutions for a single delta function analytically [152, 14, 10, 130]. Using these results, we are able to rigorously describe the band structure. We find that above a critical nonlinearity, swallowtails, or loops, form in the bands [173, 107, 153]. Stability properties are studied numerically by time evolution of perturbed stationary state solutions to the NLS. It is found that stable, as well as unstable, regimes exist for both repulsive and attractive BEC's. Finally, the appearance of swallowtails is connected to period doubled states by examining the band structure of a two-color lattice [154].

We show that the mean field Bloch states of a BEC in a Kronig-Penney potential, i.e., a lattice of delta functions, exhibits the same band structure and stability properties as the experimental case of a sinusoidal potential. Unlike in the case of the sinusoidal potential, Bloch state solutions to the Kronig-Penney potential can be described by straightforward analytic expressions. The Kronig-Penney potential, therefore, has distinct advantages as a model of BEC's trapped in periodic potentials.

In this chapter, we first examine a condensate subject to a constant potential,

essentially the free-particle states. These results can be used to analyze the effects on a condensate due to a step potential or delta function potential, both of which are single boundary potentials. A lattice of delta functions, a Kronig-Penney potential, models an optical lattice and is then used to create a full nonlinear band structure analytically. Finally, the appearance of swallowtails, or loops in the band structure, are connected to period-doubled states by examining a two-color lattice.

3.1 Constant Potential

We examine the BEC in the quasi-one-dimensional regime and obtain the full set of stationary states in closed analytic form. When the transverse dimensions of the BEC are on the order of its healing length, and its longitudinal dimension is much longer than its transverse ones, the 1D limit of the 3D NLS is appropriate to describe the system [29]. This corresponds to tight confinement with an optical lattice in two directions creating a 2D set of one dimensional tubes. A third weaker lattice is created in the free dimension. The 1D NLS, with an external potential, $V(x)$, may be written

$$i\partial_t \Psi = -\frac{1}{2}\partial_{xx}\Psi + g|\Psi|^2\Psi + V(x)\Psi\,, \tag{3.1}$$

where a harmonic oscillator confinement in the transverse directions with frequency ω has been assumed [119] for atoms of mass M, the length has been rescaled according to units of the oscillator length, $l_{ho} = (\hbar/M\omega)^{1/2}$, and energy rescaled according to units of the oscillator energy, $\hbar\omega$. The renormalized 1D coupling, $g \equiv 2a_s$, where a_s is the s-wave scattering length, characterizes the short-ranged pairwise interactions between atoms. The wave function or order parameter, $\Psi(x,t)$, can be written as $\Psi(x,t) = \sqrt{\rho(x,t)}\exp[i\phi(x,t)]$, where $\rho(x,t)$ is the longitudinal line density and the longitudinal superfluid velocity is given by $v(x,t) = \partial\phi(x,t)/\partial x$. Both attractive and repulsive atomic interactions, *i.e.*, $g < 0$ and $g > 0$, shall be considered.

In the case where the harmonic oscillator length approaches the s-wave scattering

length, $l_{ho} \simeq a_s$, the 1D NLS no longer models the system and a one-dimensional field theory with the appropriate effective coupling constant must be considered instead [119]. Since a_s is on the order of angstroms for typical BEC's, this regime is not relevant to the present study. Thus, it should be noted that this study does not examine the Tonks-Girardeau regime [57], where quantum fluctuations become important and the Gross-Pitaevskii equation no longer models the system.

The ability to analytically describe the full nonlinear band structure of a condensate derives from the stationary solutions of a free condensate [177, 178]. Stationary states are given by the form

$$\Psi(x,t) = \psi(x)e^{-i\mu t}\,, \tag{3.2}$$

where μ is the eigenvalue of the stationary solution and converts the partial differential GP equation, Eq. (3.1), into the ordinary differential equation

$$\mu\psi = -\frac{1}{2}\partial_{xx}\psi + g|\psi|^2\psi + V(x)\psi\,. \tag{3.3}$$

The wave function can be further broken up to describe the density and phase as

$$\psi(x,t) = R(x)e^{i\phi(x)}\,, \tag{3.4}$$

where $|R(x)|^2$ is the condensate density at x and $\phi(x)$ is the condensate phase at x. There are several excellent references which consider stationary solutions in a constant potential [80, 95, 29, 79, 176]. Assuming a constant external potential V, the separation of Eq. (3.1) into real and imaginary parts gives

$$R\,\partial_{xx}\phi + 2(\partial_x R)\,(\partial_x\phi) = 0\,, \tag{3.5}$$

$$\frac{1}{2}\partial_{xx}R + \frac{1}{2}(\partial_x\phi)^2\,R + g\,R^3 + V\,R = \mu\,R\,. \tag{3.6}$$

Equation (3.5) can be integrated to give

$$\partial_x\phi = \frac{\alpha}{\rho}\,, \tag{3.7}$$

where α is an undetermined constant of integration, and $\rho(x) = |R(x)|^2$ is the single-particle density. Substituting Eq. (3.7) into Eq. (3.6) and integrating yields

$$\frac{\mathrm{d}\rho}{\mathrm{d}x} = 2\sqrt{g\,\rho^3 - 2(\mu - V)\rho^2 + C\,\rho - \alpha^2}\,. \tag{3.8}$$

Integrating a second time gives

$$\int \frac{1}{\sqrt{g\rho^3 - 2(\mu - V)\rho^2 + C\rho - \alpha^2}}\,\mathrm{d}\rho = 2x + x_0\,, \tag{3.9}$$

where C and x_0 are undetermined constants of integration. It is shown in App. B that the only solutions to this integral equation are given by the Jacobian elliptic functions [17, 1]. The Jacobi elliptic functions can be considered generalizations of the trigonometric and hyperbolic functions and interpolate between the two. In App. A these special functions are briefly reviewed. The most general form of the solution is then given by

$$\rho = A\,\mathrm{sn}^2(b\,x + x_0, k) + B\,, \tag{3.10}$$

where sn is one of the Jacobian elliptic functions, A is a density prefactor, b is a translational scaling, x_0 is a translational offset, k is the elliptic parameter, and B is a vertical density offset. The period of the density is given by $2\,K(k)/b$, where $K(k)$ is the complete elliptic integral of the first kind. Since the density is positive definite, the variables are restricted such that $B \geq 0$ and $B + A \geq 0$. In Sec. 3.5 the relation between these variables and the mean number density, energy density, and momentum density are calculated and discussed for the nonlinear wave of Eq. (3.10).

It should be noted that since many of the solutions are unbounded, the norm of the wave function remains unconstrained. This is in contrast to bound or localized solutions when the normalization,

$$\int_{-\infty}^{+\infty} (\rho - \overline{\rho})\,\mathrm{d}x = 1\,, \tag{3.11}$$

may be used [95], where $\overline{\rho}$ is the average density. This allows for a normalization of systems with a localized disturbance to a constant background field. It is possible to

use a nonlinear scaling of the position and density, $x \to ax$ and $\rho \to a^{-2}\rho$, to scale the maximum density on one side of a boundary to unity. However, for considerations of single boundary systems the wave function remains unnormalized. Normalization for a periodic potential will be such that the norm of each lattice site is set to unity.

One may then determine the variables μ, α, and k, in terms of A, B, b, and g by substituting Eq. (3.10) into Eq. (3.8) and equating powers of the elliptic *sn* function to give

$$\mu = \frac{1}{2}(b^2 + (A+3B)g) + V\,, \tag{3.12}$$

$$\alpha^2 = B(A+B)(b^2+Bg)\,, \tag{3.13}$$

$$k^2 = \frac{A}{b^2}g\,. \tag{3.14}$$

This leaves the eigenvalue, μ, the constant of integration of the phase, α, and the elliptic parameter, k, determined up to A, B, b, and the interaction strength, g. Note that the fact that α enters into the equations only as α^2 implies that all *nontrivial phase* solutions, *i.e.*, those for which $\alpha \neq 0$, are doubly degenerate, as $\pm\alpha$ lead to the same value of the eigenvalue, μ, without otherwise changing the form of the density or phase. This corresponds to the energetic degeneracy of left moving and right moving systems. We shall use the term *trivial phase* to refer to solutions for which the phase is spatially constant.

In the following two sections these results are applied to piecewise constant potentials. In particular, the potential step and the delta function potential are examined.

3.2 Potential Step

In this section the complete set of solutions to the NLS with an external step potential of height V_0,

$$V(x) = V_0\,\theta(x)\,, \tag{3.15}$$

are presented analytically, given the solution parameters on the lower side of the step. In the following two subsections, the general solution to the NLS with a potential step and some particular examples are discussed.

3.2.1 General Solution

Applying the two boundary conditions of continuity of the wave function and continuity of the derivative of the wave function gives the following five conditions,

$$\rho(0^+) = \rho(0^-)\,, \tag{3.16}$$

$$\partial_x\rho(0^+) = \partial_x\rho(0^-)\,, \tag{3.17}$$

$$\phi(0^+) = \phi(0^-) + 2\pi n\,, \tag{3.18}$$

$$\alpha(0^+) = \alpha(0^-)\,, \tag{3.19}$$

$$\mu(0^+) = \mu(0^-)\,, \tag{3.20}$$

where n is an integer. The first two conditions represent the continuity of the density, Eq. (3.16), and the derivative of the density, Eq. (3.17). The next two conditions represent the continuity of the phase, Eq. (3.18), and the derivative of the phase, Eq. (3.19). Equation (3.20) demands that the eigenvalue be the same on either side of the boundary. Note that in Eq. (3.12) the eigenvalue on the right hand side is offset by V_0 as compared to the left hand side. Since n only enters into the phase and does not effect such quantities as the eigenvalue and density, only the $n = 0$ state is considered and, consequently, the phase, ϕ, is continuous across the boundary. However, it is important to note that all solutions are of denumerably infinite degeneracy, according to Eq. (3.18). Since ϕ is given by

$$\phi(x) = \int_0^x \frac{\alpha}{\rho(x)}\mathrm{d}x + \text{const.}\,, \tag{3.21}$$

continuity in the phase is easily achieved by setting the constant phase shift equal on either side of the boundary and, therefore, Eq. (3.18) is satisfied.

In the following derivation, it is assumed that the wave function parameters on the left side of the step are known completely. Therefore the density prefactor, A_L, the vertical density offset, B_L, the translational scaling, b_L, and the horizontal offset, x_{0L} are all known, where the L subscript refers to variables on the left side; an R subscript will refer to variables on the right side. In addition, the experimental parameters of the interaction strength, g, and the potential step height, V_0, are both known. From the variables on the left and Eq. (3.10), the density at the boundary, $\rho_L \equiv \rho(0^-)$, and its derivative at the boundary, $\partial_x \rho_L \equiv \partial_x \rho(0^-)$, can be determined. The eigenvalue, μ, and the phase constant, α, can be determined from Eqs. (3.12) and (3.13).

From Eqs. (3.10) and (3.16) the square of the Jacobian elliptic sn function can be solved for,

$$\mathrm{sn}^2\left(x_{0R}, \sqrt{\frac{A_R g}{b_R^2}}\right) = \frac{\rho_L - B_R}{A_R}\,. \tag{3.22}$$

From Eqs. (3.12) and (3.20), the horizontal scaling, b_R, is given by

$$b_R^2 = 2(\mu - V_0) - (A_R + 3B_R)g\,. \tag{3.23}$$

These variables are substituted into Eqs. (3.19) and (3.17), using Eq. (3.13), to give

$$\begin{aligned} \alpha_L^2 &= B_R(A_R + B_R) \\ &\quad \times [2(\mu - V_0) - (A_R + 2B_R)g]\,, \end{aligned} \tag{3.24}$$

$$\begin{aligned} (\partial_x \rho_L)^2 &= -4(B_R - \rho_L)(A_R + B_R - \rho_L) \\ &\quad \times [2(\mu - V_0) - (A_R + 2B_R + \rho_L)g]\,. \end{aligned} \tag{3.25}$$

Equations (3.24) and (3.25) are quadratic in A_R and cubic in B_R and can be solved analytically for A_R and B_R to give six solutions. The remaining variables on the right side can then be found by substituting the values of A_R and B_R into Eq. (3.23), to find b_R, and by taking the inverse Jacobi sn function of Eq. (3.22) to give

$$x_{0R} = \mathrm{sn}^{-1}\left(\frac{\rho_L - B_R}{A_R}, \sqrt{\frac{A_R g}{b_R^2}}\right)\,. \tag{3.26}$$

The full solution is then completely known. It is therefore possible to completely describe the system analytically knowing only the parameters on one side of the step. This not only introduces computational ease in evaluating solutions, it also provides all possible solutions, most of which cannot be determined using purely numerical methods. In the following section, specific examples of a BEC in the presence of a step potential will be examined.

3.2.2 Particular Examples

The solutions to the potential step problem can be divided into two categories. The eigenvalue, μ, can be large enough that particles are free to move across the boundary. It is then possible to examine the nonlinear analog to a transmitted wave for the linear Schrödinger equation. However, if the eigenvalue is too small, then the wave function must decay under the step.

When μ is larger than the effective potential,

$$V_{eff}(x) = V_0 + g\rho(x)\,, \tag{3.27}$$

the wave can be transmitted across the boundary. Note that in the case of an attractive interaction, $g < 0$, the eigenvalue can be less than the step height, V_0, and for a repulsive interaction, $g > 0$, the eigenvalue must be strictly greater than the step height. In Figs. 3.1(a) and (b), the density and phase of a nonlinear state with a repulsive interaction strength is shown. A step of height $V_0 = 1$, positioned at $x = 0$, and a condensate with an interaction strength of $g = 0.2$ and eigenvalue of $\mu = 2.404$ were used. The increased interaction strength and nonlinearity has caused the peaks of the wave function to become much broader than in the linear case, which would be simply sine waves. Figure 3.1(c) and (d) present the density and phase of a similar solution but with an attractive interaction strength. This potential is again given by a step with height of $V_0 = 1$, positioned at $x = 0$. An interaction strength of $g = -0.2$ and

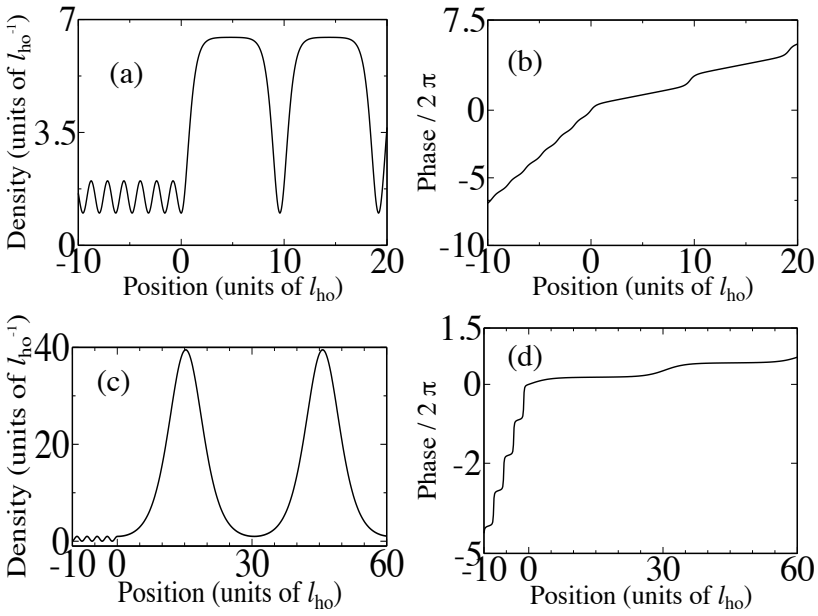

Figure 3.1: Stationary solutions to the NLS with a potential step of form $V(x) = V_0\theta(x)$. These solutions, which are the nonlinear analogs of the continuum of linear stationary scattering states, exhibit a large deviation from the traditional linear solutions. Shown are particular examples of (a) the density and (b) the phase for a repulsive interaction strength and (c) the density and (d) the phase for attractive interaction strength.

eigenvalue of $\mu = 0.98$ was used. In this case, the peaks have instead narrowed due to the attractive interaction.

When the eigenvalue is smaller than the effective potential, $\mu < V_{eff}(x)$, the wave function must decay under the step. In Fig. 3.2(a) the density of a nonlinear solution with a repulsive interaction strength that decays as it crosses the boundary of the step is shown. A step with height of $V_0 = 1$, positioned at $x = 0$, and a condensate with an interaction strength of $g = 0.12$ and eigenvalue of $\mu = 0.5$ were used. Figure 3.2(b) shows a similar solution but with an attractive interaction strength. This potential is again given by a step with height of $V_0 = 1$, positioned at $x = 0$. An interaction strength of $g = -10$ and eigenvalue of $\mu = -49$ were used. For both wave functions, the phase is necessarily trivial, since all wave function that approach zero at infinity must have $A = -B$, and hence from Eqs. (3.7) and (3.13), the phase is constant. In order to stress

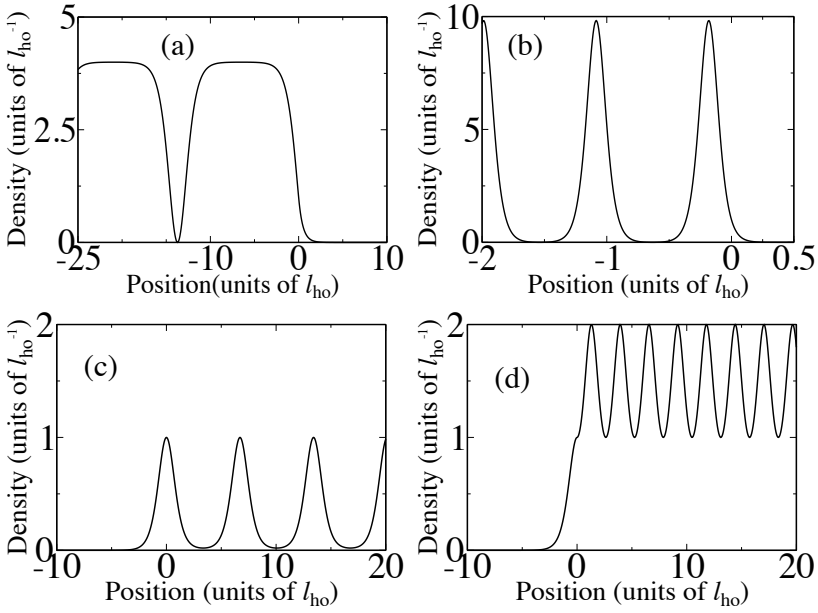

Figure 3.2: Stationary solutions to the NLS with a potential step for which the wave function decay, which are the nonlinear analogs to evanescent waves. Shown are particular examples of the densities of nonlinear waves with (a) repulsive interaction strength, (b) attractive interaction strength, and (c) and (d) with an attractive interaction strength that decay on the lower side of the step.

the importance of the effective potential, and not just the step potential, Figs. 3.2(c) and (d) show the density of two nonlinear wave function with attractive interactions, $g = -1$, that decay occurs on the lower side of the potential. Both wave function have an eigenvalue of $\mu = -0.5$ and a potential of height of $V_0 = 0.01$ and $V_0 = 1$ were used for Fig. (3.2(c) and Fig. 3.2(d), respectively.

Thus the NLS with a potential step has solutions to the step potential that provide a connection between the linear solutions and a wide variety of exotic nonlinear wave function, as shall be discussed in Sec. 3.4.

3.3 Point-like Impurity

In this section, the case of a potential of form

$$V(x) = V_0\,\delta(x) \tag{3.28}$$

is considered. Such a potential models an impurity which deforms the constant background potential on a length scale much less than that of the healing length. Given the state of the system on the negative x, or left side of the impurity, the variables on the right side of the impurity are determined. A negative value of V_0 represents an attractive impurity, such as due to defects in hydrogen-bonded chains [94, 92], and a positive value of V_0 represents a repulsive impurity, such as with helium atoms in a BEC [25, 72].

3.3.1 General Solution

The boundary conditions for an impurity are similar to those for the potential step, except that the derivative of the wave function experiences a discontinuity at the boundary. Therefore, Eqs. (3.16), (3.20), (3.19) and (3.18) must still be satisfied, along with

$$\partial_x \rho(0^+) - \partial_x \rho(0^-) = -4\rho(0)V_0\,. \tag{3.29}$$

It is again assumed that all variables on the left side of the impurity are known as well as the experimental parameters of interaction strength, g, and impurity strength, V_0. Using a treatment that is exactly analogous to that for the step function, all of the parameters on the right side, given those on the left, are analytically determined. The only difference is that in Eqs. (3.23), (3.24), (3.25), and (3.26), the quantity $\partial_x \rho_L$ must be replaced with $(\partial_x \rho_L - 4V_0\rho_L)$ and $(\mu - V_0)$ must be replaced with μ. It is therefore possible to completely describe the system analytically knowing only the parameters on one side of the impurity. In the following section, examples of wave functions subject to an impurity are examined.

3.3.2 Particular Examples

For the delta function potential, both symmetric and nonsymmetric wave function are possible. Of particular interest are the symmetric wave function in the $k = 1$

limit of the Jacobian elliptic functions. In this case all solutions become hyperbolic trigonometric functions with a localized change in the density around the impurity and no oscillations at $\pm\infty$. Solutions of this type we term *localized* [30] and are of four different forms:

$$\rho = \alpha^2 + (1-\alpha^2)\tanh^2(\sqrt{1-\alpha^2}|x| + x_0)\,, \tag{3.30}$$

$$\rho = \alpha^2 + (1-\alpha^2)\coth^2(\sqrt{1-\alpha^2}|x| + x_0)\,, \tag{3.31}$$

$$\rho = b^2\mathrm{sech}^2(b|x| + x_0)\,, \tag{3.32}$$

$$\rho = b^2\mathrm{csch}^2(b|x| + x_0)\,, \tag{3.33}$$

where the translational offset, x_0, is determined by the impurity strength, V_0, and the density has been normalized according to Eq. (3.11). Equations (3.30) and (3.31) are valid for repulsive interactions, while Eqs. (3.32) and (3.33) are valid for attractive interactions.

Figure 3.3 shows the possible wave function for repulsive interactions. An example of the solution described by Eq. (3.30) is plotted in Fig. 3.3(a) with a repulsive impurity of strength $V_0 = 0.5$. This may be interpreted as a single dark soliton bound by an impurity. This is similar to the solution found by Hakim [71] for a soliton that is moving with an impurity. In addition, a bound state of two dark solitons, Fig. 3.3(c), can be created when the strength of the impurity is attractive and exactly balances the repulsion between the two dark solitons. Figure 3.3(e) shows the hyperbolic cotangent function solution with an impurity strength of $V_0 = -0.5$; this may be interpreted as a deformation of the ground state constant solution to the NLS with a constant potential. In all plots an interaction strength of $g = 1$ and phase constant of $\alpha = 0.5$ were used.

It should be noted that there exists a bound state of a repulsive condensate with an attractive impurity. This solution is given by,

$$\rho = \frac{b^2}{g}\mathrm{csch}^2\left(bx + \coth^{-1}\left(\frac{-V_0}{b}\right)\right)\,, \tag{3.34}$$

where the interaction strength, g has specifically been included and b must be determined such that the density is normalized to unity. These requirements place a limit on how repulsive the interaction may become and is given by,

$$g_{\max} = -4V_0\,, \tag{3.35}$$

where $g_{\max}$ is the most repulsive interaction the condensate may have. If the interaction is increased past this point, the condensate will spill away from the impurity and will no longer be bound.

The set of symmetric localized solutions for the case of attractive interactions do not allow for nontrivial phases, in contrast to the case of repulsive interactions. For attractive interactions, $g < 0$, the hyperbolic secant function solution, Eq. (3.32), is valid for both $V_0 > 0$, Fig. 3.4(a), and $V_0 < 0$, Fig. 3.4(b), where potential strengths of $V_0 = 0.9$ and $V_0 = -0.9$ were used, respectively. These solutions may be interpreted as a single bright soliton, which is the ground state solution to the 1D-NLS, deformed by an impurity. The hyperbolic cosecant function solution, Eq. (3.33), is only valid if $V_0 < 0$ and is similar in form to the hyperbolic secant solution of Fig. 3.4(b). The two solutions types are degenerate for $V_0 < 0$, with an eigenvalue of $\mu = -b^2/2$. In Figs. 3.4(a) and (b) an interaction strength of $g = -1$ and translational scaling of $b = 1$ were used.

Nonsymmetric wave function which oscillate at infinity are also possible and come in two forms, oscillations on one side of the delta function and oscillations on both sides. Figure 3.5 shows two possible nonsymmetric wave function subject to a delta function positioned at $x = 0$ that oscillate on one side of the potential. The density of a wave function with a repulsive interaction strength of $g = 0.21$ and eigenvalue of $\mu = 2.4$, distorted by a delta function, $V_0 = 2$, is shown in Fig. 3.5(a), where the left side reproduces the hyperbolic tangent function of Eq. (3.30). In Fig. 3.5(b), an attractively interacting, $g = -50$, wave function with an eigenvalue of $\mu = -50$, distorted by a delta function, $V_0 = 10$, is shown that appears similar to the evanescent wave function of

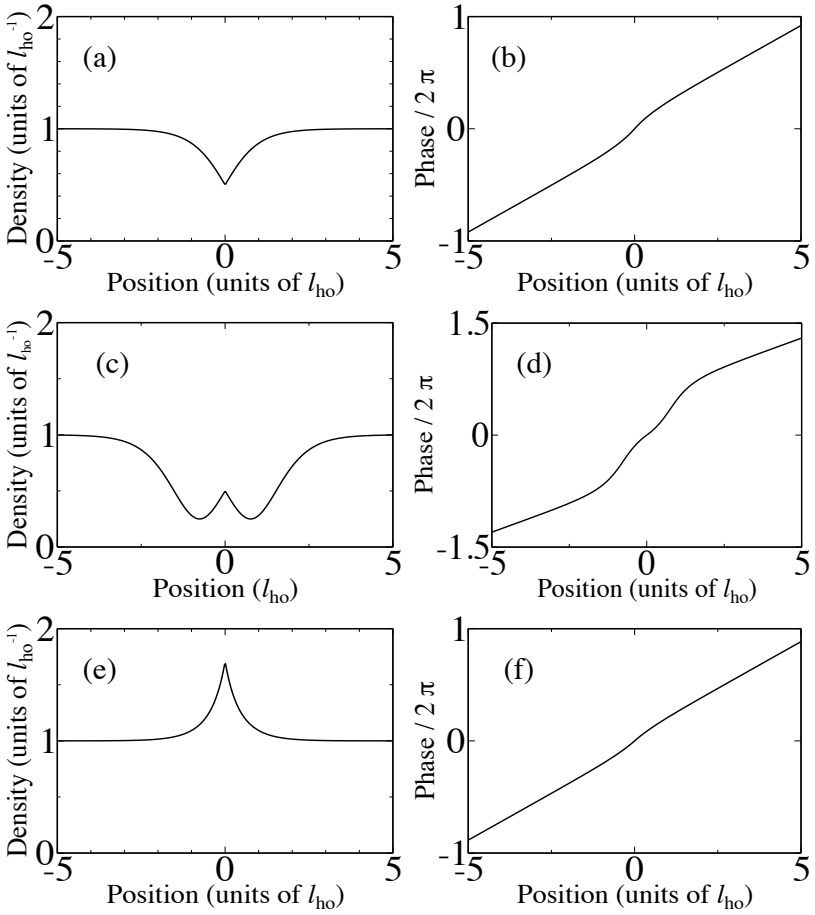

Figure 3.3: Localized, symmetric solutions to the NLS with repulsive interaction strength in the presence of an impurity, $V(x) = V_0\delta(x)$. Shown are particular examples of (a) the density and (b) the phase of a dark soliton bound by a repulsive impurity, (c) the density and (d) the phase of a pair of dark solitons bound by an attractive impurity, and (e) the density and (f) the phase of a supercurrent deformed by an attractive impurity. Note that (a) and (c) may also be interpreted as deformations of a supercurrent.

Fig. 3.2 that decay beneath a step. Note that Fig. 3.5(a) has a nontrivial phase while the phase of Fig. 3.5(b) is trivial.

Figure 3.6 shows two possible nonsymmetric wave function subject to a delta function positioned at $x = 0$ with strength $V_0 = 2$ that oscillate on both sides of the potential. A repulsive interaction strength produces the characteristic widening of the pulse peaks, Fig. 3.6(a). The corresponding phase is given in Fig. 3.6(b). An attractive interaction strength creates a narrowing of the pulse peaks, Fig. 3.6(c). The

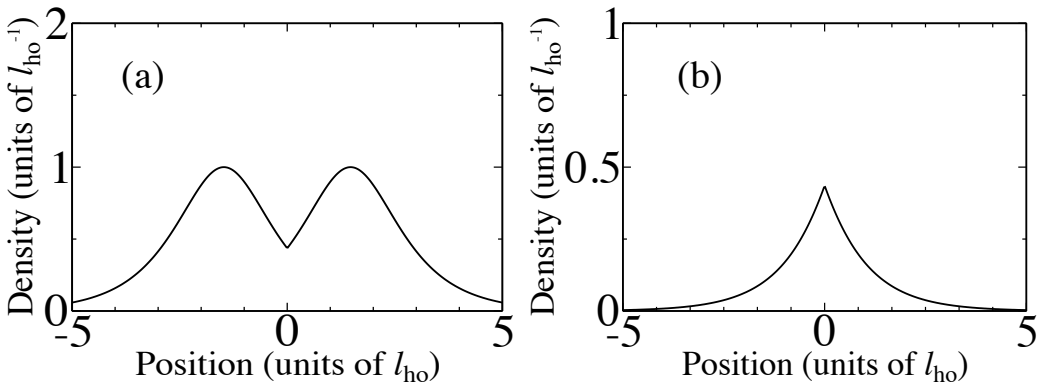

Figure 3.4: Localized, symmetric solutions to the NLS with attractive interaction strength in the presence of an impurity. Shown are particular examples of (a) the density of a bright soliton, which is the ground state solution to the NLS, deformed by a repulsive impurity and (b) the density of a bright soliton deformed by an attractive impurity.

corresponding phase is given in Fig. 3.6(d). The condensates in Figs. 3.6(a) and (c) are characterized by eigenvalues of $\mu = 2.4$ and $\mu = -1.3$, respectively.

3.4 Linear Limits of Transmitted and Reflected Waves

In this section it is shown how the solutions to the NLS connect to the solutions of the linear Schrödinger equation. There are two distinct types of possible waves. If the wave has enough energy it is possible to make the wave propagate through space. However, if it does not have enough energy, the wave can carry no current and is referred to as an evanescent wave. These waves must decay. In the next two sections, these two types of waves are discussed concerning their role as the linear limit of the nonlinear solutions.

3.4.1 Transmitted Waves

In a linear system, if the energy of the system is greater than the potential energy, then the wave can be transmitted through space as sine waves. The nonlinear Jacobian elliptic *sn* function waves are the nonlinear analogue of the sine waves of a linear system.

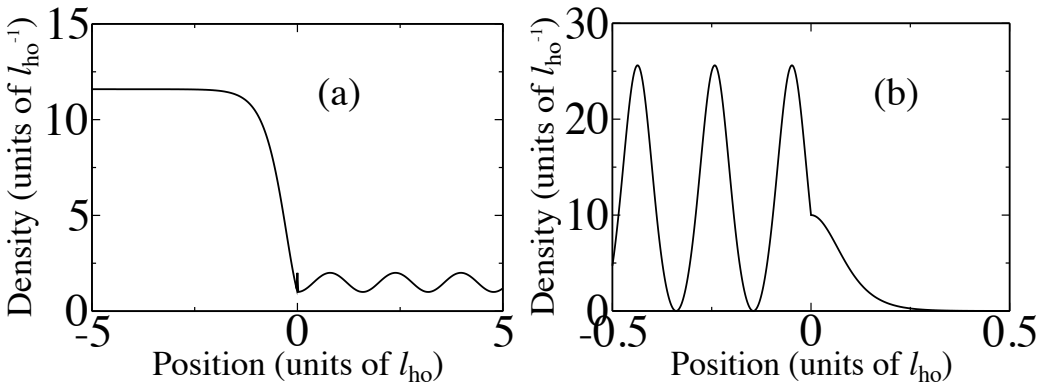

Figure 3.5: Solutions to the NLS with an impurity that oscillate on one side of the potential. Shown are particular examples of (a) the density of a nonlinear wave with repulsive interaction strength and (b) the density of a nonlinear wave with attractive interaction strength. These waves have no analog with the solutions of the linear Schrödinger equation.

In this section, it is shown how the nonlinear solutions, in the linear limit, recreate the linear solutions of propagating waves.

For the linear case, the usual representation of the system by incident, transmitted, and reflected waves is given by,

$$\Psi_L(x,t) = \left(e^{ik_L x} + Re^{-ik_L x}\right) e^{-i\mu t}, \tag{3.36}$$

$$\Psi_R(x,t) = Te^{ik_R x}\, e^{-i\mu t}, \tag{3.37}$$

where $k_L = \sqrt{2(\mu - V_L)}$, $k_R = \sqrt{2(\mu - V_R)}$, μ is the eigenvalue of the Schrödinger equation, R is the reflection coefficient, T is the transmission coefficient, and the incident wave is assumed to be coming in from the left. The potentials, V_L and V_R, and the scattering coefficients, R and T, are determined by the type of boundary. For the case of a potential step, the potentials are given by $V_L = 0$ and $V_R = V_0$. For a delta function potential, the potentials are given by $V_L = V_R = 0$. The wave function can be alternately described by an amplitude and phase as follows:

$$\rho_L = (1+r)^2 - 4\,r\,\sin^2(\sqrt{2\,\mu}\,x - s/2), \tag{3.38}$$

$$\partial_x \phi_L = \frac{(r-1)(r+1)\sqrt{2\,\mu}}{(1+r)^2 - 4\,r\,\sin^2(\sqrt{2\,\mu}\,x - s/2)}, \tag{3.39}$$

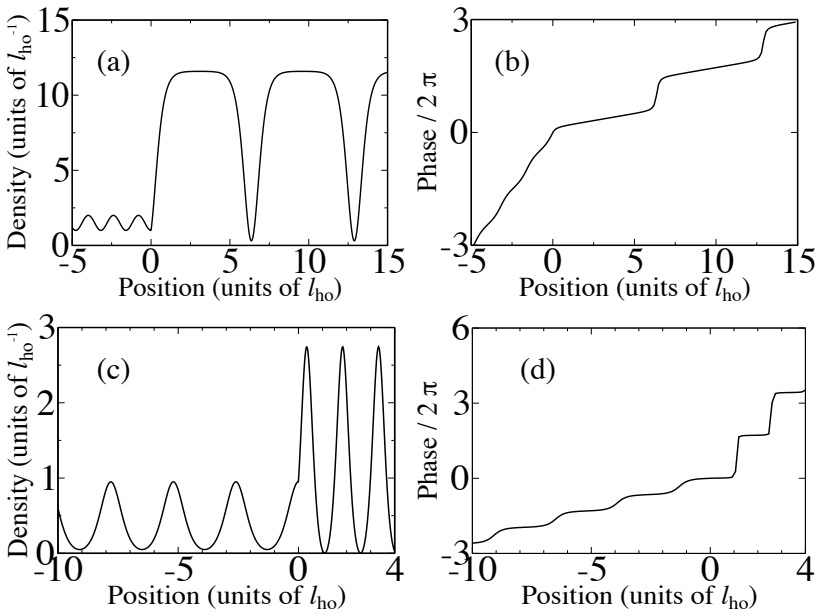

Figure 3.6: Nonsymmetric solutions to the NLS with an impurity. Shown are particular examples of (a) the density and (b) the phase of a nonlinear wave with repulsive interaction strength and (c) the density and (d) the phase of a nonlinear wave with attractive interaction strength. These solutions are the nonlinear analogs to the continuum of linear stationary scattering states.

where

$$\Psi_L(x,t) = \sqrt{\rho_L(x)}\,\exp[i\phi_L(x)]\,e^{-i\mu t}\,, \tag{3.40}$$

$$R = re^{is}\,, \tag{3.41}$$

with r and s real. The nonlinear solution is then connected to the linear solution by

$$x_0 = -s/2\,, \tag{3.42}$$

$$b^2 = 2\mu\,, \tag{3.43}$$

$$A = -4r\,, \tag{3.44}$$

$$B = (r+1)^2\,. \tag{3.45}$$

The transmitted wave can easily be given by

$$\rho_R = t^2\,, \tag{3.46}$$

$$\partial_x\phi_R = \frac{\sqrt{2\mu}}{t^2}\,, \tag{3.47}$$

where

$$\Psi_R(x,t) = \sqrt{\rho_R(x)}\,\exp[i\phi_R(x)]\,e^{-i\mu t}\,, \tag{3.48}$$

$$T = te^{iw}\,, \tag{3.49}$$

with t and w real. The nonlinear solution is then connected to the linear solution by

$$x_0 = 0\,, \tag{3.50}$$

$$b^2 = 2\mu\,, \tag{3.51}$$

$$A = 0\,, \tag{3.52}$$

$$B = t^2\,. \tag{3.53}$$

When the eigenvalue is greater than the effective potential, the nonlinear solutions are therefore adiabatically connected to the linear transmitted wave solutions. The next section connects the decaying evanescent waves with nonlinear solutions.

3.4.2 Evanescent Waves

If the eigenvalue, μ, is smaller than the effective potential then the wave function must decay. In the linear case, the decay is precisely exponential. The Jacobian elliptic sn function solution, Eq. (3.10), of the NLS can provide the appropriate exponential decay. In the limits $g \to 0$ and B, $x_0 \to +\infty$ under the constraints $A{=}{-}B$ and $A\,g/b^2 = 1$, Eq. (3.10) gives

$$\lim_{B,x_0\to+\infty} B\,\mathrm{sech}^2(bx+x_0) = \rho_0\,e^{-bx}\,, \tag{3.54}$$

where ρ_0 is the density at the boundary and is given by,

$$\rho_0 = \frac{4B}{e^{2x_0}}\,. \tag{3.55}$$

When the limit that g approach zero is not enforced,

$$\rho(x) \propto \frac{1}{(N_+e^{bx} + N_-e^{-bx})^2}\,, \tag{3.56}$$

where N_+ and N_- are constants related to the magnitude and sign of the interaction strength. The decay of the density is, therefore, not strictly an exponential decay. It is interesting to note that all decaying solutions, whether linear or nonlinear, must possess a trivial phase. This is due to the restriction that $A{=}{-}B$, and, hence from Eqs. (3.13) and (3.7), the phase must vanish. This is also consistent with the physical interpretation of the phase since a nontrivial phase corresponds to a superfluid velocity and the velocity must vanish if the wave cannot be transmitted.

3.5 Single Boundary Conclusions

The full set of stationary states of the mean field of a Bose-Einstein condensate, modeled by the nonlinear Schrödinger equation in one dimension, in the presence of a potential step or pointlike impurity were presented in closed analytic form. Non-decaying solutions were divided into two categories: localized soliton-like solutions, and solutions that oscillate out to infinity. The localized solutions are of a purely nonlinear character, as they have no linear analog. On the other hand, the oscillating solutions were shown to be adiabatically connected to the solutions to the linear Schrödinger equation.

With a delta function potential, the localized solution can be interpreted as a single bright or dark soliton trapped by the impurity. In addition, it was shown that an impurity can also bind a soliton pair. If the impurity is attractive, the natural repulsion between two dark solitons can be exactly canceled by the attraction of the impurity, while if the impurity is repulsive, it can balance the natural attraction of in-phase bright solitons. Since these solutions are conjected to be stable (see below), they are excellent candidates for the experimental realization of stationary excited states of a Bose-Einstein condensate. In addition, the maximum repulsive interaction strength of the condensate with an attractive impurity that allows for a bound state has been determined.

The oscillating solutions of the NLS, despite being adiabatically connected to oscillating solutions of the Schrödinger equation, have very different properties due to the concept of an effective potential. For the attractive interaction solution for an evanescent wave decaying under a step, as illustrated in Fig. 3.2(b), the eigenvalue is larger than the effective potential in the regions of high density and is less than the effective potential in regions of low density. Figures 3.2(c) and (d) show more radical deviations from the linear solutions since the wave function decay on the lower side of the step.

It is possible to characterize the general solution of the NLS, Eq. (3.10), in terms of physical quantities such as the mean linear number density, $\overline{n}$, mean energy density, $\overline{\mathcal{E}}$, and mean momentum density, $\overline{\mathcal{P}}$. The densities are given by

$$\overline{n} = B + A\Big(\frac{1}{k^2} - \frac{E(k)}{k^2 K(k)}\Big)\,, \tag{3.57}$$

$$\overline{\mathcal{E}} = \overline{n}\mu + \frac{3B^2 g - b^2 A}{6} + \frac{2}{3}(\mu - V)(\overline{n} - B)\,, \tag{3.58}$$

$$\overline{\mathcal{P}} = \alpha\,, \tag{3.59}$$

where μ, α, and k are given by Eqs. (3.12), (3.13), and (3.14), respectively. In general, the number, energy, and momentum densities must be calculated separately for the left and right sides of a boundary. These densities can be used to determine the variables A, B, and b of Eq. (3.10), leaving only the translational offset, x_0, as a free variable determined by the boundary conditions. It should be noted that the factor multiplying A in the mean number density, Eq. (3.57), approaches one half when k approaches zero and approaches one when k approaches unity. This is to be expected since the mean number density of a linear wave is given by $B + A/2$ and the mean number density of an extremely nonlinear wave is given by $B + A$. The mean energy density can easily be calculated from

$$\overline{\mathcal{E}} = \overline{n}\mu - \frac{g}{2}\overline{\rho^2}\,, \tag{3.60}$$

and so the second and third terms on the right side of Eq. (3.58) are due to this

nonlinear correction. Since the mean momentum density, Eq. (3.59), is equal to α, the mean momentum density must be continuous across the boundary due to the boundary condition on α, Eq. (3.19). In addition, the momentum density as a function of position is also given by α, and so the momentum density is equal everywhere.

The healing length, ξ, of the NLS in the quasi-one-dimensional regime, where the transverse dimensions are trapped by a harmonic potential of frequency ω, is given by

$$\xi^2 = \frac{l_{ho}^2}{8\pi a_s \overline{n}}, \tag{3.61}$$

where $\overline{n}$ is given by Eq. (3.57). Since the mean number density can vary across the boundary, it is possible for the condensate to have a different healing length on either side of a boundary. Since the speed of sound in the condensate is inversely proportional to the healing length, the speed with which phonon-like excitations can travel vary as they cross the boundary.

While finding the complete set of solutions to the Gross-Pitaevskii equation, Eq. (3.1), with an impurity or step potential provides much information about the system, only stable solutions are experimentally observable. Previous works have examined the stability of stationary states for a constant external potential (see, for example, [80, 79, 60, 61, 74, 95, 166, 176]), as well as for periodic and harmonic potentials (see, for example, [24, 28]). Most studies are ultimately numerical: linear stability can be solved in a few special cases, while nonlinear stability is analytically intractable. For a constant external potential, single bright and dark solitons and dark soliton trains are stable. A finite number of bright solitons may form bound states, as for example order n solitons ($n > 1$). Bright soliton trains are always unstable. However, they may be experimentally stable since their lifetime may be longer than experiments, which typically require stability timescales of from milliseconds to seconds. Bright soliton trains which have a phase difference $\Delta\phi$ between adjacent peaks such that $-\pi/2 < \Delta\phi < 3\pi/2$ exhibit this experimental stability, with the lifetime being longer the closer $\Delta\phi$ is to π.

Bright soliton trains with $-\pi/2 < \Delta\phi < \pi/2$ are unstable but become quasi-periodic in time in a finite system.

Based on these known results from the case of a constant potential, as well as the from the stability analysis with an impurity performed by Bogdan *et al.* [14], the stability of an attractive condensate with an impurity is as follows. According to Bogdan, the bound state of two bright solitons, as in Fig. 3.4(b), are stable, since, so long as they are strongly overlapping, they will be in phase ($\Delta\phi = 0$) and remain bound to the impurity. This is also the ground state of the system. However, the kind of solution shown in Fig. 3.4(a) is unstable [14]. We now conject on the stability of a repulsive condensate that is not bound and whose density approaches a nonzero constant at infinity. Localized solutions in the case of repulsive nonlinearity are obviously stable in the cases of Fig. 3.3(a)-(b) and 3.3(e)-(f), since they are the ground states. The bound pair of dark solitons, illustrated in Fig. 3.3(c)-(d), should be likewise stable, so long as the impurity is sufficiently strong. All of these solution types, except for attractive solitons bound by a repulsive impurity, are expected to be experimentally observable in finite systems, such as an elongated harmonic trap. An excellent analysis of the stability of solitons pinned with impurities is given by Bogdan, *et. al.* [14]. The stability of soliton trains is a less certain issue. Such a stability study presents a subject for future research.

We emphasize that neither the idea of left and right traveling waves nor that of reflected *plus* incident waves apply to nonlinear wave equation defined by the nonlinear Schrödinger equation. This is important since one cannot create wavepackets from linear combinations of these solutions. Instead, these solutions already contain the wavepacket-like solutions, or solitons, that are necessary to describe the system; moreover, solitons, unlike wavepackets, are nondispersive. Time dependent nonlinear scattering remains an open question that can certainly be addressed via numerical studies. In general, the stationary solutions to the NLS give physical insight into its dynamics, without which

numerical solutions may be difficult to interpret. Perhaps more importantly, using the general nature of the solutions to the cases of a step function and an impurity, it is possible to describe all stationary states to piecewise constant potentials.

In conclusion, we have analytically solved for all stationary solutions to the nonlinear Schrödinger equation with a delta function or a step function potential. This models the steady state behavior of the mean field of a Bose-Einstein condensate in the presence of an impurity, or of a potential step created by, for instance, a laser passing over the edge of a razor blade. Novel wave function were found, including solitons trapped by the impurity and the nonlinear analog of transmitted and evanescent waves.

3.6 A Kronig-Penney Potential and Bloch Waves

We now consider the mean-field model of a quasi-one-dimensional BEC in the presence of a Kronig-Penney potential,

$$V'(x) = V_0' \sum_{j=-\infty}^{+\infty} \delta(x - j\,d)\,, \tag{3.62}$$

where d is the lattice spacing and V_0 is the strength of the potential. When the transverse dimensions of the BEC are on the order of its healing length, and its longitudinal dimension is much longer than its transverse ones, the 1D NLS [145, 29] which describes the stationary states of the mean field of a BEC is given by,

$$-\frac{1}{2}\partial_{xx}\Psi + g|\Psi|^2\Psi + V(x)\Psi = \mu\Psi\,. \tag{3.63}$$

Here m is the atomic mass, μ is the eigenvalue, g characterizes the short range pairwise interaction, and $V(x)$ is an external potential [119].

In Eq. (3.63), the length is scaled according to the lattice spacing d, and the energy has been rescaled by $\pi^2/(2E_0)$, where

$$E_0 \equiv \frac{\hbar^2\pi^2}{2md^2} \tag{3.64}$$

is the kinetic energy of a particle with a wave vector equal to that at the boundary of the first Brillouin zone. The variables in Eq. (3.63) are defined by

$$x = \frac{1}{d}x' , \tag{3.65}$$

$$\mu = \frac{\pi^2}{2E_0}\mu' , \tag{3.66}$$

$$g = \frac{\pi^2}{2E_0}g' , \tag{3.67}$$

$$V(x) = \frac{\pi^2}{2E_0}V'(x'/d) , \tag{3.68}$$

where the primed variables contain the physical units of the system. The renormalized 1D coupling is, $g \equiv na_s\omega md^2/\hbar$, where a harmonic oscillator confinement in the transverse directions has been assumed with frequency ω. Both attractive and repulsive atomic interactions, *i.e.*, $g > 0$ and $g < 0$, shall be considered. The wave function or order parameter, $\Psi(x,t)$, can be written as

$$\Psi(x,t) = \sqrt{\rho(x,t)}\exp[-i\mu t + i\phi(x,t)] , \tag{3.69}$$

where $\rho(x,t)$ is the line density and $v(x,t) = (\hbar/m)\partial\phi(x,t)/\partial x$ is the local superfluid velocity.

In addition to the NLS, Eq. (3.63), the normalization of the wave function is given by,

$$n = \int_0^1 \rho(x')\mathrm{d}x' , \tag{3.70}$$

where n is the number of atoms per lattice site. The boundary conditions induced by the Kronig-Penney potential causes a discontinuity in the derivative of the wave function across each delta function,

$$\lim_{\epsilon\to 0}[\partial_x\rho(j+\epsilon) - \partial_x\rho(j-\epsilon)] = 4V_0\rho(0) , \tag{3.71}$$

where j is an integer. By using the complete set of stationary state solutions to the constant potential case, we can calculate the full set of Bloch solutions for a lattice. The

boundary conditions are used to determine the appropriate values of the free variables, B, b, x_0, and k.

In this section, we use the methods from earlier in this chapter and apply them to a situation in which a lattice of delta functions is present. As is traditionally done in calculating band structures, we seek Bloch wave solutions of the form

$$\Psi(x) = e^{iqx} f_q(x), \tag{3.72}$$

where q is the wave number, $\hbar q$ is the quasi-momentum and $f_q(x)$ has the same period as the lattice, $f_q(x) = f_q(x+1)$. By substituting Eq. (3.72) into Eq. (3.69), one finds that the density, ρ, must also have the same period as the lattice and that the wavenumber and energy per particle can be determined from the density profile by,

$$q = \int_0^1 \frac{\alpha}{\rho(x')} \mathrm{d}x'. \tag{3.73}$$

$$\frac{E[\Psi]}{n} = \frac{1}{n}\int_0^1 \mathrm{d}x \left(\frac{1}{2}|\partial_x \Psi|^2 + \frac{g}{2}|\Psi|^4 + V_0 \delta(x)|\Psi|^2 \right). \tag{3.74}$$

The quasi-momentum is simply the phase jump across each lattice site.

We will examine the quasi-momentum energy bands. The problem reduces to one in which the density is symmetric about the center of the lattice sites, $x = j + 0.5$, where j is an integer. Due to this symmetry, there are only two possible values for the translational offset x_0,

$$x_0 \in \left\{ -\frac{b}{2}, K(k) - \frac{b}{2} \right\}, \tag{3.75}$$

where $2K(k)$ is the period of the density. The offset forces the density in the center of each site to be either a minimum or a maximum of the site, depending on the sign of the interaction.

It is computationally intensive to include the integral in the wavenumber equation, Eq. (3.73), with a root finding algorithm. Therefore, one of the parameters, b, k, or B, is varied while the other two are determined from the number equation, Eq. (3.70), and boundary condition, Eq. (3.71). The offset is then chosen depending on which

energy band is being examined. The wavenumber and energy are evaluated from these parameters and can then be plotted parametrically. In the following section, we discuss the energy bands for repulsive and attractive interatomic interactions.

3.7 Nonlinear Band Structure

The structure of the energy bands is strongly dependent on the strength and sign of the atom-atom interactions, g. In this section, the band structure is examined in four parameter regimes: weakly repulsive, strongly repulsive, weakly attractive, and strongly attractive. Note that in this chapter, a weakly interacting system is defined by $gn/V_0 \leq 1$, and a strongly interacting system is defined by $gn/V_0 \gg 1$.

In Fig. 3.7 and Fig. 3.8, the energy bands for specific cases of weak and strong repulsive interactions are presented, $gn = E_0$ and $gn = 10E_0$, respectively. The condensates are in a repulsive lattice, $V_0 = E_0$. In Fig. 3.7, the interaction strength is small and deviations from the linear band structure are small as well. The bands are vertically shifted higher as compared to a linear system due to the repulsive interactions, which increase the energy of the system. When the interaction strength is further increased the band structure becomes quite different. *Swallowtails* [175], or loop structures, appear in the bands, as in Fig. 3.8. The width of these swallowtails grows as the interaction strength is increased. Swallowtails are a general feature of a nonlinear system in a periodic potential [174] and appear for both repulsive and attractive interactions.

The presence of swallowtails has been conjectured to be due to the hysteretic behavior of the superfluid condensate. A thorough discussion of this topic is given by Mueller [117] (see also references therein). For a completely free, non-interacting system, the energy has a quadratic dependence on the momentum, shown as the dashed parabolic curves in Fig. 3.9. Since a change in wavenumber of 2π leaves the system unchanged, the quadratic dependence is repeated centered around integer multiples of 2π. When a periodic potential is added to the system, bands in the energy are formed,

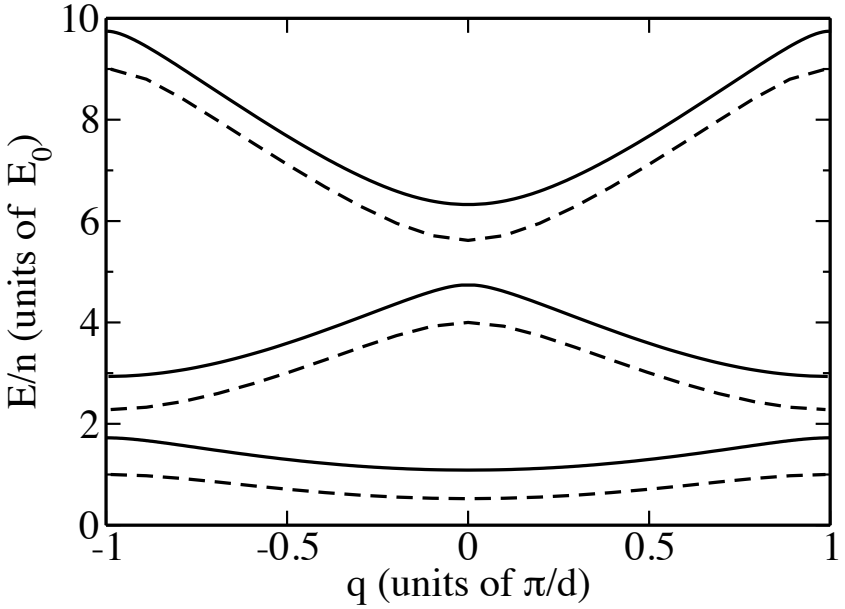

Figure 3.7: Energy per particle as a function of the quasi-momentum for the first three bands of a weakly repulsive condensate ($gn = E_0$) in a repulsive lattice ($V_0 = E_0$). The noninteracting, linear band structure is given by the dashed curves.

shown as the dot-dash sinusoidal curve in Fig. 3.9. An interacting condensate, however, is a superfluid and can therefore screen out the periodic potential [169]. The energy band will then appear similar to that of a free particle, shown as a solid swallowtail curve in Fig. 3.9, until a critical point. At the critical momentum, determined by the average condensate sound speed, the energy band terminates. If this velocity is greater than the edge of the Brillouin zone, there are then two separate energy minima. This demands that there be a saddle point separating them and hence the three stationary states. This discussion can be used to consider condensates with repulsive interactions, but not attractive interactions. We find the appearance of swallowtails for both signs of interaction.

For interacting systems in periodic potentials, there is a minimum interaction strength for which the swallowtails in the energy bands can exist [117]. In general, this can be dependent on both the strength of the potential as well as the band that is being discussed. For a sinusoidal lattice it was shown that the onset of the swallowtail for

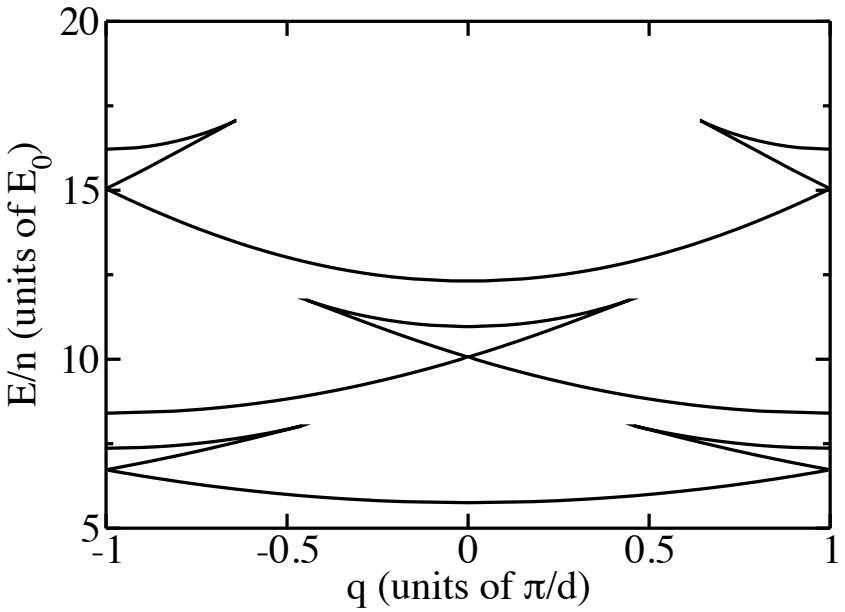

Figure 3.8: Energy per particle as a function of the quasi-momentum for the first three bands of a strongly repulsive condensate ($gn = 10E_0$) in a repulsive lattice ($V_0 = E_0$). Note the appearance of swallowtails at the edge of the Brillouin zone in the odd bands and at the center of the even bands.

the lowest band of a repulsive condensate occurs when the interaction strength and the potential are equal. For higher bands the relationship no longer becomes analytic [107]. For the Kronig-Penney lattice potential, the critical value for the onset of the swallowtails is not dependent on the band under consideration or the sign of the interaction. Numerically, we are able to determine that the onset occurs when $gn = 2V_0$. This holds true in all cases except for the lowest band of an attractive condensate, as will be explained later in the section.

The energy bands are slightly different when the condensate is in an attractive potential, i.e. $V_0 < 0$. At the Brillouin zone boundary, the energy gap between bands is proportional to V_0 for a weakly interacting system. The second band then can cross the first band, since for an attractive potential the gap size is negative. In contrast, the bands are separated by an energy $\rho(0)V_0$ for a repulsive potential. As the interaction strength increases, the effects of the potential become less noticeable and the bands are

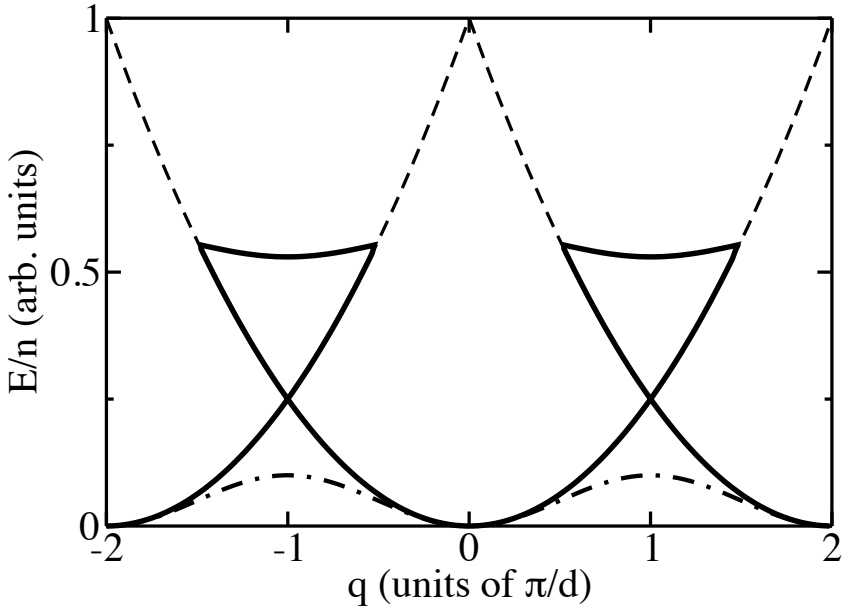

Figure 3.9: Energy per particle as a function of the quasi-momentum wave number for a noninteracting system with no potential (dashed curve), a periodic potential and small or no interaction (dot-dashed curve) and a periodic potential with a large interaction (solid curve).

no longer degenerate. Note that repulsive and attractive sinusoidal potentials create the same band structure. The difference in the current system arises since there are two length scales associated with a Kronig-Penney potential, the lattice spacing and delta function width.

The energy bands for an attractive condensate in a repulsive potential, $V_0 = E_0$, with a small interaction strength, $gn = -E_0$, have a qualitatively similar form as for a weakly repulsive condensate, see Fig. 3.10. Note that the attractive bands are, however, lower in energy than the repulsive bands due to the attractive interaction strength. In contrast to the weakly interacting case, a strongly attractive condensate has several qualitative differences compared to a strongly repulsive condensate.

In Fig. 3.11, the band structure for a large attractive interaction, $gn = -10E_0$, in a repulsive potential, $V_0 = E_0$, is illustrated. The swallowtails in the bands are now on the upper band at the band gaps as opposed to the lower bands at the band gaps as they

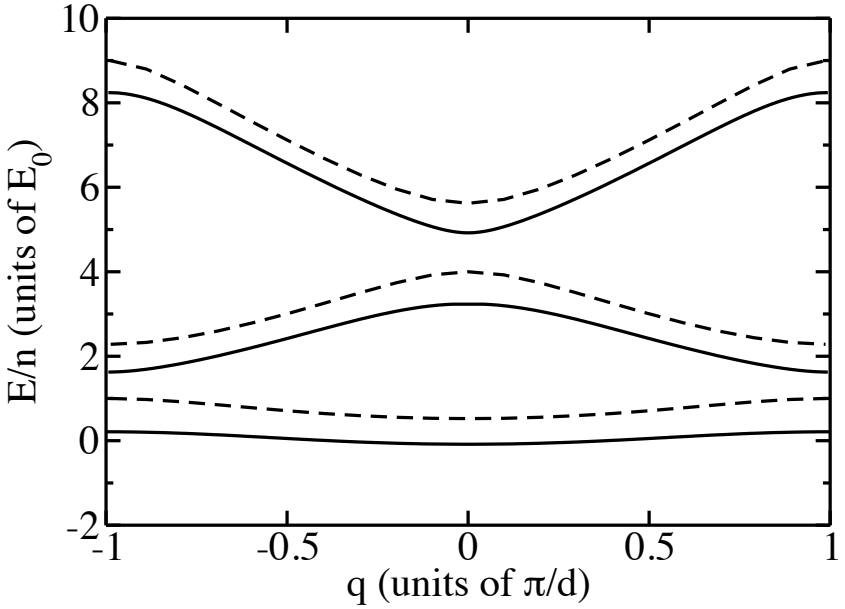

Figure 3.10: Energy per particle as a function of the quasi-momentum wave number for the first three bands of a weakly attractive condensate ($gn = -E_0$) in a repulsive lattice ($V_0 = E_0$). The noninteracting linear band structure is given by the dashed curves.

were for the repulsive case in Fig. 3.8. The first energy band never has a swallowtail because the swallowtail must be on the lower portion of the band and below the center of the band there is no quadratic energy dependence for the swallowtail to follow, see Fig. 3.9.

The higher bands of a strongly interacting attractive condensate can look quite different than those of a strongly interacting repulsive condensate. After the initial critical value of the interaction strength is reached, a swallowtail in the band starts to form, as in the third band of Fig. 3.11. As the interaction strength increases, another critical value is reached where the width of the swallowtail in q reaches π and runs into the band edge. Eventually, the wave number that should be less than zero becomes imaginary due to the form of α. This represents a nonphysical solution and is contrary to the assumption that the phase is real in Eq. (3.69). Therefore, the band appears as two separate curves, a loop and a separate line. These are both marked as Band 2 in Fig. 3.11. It takes on this appearance since the swallowtail cannot extend lower than

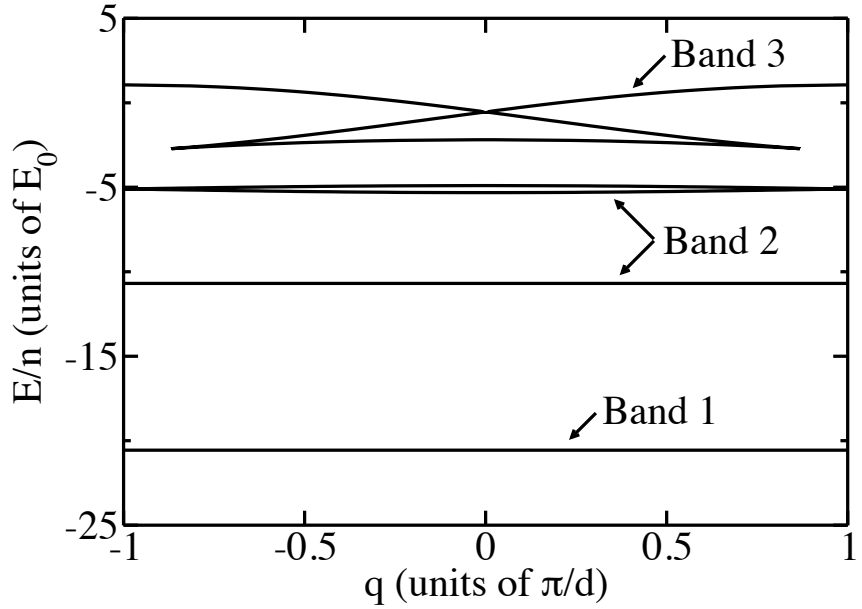

Figure 3.11: Energy per particle as a function of the quasi-momentum wave number for the first three bands of a strongly attractive condensate ($gn = -10E_0$) in a repulsive lattice ($V_0 = E_0$). The first band does not have a swallowtail. However, the second and third bands do have swallowtails. The swallowtail in the second band appears as a loop with an unattached curve since an attractive condensate has a maximum width for the swallowtails, which in the case of the second band is a width of π.

the minimum in the adjacent quadratic energy dependence. In general, the n^{th} band will develop this two-part structure when the swallowtail reaches a width of $(n-1)\pi$ since the swallowtail will then have reached the minimum of the corresponding free particle energy. Note that this phenomenon does not occur for a repulsive interaction since there is no extremum to limit the growth of the swallowtail.

3.8 Density Profiles of Bloch Waves

As density is the primary experimental observable for BEC's, the change in the density profile with wave number is important. Weak interactions create similar changes in the density profile and energy band structure independent of the sign of the interaction. This is because the interaction energies are less than or of the same magnitude as the potential. For strong interactions, the density is in general more sharply peaked for

an attractive condensate and flatter for a repulsive condensate. However, the general ways in which the densities changes are qualitatively similar.

The densities of the weakly attractive condensate in the first band are shown for three different quasi-momenta in Fig. 3.12. The solid curve, dashed curve, and dotted curve are the density profiles for $q = 0$, $q = \pi/2$, and $q = \pi$, respectively. To understand the energy bands in terms of the density profile, the three terms of the energy in Eq. (3.74) should be discussed. The kinetic, interaction and potential energy per particle are given by the first, second, and third terms of Eq. (3.74). Notice that the density at the origin decreases as the wave number is increased. Therefore the potential energy will also decrease due to the delta function at $x = j$, where j is an integer. Because the condensate is attractive, the interaction energy decreases as the wave number is increased since the density becomes more peaked. The kinetic energy increases as the wave number increases since the variations in the density become larger.

The case of the density variations associated with the first band of a strongly interacting repulsive condensate is shown in Fig. 3.13 and is qualitatively similar to that of the weakly attractive case. The solid curve represents the density profile for $q = 0$. The dot-dash curve represents the density when $q = \pi$ at the bottom of the swallowtail. The dashed curve represents the density when $q = 0.46\pi$ at the end of the swallowtail. The dotted curve represents the density when $q = \pi$ at the top of the swallowtail. The density at the origin again decreases as the wave number increases and therefore the potential energy also increases . The interaction energy increases as the band is traversed since the density becomes more peaked. The kinetic energy follows the same qualitative path as the total energy. Of the three, it is therefore the kinetic energy that has the greatest influence on the energy bands.

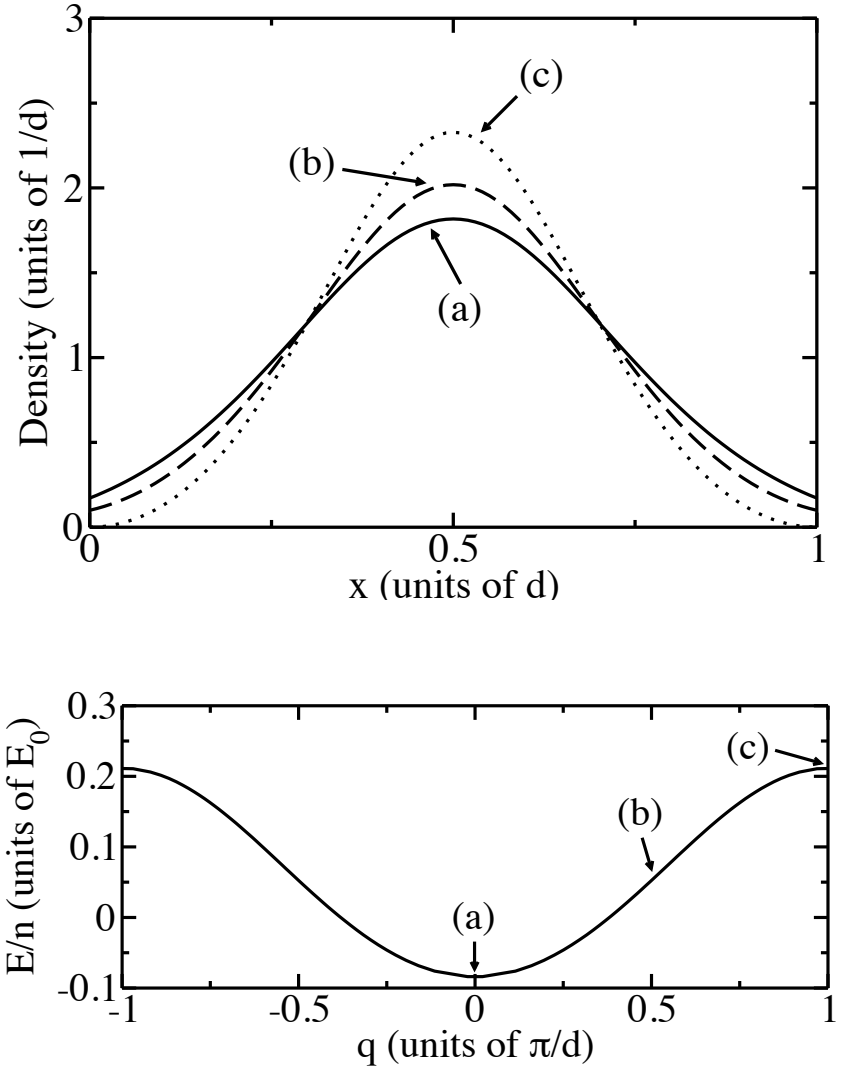

Figure 3.12: Changes in the density of a weakly attractive, $gn = -E_0$, condensate associated with different positions on the first band. The solid curve represents the density when $q = 0$. The dashed curve represents the density when $q = \pi/2$. The dotted curve represents the density when $q = \pi$. The lower plot shows the corresponding positions on the first energy band.

3.9 Stability of Bloch Waves

We now study the stability of the Bloch states and determine the stable regions of the bands. In addition to stable solutions, solutions that have instability times much longer than experimental time scales can be observed in experiments. Recent studies of the stability of condensates in a periodic potential have focused on linear energetic

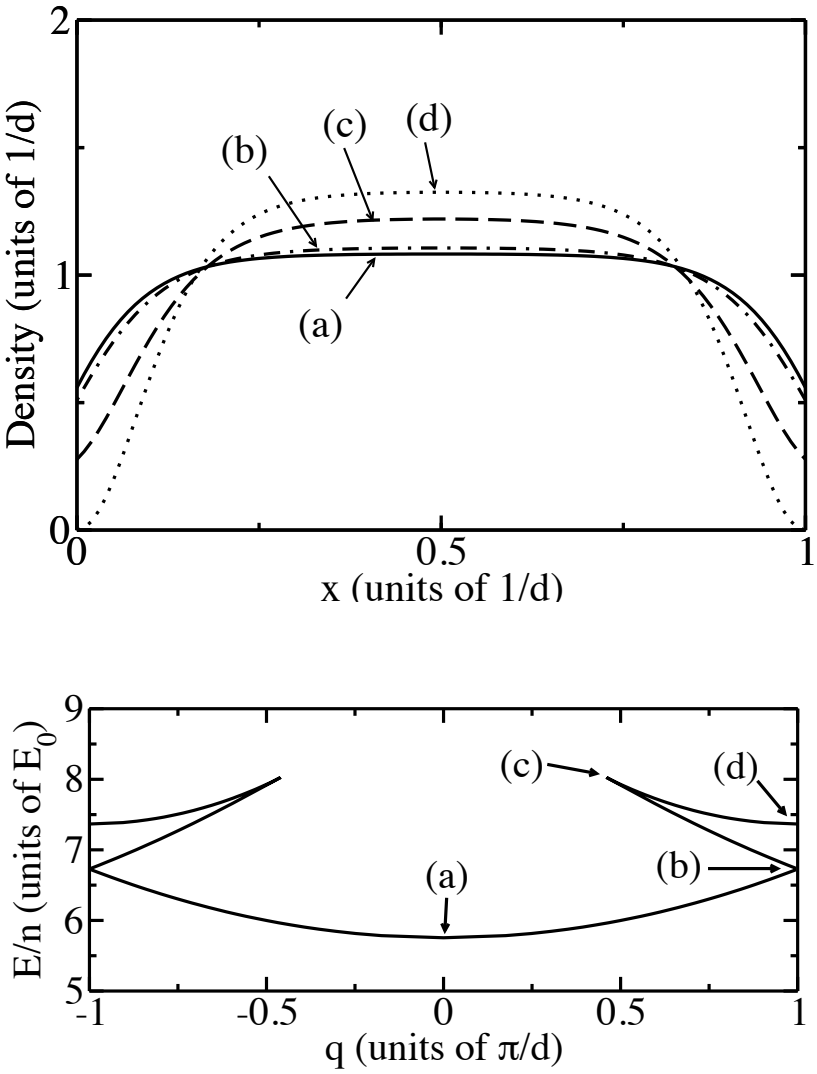

Figure 3.13: Changes in the density of a strongly repulsive condensate, $gn = 10E_0$, associated with different positions on the first band. The solid curve represents the density when $q = 0$. The dot-dashed curve represents the density when $q = \pi$ at the bottom of the swallowtail. The dashed curve represents the density when $q = 0.46\pi$ at the end of the swallowtail. The dotted curve represents the density when $q = \pi$ at the top of the swallowtail. The lower plot shows the corresponding positions on the first energy band.

and dynamic stability, also called Landau stability [168, 23, 106, 107, 50]. In contrast, we consider the full response of the condensate to stochastic perturbations. In order to numerically simulate the NLS with a periodic potential, a ring geometry was used with a quantized phase such that $Nq = 2\pi j$, where q is the wave number, N is the number

of sites and j is an integer. To ensure that the phase quantization does not effect the stability properties, enough lattice sites were used to allow for many rotations of the phase. The outcome of the stability analysis is independent of the number of sites for sufficiently large number of sites. In most cases, $j = 4$ was found to be adequate to extract the correct stability properties.

The delta functions were simulated by single point distortions in the potential grid. They were also implemented by using boxes of varying widths with areas normalized to create the appropriate potential strength. The size of the boxes did not influence the stability properties until the width became approximately 10% of the healing length,

$$\xi \equiv \hbar/\sqrt{2gn}\,. \tag{3.76}$$

The NLS was evolved using a variable step fourth-order Runge-Kutta algorithm in time and a filtered pseudo-spectral method in space. The noise introduced into the simulations comes from the round off error associated with numerical simulations. To ensure that the form of the noise from round off error did not affect the stability properties of the system, initial stochastic white noise of various levels was introduced into the Fourier spectrum. For levels significantly greater than the round off noise, the stability times approached those from the round off noise. Introduction of white noise at the level in the eighth significant digit produced the same instability times as the round off noise, which effects the sixteenth significant digit. All simulations were performed over time scales longer than experimental lifetimes of the BEC, which are on the order of seconds.

The time at which the onset of instability occurs is determined by the effective variance in the Fourier spectrum,

$$\sigma(t) \equiv \sqrt{\frac{\sum_p (f(p,t) - f(p,0))^2}{2\sum_p (f(p,0))^2}}\,, \tag{3.77}$$

where $f(p,t)$ is the Fourier component of the wave function at momentum, p, and time, t, and the sum is over the momentum. This quantity determines how different the

Fourier spectrum is compared to the original stationary state. It vanishes when the two spectra are identical and approaches unity when there are no Fourier components in common. When $\sigma(t)$ reaches 0.5, i.e. 50% of the Fourier spectrum is different than the original, the system is considered to have become unstable.

Unless otherwise noted, for the stability analysis the lattice spacing is given by $d = 1$ μm, the approximate length scale with which current optical lattices are created. In addition, all instability time scales will be given for ^{87}Rb.

3.9.1 Attractive Atomic Interactions

With an attractive interaction of $gn = -E_0$ in a repulsive potential of $V_0 = E_0$ (see Fig. 3.10), the lowest energy solution, zero quasi-momentum in the lowest band, has a lifetime greater than experimental time scales. However, when even a slight harmonic perturbation to the potential is added to the initial time step the condensate becomes rapidly unstable. For instance, with a harmonic frequency of 120 Hz, which is approximately the experimental trapping frequency [115], simulations show an instability at 1.5 ms. This is short compared to the lifetime of a BEC [115], but still observable.

When the quasi-momentum of the first band is increased, the stability of the system becomes dependent on the effective mass. The effective mass, m^*, is defined as,

$$m^* \equiv \frac{1}{\partial^2 E/\partial q^2} \,. \tag{3.78}$$

The physical meaning of the effective mass is the mass that the particle would appear to have if the potential was not being considered [4]. The sign of the effective mass can be transferred to the interaction strength, changing an attractive interaction to an effective repulsive interaction. Therefore, when the quasi-momentum increases and the energy band becomes concave down, $m^* < 0$, the system enters a regime of stability. The system remains stable even in the presence of a harmonic perturbation.

For zero quasi-momentum in the second band, the system immediately develops

temporally periodic variations in the phase and density. There is an additional instability, occurring on the order of 5 ms, that destroys the periodicity of the system. One might expect that this part of the band be stable since there is a negative effective mass, but the oscillations due to the two density peaks per lattice site force the system to be unstable. The oscillations, although periodic in time, create a larger underlying instability to grow.

The stability properties of a strongly attractive condensate are similar to those of a weakly attractive condensate. The stability of the first band is determined by the effective mass while higher bands always go unstable. Therefore, for an attractive condensate, the system of Bloch waves is stable only if there is one density peak per lattice site and the effective mass is negative.

3.9.2 Repulsive Atomic Interactions

Like an attractive condensate, a repulsive condensate only has stable regions on the first band. For a weakly interacting repulsive condensate, $gn = E_0$ and $V_0 = E_0$, the effective mass in the first band is positive between $q = 0$ and $q = \pi/2$. The effective mass becomes negative for larger quasi-momentum, since the energy becomes concave down. Hence the system becomes unstable. For a wave number of $q = 9\pi/16$ the instability time is 10 ms. This decreases to 2 ms for $q = \pi$. In this regime, with negative effective mass, the actual ground state is an envelope soliton that can spread over many lattice sites. These types of states are called gap solitons [101, 76, 105, 45] and only occur in interacting systems. Figure 3.14 presents the unstable evolution of the weakly repulsive condensate in the first band with a wave number of $q = \pi$ in Fourier space. Notice that the instabilities arise from perturbations around the primary Fourier components of the wave function. In Fig. 3.15, the effective variance, σ, is plotted as a function of evolution time. The system becomes unstable around 2 ms. The second band becomes unstable in 0.5 ms for $q = 0$ and in 6 ms for $q = \pi$. Therefore, the system is stable in the

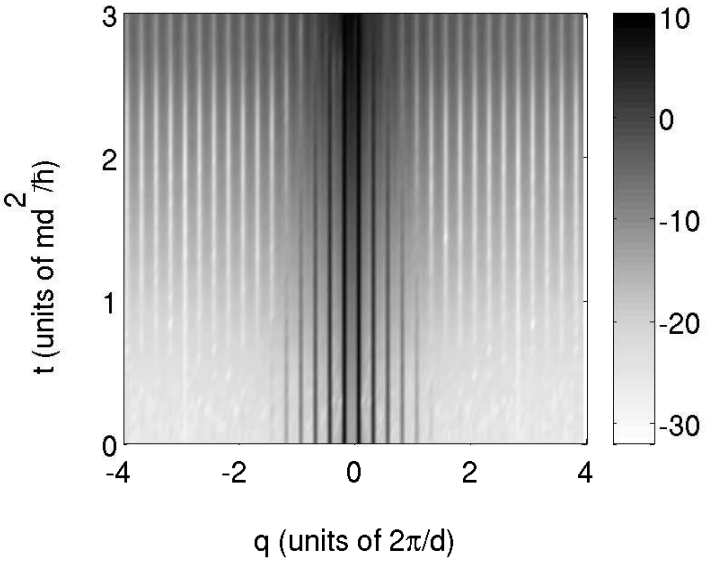

Figure 3.14: Logarithm of the Fourier spectrum during the time evolution. Time is in units of $\hbar/E_0$ and distance in units of the lattice spacing.

first band with positive effective mass and unstable elsewhere. This is consistent with the effects that the effective mass has on stability in systems described by the lowest band DNLS. In a work by Fallani *et al.* [50], the instability time of a condensate in a lattice was measured by using an RF-shield to remove the hottest atoms produced by the heating created in the sample by instability. The loss rate, equal to the inverse of the lifetime, should then be qualitatively similar to the instability time. Our calculations are consistent with these experimentally observed loss rates of a BEC in an optical lattice [50].

Due to the presence of the swallowtails, the strongly interacting system provides different stability regimes. For a repulsive condensate with $gn = 10E_0$, in a repulsive lattice with $V_0 = E_0$, the main section of the first band, as well as the lower portion of the swallowtail, have positive effective mass and remain stable. A small portion at the edge of the band still has a negative effective mass and is unstable. The upper portion of the swallowtail, as discussed in Sec. 3.7, is an energy maximum and is not expected

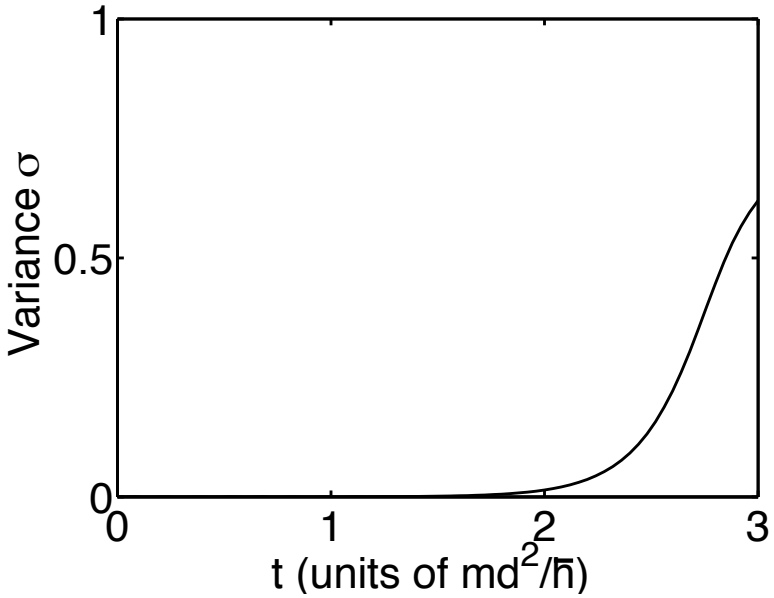

Figure 3.15: The time evolution of the effective variance of the momentum density, σ. Time is in units of $\hbar/E_0$.

to remain stable. Our simulations find that the instability time of the upper portion of the swallowtail is approximately 0.2 ms, independent of the actual quasi-momentum.

The size of the lattice spacing can influence the time scales for which the system becomes unstable. In Fig. 3.16, the instability time is presented as a function of the lattice spacing for a repulsive condensate, $gn = E_a$, in a repulsive lattice, $V_0 = E_a$, with a wave number of $q = \pi$, where $E_a \equiv \hbar^2\pi^2/2m(1\mu m)^2$.

There is a minimum instability time as the lattice spacing varies that occurs when the lattice spacing is approximately twice the healing length, ξ. The instability time is given by half of the interaction strength time, $gn/\hbar$. When the lattice spacing is much larger than the healing length, the density becomes extremely flat except at the delta functions, where the density deformations take the form of pinned dark solitons. Since the lattice spacing is large, the dark solitons are far apart and are effectively noninteracting pinned solitons. Dark solitons are known to be robustly stable [95, 24]. Therefore, for a lattice spacing much larger than the healing length the system becomes

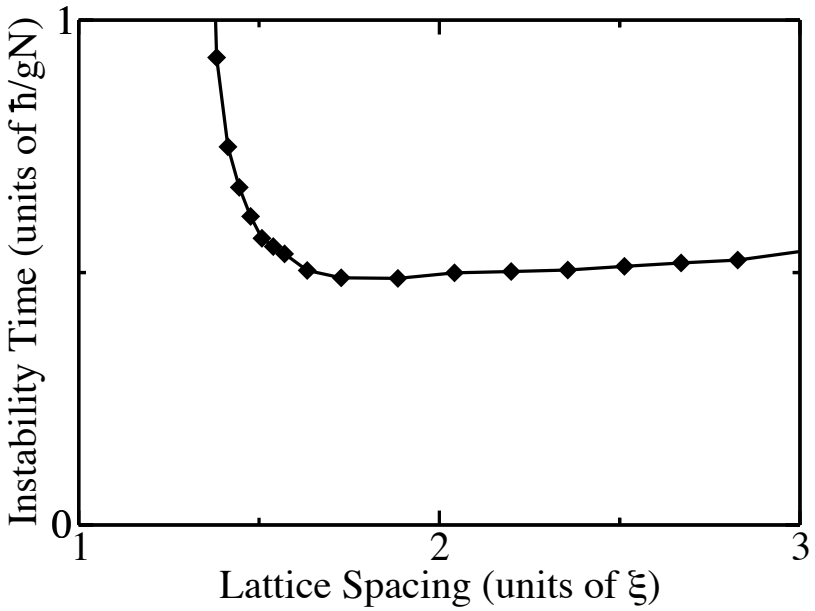

Figure 3.16: The instability time as the lattice spacing is varied. Time is in unit of $\hbar/gn$ and distance in units of the healing length, $\xi = \hbar/\sqrt{2gn}$.

stable. For lattice spacing smaller than twice the healing length, the condensate does not distinguish between the separate delta functions and, therefore, experiences closer to a constant potential. In this regime, the kinetic energy becomes much greater than the interaction energy and potential energy since variations in the density occur on the length scale of $d/2$, which is less than the healing length. The system becomes effectively free and noninteracting and, therefore, approaches stability.

3.10 Analytical Methods in Nonlinear Band Theory

The band structure of a BEC in an optical lattice has previously been studied both analytically and numerically. An array of techniques have been developed. The sinusoidal potential, which is the experimental case, has been investigated by expanding the wave function in a Fourier series and minimizing the energy [175, 43, 173, 107, 106]. Two other potentials have been studied in detail. A Jacobi elliptic potential, which asymptotically approaches the sinusoidal case, has the advantage that it admits a useful

class of exact solutions [23, 24, 22]. On the other hand, the Kronig-Penney potential can be solved completely and exactly, as we have shown previously [153, 152]. A work by Li and Smerzi followed a similar line of analysis [102]. We compare these three models with the aid of the Bloch wave representation. For the Jacobi elliptic potential this requires a reinterpretation of the original result [23]. In addition, we explain the long standing open problem of why certain density offsets in this class of solutions lead to instability. We find that the form of the potential has no effect on the superfluid and other physical properties of the system. Of the closed-form analytical methods available for the three potentials, only the Kronig-Penney potential admits a full description of the band structure.

Of the many methods used in nonlinear band theory, analytical methods allow for greater flexibility in describing solution types, as they result in general expressions which describe all parameter regimes simultaneously. In this section, we compare three methods that use different periodic potentials and interpret their solutions in the Bloch wave representation. It is found that they all produce the same band structure for the lowest band. Hence, the exact form of the potential is unimportant.

3.10.1 Solution by Cancellation

The first analytical method for obtaining solutions to the NLS with a periodic potential in the context of a BEC was given by Bronski, et. al. [23] for a Jacobi elliptic potential of form

$$V(x) = -V_0(1 - 2\,\mathrm{sn}^2(2K(k)x, k))\,, \tag{3.79}$$

where sn is one of the Jacobi elliptic functions [1]. The Jacobi elliptic functions are generalized periodic functions characterized by an elliptic parameter $k \in [0, 1]$. They approach circular and hyperbolic trigonometric functions as $k \to 0$ and $k \to 1$, respectively. For k not exponentially close to unity, the potential is similar to the sinusoidal case. As k approaches unity, the period of the lattice becomes much greater than the

width of the localized variations of the potential, thereby approaching a lattice of delta functions, i.e., a Kronig-Penney potential. The period of the lattice is $2K(k) \in [\pi, \infty]$ where $K(k)$ is a complete elliptic integral of the first kind [1].

Bronski *et al.* were able to show that it is possible to choose a suitable ansatz for the density such that the nonlinear term cancels the potential term, thereby leaving a system that is effectively free. They found a special class of solutions with a period equal to that of the lattice, where the density was assumed to be of the form

$$\rho(x) = A\,\mathrm{sn}^2(bx, k) + B\,. \tag{3.80}$$

The following conditions must then be met:

$$A = \frac{b^2k^2 + 2V_0}{g}\,, \tag{3.81}$$

$$\alpha^2 = B(B + A)(b^2 + Bg - \frac{2BV_0}{A})\,, \tag{3.82}$$

$$\mu = \frac{1}{2}(b^2 + Ag + 3Bg) - \frac{BV_0}{A}\,. \tag{3.83}$$

Machholm *et al.* [107] showed that this solution corresponds to the edge of the Brillouin zone for the exactly sinusoidal case, $k = 0$. If the parameters of the potential, V_0, k, and b, and the interaction strength gn are set, the wave function is completely determined without any free parameters. Nevertheless, the solutions are of more general use. In fact, although not described in this way by the original authors, this family of solutions can be used to map out the whole lowest energy band. It is possible to change the elliptic parameter k to get a spectrum of solutions. Since the Jacobi elliptic functions closely approximate the trigonometric functions for all k except exponentially close to unity, there is a wide range of values for k where the potential is approximately sinusoidal. In addition, the sign of the potential coefficient V_0 does not significantly change the form of the potential and so this is another parameter that can be changed to determine the energy bands. Therefore, when the elliptic parameter is varied, and the solutions determined via Eqs. (3.80)-(3.83), the complete lowest energy band can

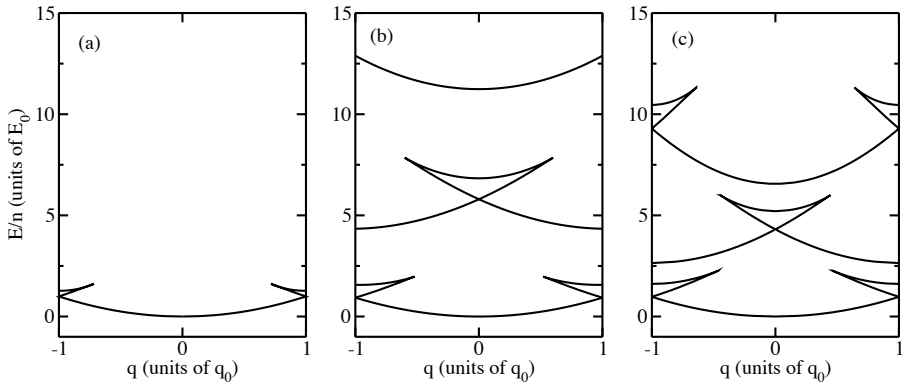

Figure 3.17: Band structure for a strongly repulsive condensate, $gn = 10$, in a periodic potential. Shown are results obtained via the analytical methods of (a) Bronski *et al.* [23] with a Jacobi elliptic potential ($|V_0| = 1$), (b) Machholm *et al.* [107] with a sinusoidal potential ($V_0 = 4$), and (c) Seaman *et al.* [153] with a Kronig-Penney potential ($V_0 = 1$).

be analytically determined for arbitrary interaction strength.

An example of the band structure for strong nonlinearity is shown in Fig. 3.17(a). The interaction strength is chosen to be a factor of ten larger than the strength of the potential, causing the appearance of swallowtails. Only the lowest energy band can be extracted with this class of solutions. This shows that these simple exact solutions are sufficient to describe measurable properties of the condensate such as breakdown of superfluidity for critical values of the nonlinearity [117, 50].

In the work of Bronski et al. [23, 24], the linear stability properties of the solutions were proved for the case of constant, or trivial phase. No such proof was discovered for the case of non-trivial phase solutions. The latter are, for example, the only stable ones in the exactly sinusoidal case of $k = 0$. It was found numerically that non-trivial phase solutions for repulsive condensates with large offsets B were stable, while for smaller B they were unstable. No explanation for this stability property was found. After we recast the solutions in Bloch form and used them to determine the band structure, the stability properties become immediately apparent. Solutions on the upper edge of the swallowtail are known to be unstable, as they represent an energy maximum [117, 107, 153]; these

correspond to small B. Solutions on the main part of the band and the lower edge of the swallowtail represent an energy minimum and are stable; these correspond to large B. For instance, in Fig. 3.17(a), the main part of the band from $q = 0$ to $q = 1$ corresponds to $B \in [0.559, 0.509]$; the lower edge of the swallowtail near the edge of the Brillouin zone corresponds to $B \in [0.509, 0.277]$; and the upper edge, which is unstable, corresponds to $B \in [0.277, 0]$. We note that, in comparing with Bronski *et al.*, they normalized the wave function to gn rather than having gn as the coefficient of the nonlinearity in the NLS. In their numerical studies of stability, they did not hold their normalization (our nonlinear coefficient) fixed. In Fig. 3.17(a), we fix the nonlinearity to be $gn = 10|V_0|$.

3.10.2 Solution by Three Mode Approximation

In a subsequent work by Machholm, et. al. [107], a more complete method to determine the nonlinear band structure was introduced that used a sinusoidal potential

$$V(x) = 2V_0 \cos^2(\pi x)\,. \tag{3.84}$$

The wave function was expanded in a Fourier series for a particular quasi-momentum and the energy was minimized. This method uses the exact physical form of the typical experimental lattice potential that a BEC is held in but requires the root finding of many free parameters. Machholm *et al.* showed that one can obtain analytical solutions by using a three-mode Fourier spectrum:

$$\Psi(x) = \sqrt{n}e^{iqx}(a_0 + a_1 e^{i2\pi x} + a_{-1}e^{-i2\pi x})\,, \tag{3.85}$$

where a_0, a_1 and a_{-1} are real coefficients. Due to the normalization condition on the wave function, there are two real free parameters of the solution.

Using the three-mode expansion of the wave function, it is possible to extract the first two bands and the lower part of the third band, as shown in Fig. 3.17(b). Notice that, unlike with the previous method, full information from the first two bands can

be extracted, instead of only the lowest band. However, the three-mode approximation overestimates the width of the swallowtails [107]. If more Fourier components are included, for a total between five and ten, the first three bands can be described to within 1% accuracy. For higher bands even more Fourier components are needed. This method was later extended to include period-doubled states [106].

In addition to determining the band structure, Machholm *et al.* were able to determine several analytical expressions associated with the stability properties of the condensate. In particular, the interaction strength at which swallowtails first appear in the lowest band, and the width of the swallowtails for a given interaction strength were determined analytically. Studies of the stability of the condensate to small perturbations were also performed.

3.10.3 Solution via a Piece-wise Constant Lattice

In the previous section, a lattice of delta functions, a Kronig-Penney potential, was used

$$V(x) = V_0 \sum_{j=-\infty}^{+\infty} \delta(x - j)\,. \tag{3.86}$$

We presented the complete set of Bloch waves solutions in analytical form by solving the piece-wise-constant potential case and using the appropriate boundary conditions to fix the parameters of the solution. The potential, however, is quite different from the experimentally created sinusoidal lattice. The optical lattice potential is composed of a single Fourier component while the Kronig-Penney potential is a comb of equally weighted Fourier components. We proved that the most general form of the density over a finite interval of constant potential is given by

$$\rho(x) = B + \frac{k^2 b^2}{g} \mathrm{sn}^2(bx + x_0, k)\,, \tag{3.87}$$

where again sn is one of the Jacobi elliptic functions. The chemical potential μ and phase prefactor α are given by

$$\mu = \frac{1}{2}[b^2(1+k^2) + 3Bg]\,, \tag{3.88}$$

$$\alpha^2 = B(k^2b^2/g + B)(b^2 + Bg)\,. \tag{3.89}$$

The energy bands can be determined by varying one of the parameters in the wave function, such as B or b, and determining the quasi-momentum and the energy from Eqs. (3.73) and (3.74). In particular, the parameter scaling b was varied since it is closely related to the quasi-momentum. The offset B and elliptic parameter k are determined by number conservation and the boundary conditions across the delta functions.

The first three bands for the Kronig-Penney lattice are presented in Fig. 3.17(c). Although only the first three bands are presented, our method can be used to determine the higher bands with no additional computational intensity, unlike the technique of Sec. 3.10.2. For all energy bands, all that is required computationally is the root finding of two parameters, the offset B and the elliptic parameter k. The stability properties of the condensate were then numerically determined by dynamically evolving an initial state composed of the stationary solution plus a small amount of white noise. It was found that the stability of the energy bands depended on the interaction strength. For weak nonlinearity, the bands become unstable for quasi-momentum greater than approximately $\pi/2$. For strong nonlinearity, the tops of the swallowtails are unstable but the remainder of the first band is stable. The second and higher bands are always unstable.

In spite of the differences in the potentials, all three methods find a similar nonlinear band structure. In addition, the stability properties of the three models are also the same. Therefore, to study the main physical aspects of this system, any method can be used. All three methods are useful in determining the first band. For the full band structure, only our method is analytically and numerically tractable.

3.11 Periodic Potential Conclusions

The full set of Bloch wave stationary states of a Bose-Einstein condensate in a Kronig-Penney lattice potential, with period commensurate with the lattice, have been presented analytically for both repulsive and attractive interactions. The quasi-momentum energy bands were found to exhibit a cusp at the critical interaction strength $gn = 2V_0$, where g is the interatomic interaction strength, n is the linear density, and V_0 is the lattice potential strength. For larger interaction strengths, swallowtails form in the bands. These swallowtails have the same qualitative form as for a sinusoidal potental and exhibit the same stability properties.

Both attractive and repulsive condensates were found to be dynamically stable only in the first band and when the effective interaction, $\mathrm{sgn}(m^*)g$, was positive. Also, even in the first band, the upper edges of swallowtails were always unstable. Therefore, for an attractive condensate, the only stable Bloch states exist in the first band between the wave number where m^* becomes negative and $q = \pi$. A repulsive condensate is only stable in the first band from $q = 0$ to the wave number where m^* becomes negative. Higher bands are always unstable, for both attractive and repulsive condensates. When solutions became unstable, our numerical studies consistently observed that the instabilities originated around the primary Fourier components of the wave function. This is in agreement with the formal proof of the instability of constant phase Bloch-wave solutions by Bronski *et al.* [24]. The instability time was found to be a function of the lattice constant. If the delta functions are spaced either smaller than or much larger than the healing length of the condensate, the solutions had instability times longer than lifetime of the BEC. Thus experiments could access formally unstable sections of the energy bands, and, by controlling the ratio of the healing length to the lattice constant, directly observe the dynamics of instability. The results of our stability analysis are consistent with the experimental work performed by Fallani *et al.* [50], in which the loss

rate, the inverse of the lifetime, was determined by removing the hottest atoms with an RF-shield.

We also found that for a repulsive condensate with a swallowtail, almost the entire energy band is concave up and, hence, the effective mass is nearly always positive. This is in contrast to a weakly repulsive condensate, where the concavity of the energy band changes, creating a region of negative effective mass. Therefore, there is a maximum interaction strength for which gap solitons [101, 76, 105, 35, 45] can be formed since they require a negative effective mass. The maximum interaction energy is given by $gn = 2V_0$, the strength at which swallowtails appear.

It should be noted that the solutions given in the chapter map onto both the linear Schrödinger equation and discrete nonlinear Schrödinger equation (DNLS) limits if the proper procedure is followed. In the limit that

$$\lim_{g,k\to 0} k^2/g \to A/b^2 \tag{3.90}$$

the linear dispersion relation for the linear Schrödinger equation is recovered. In the limit that

$$\frac{V_0}{gn} \gg 1 \tag{3.91}$$

one obtains the DNLS,

$$i\partial_t \psi_j = \epsilon_j \psi_j + J_j(\psi_{j+1} + \psi_{j-1}) + U_j|\psi_j|^2\psi_j \,, \tag{3.92}$$

where ϵ_j, J_j, and U_j are obtained via the Wannier formalism [133].

Stationary solutions to the NLS with a Kronig-Penney potential need not take the form of Bloch states. Solutions with a period which is an integer multiple of the lattice period have been shown to exist for the sinusoidal potential [106] and are expected also to be present for the Kronig-Penney potential. Envelope solutions, such as gap solitons, also play an important role in other systems modelled by the NLS and have been observed in BEC's [45]. The analytic methods which we have described here are equally applicable to these solution types and form the subject of future study [153].

3.12 Two Color Lattice

There has been great interest in the study of Bose-Einstein condensates (BEC's) from both the experimental and theoretical perspectives since BEC's were first created in 1995 [6, 39, 19]. In particular, the examination of BEC's in periodic potentials in the superfluid phase has yielded many intriguing phenomena, such as gap solitons [45, 7], the appearance of swallowtails or loops in the band structure, pulsed atom lasers and demonstrations of their phase coherence [5, 70], and matter-wave diffraction [121]. BEC's in periodic potentials, unlike other solid state systems, have the advantage that the lattice geometry and interatomic interactions are highly controllable [136, 81]. We examine the mean field Bloch states of a BEC in one-color and two-color potentials for arbitrary interaction and potential strengths. The full nonlinear band structure of the system is then determined for a two-color potential. We show that period-doubled states in the usual one-color lattice are directly connected with Bloch waves in the two-color case. Period-doubled states have a periodicity which is twice that of the underlying lattice. This allows for a novel interpretation of swallowtails, a key physical property of the band structure of a BEC. The study of period-doubled states has been important in other systems, for instance in optics [144, 158], because it offers experimental access to the period-doubling route to chaos.

The two-color lattice has already received some attention in the literature. Roth and Burnett showed that when the period of the second lattice is much longer than the first, so that it forms an envelope, new quantum phases are introduced into the quantum problem [138]. We will consider the superfluid phase only, which is obtained when the lattice height is on the order of or smaller than the chemical potential. Very recently, Louis *et al.* have studied gap solitons in a two-color lattice for which the second lattice has half the period of the first [104]. We study the same potential, but for Bloch waves, rather than gap solitons. Bloch waves have the same period

as the lattice, whereas gap solitons are envelope solutions. Using the Kronig-Penney potential, we link the period-doubled states of the one-color lattice to Bloch waves in the two-color case. Adiabatically turning off one of the frequencies in a two-color lattice, one can clearly observe the origin of swallowtails. Unlike previous explanations of this intriguing property of nonlinear periodic systems [117], ours encompasses both repulsive and attractive BEC's.

Experiments on BEC's in optical lattice potentials proceed as follows. Alkali-metal bosonic atoms are cooled to the quantum degenerate regime. The interference pattern of two counter propagating lasers is used to create a sinusoidal potential shift caused by the ac Stark effect induced by the dipole interaction with the laser field on the atoms' center of mass motion [110, 41]. A small frequency detuning of one of the lasers allows for examination of the different quasi-momentum states and their stability properties by creating a traveling wave interference pattern moving at the velocity $v = (\lambda/2)\delta\nu$, where λ is the wavelength of the first beam and $\delta\nu$ is the detuning [49, 124, 50]. The two-color lattice can then be created by the superposition of two lasers with frequencies which differ by a factor of two. This can be achieved using second harmonic generation with nonlinear crystals. Complex lattice configurations with several lasers have already been performed experimentally [68]. We present a dynamical study of key observables for the two-color lattice, such as the instability time, that can be experimentally investigated with minor changes to current apparatus. There have been many theoretical studies of stability properties of BEC's in one-color lattices (see [23, 24, 22, 164, 76, 89, 105], to name a few), though not of the two-color case.

The band structure is modified from the well-known solutions of the linear Schrödinger equation with a periodic potential. There are two physical regimes [153]. For $|g|n \leq V_0$, which we term the regime of weak nonlinearity, the linear band structure is simply perturbed up or down, depending on the sign of g. For $|g|n \gg V_0$, which corresponds to

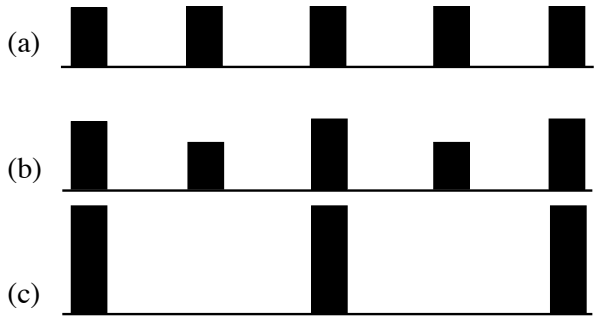

Figure 3.18: A sketch of the potential is illustrated for the three cases of Figs. 3.19 and 3.20, with appropriately normalized boxes representing delta functions: (a) a one-color lattice of period d and $\Delta = 0$; (b) a two-color lattice with a small difference in the potential strengths, period $2d$ and $\Delta = 0.2$; (c) a one-color lattice with period $2d$ and $\Delta = 1$. Adiabatically tuning the system from (a) to (c) allows for a novel explanation of the appearance of swallowtails in the band structure.

the regime of strong nonlinearity, the bands wrap back around on themselves to form loop structures, or swallowtails. These swallowtails have previously been described in terms of the superfluid screening properties of the condensate [117]. This explanation is only valid for repulsive condensates, despite the fact that swallowtails also appear in the attractive case. This motivates the need for another explanation, which we provide in following section.

3.13 The Two Color Lattice and Formation of Swallowtails

Current experiments with BEC's utilize only one-color lattices in the weakly nonlinear regime. Therefore there has been no experimental observation of the swallowtail structure, which requires strong nonlinearity. Two-color lattices, on the other hand, allow one to produce swallowtails even for weak nonlinearity, as we shall show in the following. Moreover, adiabatically tuning the two-color lattice allows for an explanation of swallowtails for both repulsive and attractive BEC's.

A two-color lattice is produced by adding a second frequency component of twice the fundamental frequency, or half the period. Such a straightforward modification of existing experiments can be made via second harmonic generation with nonlinear

crystals. In Sec. 3.10 we showed that the exact form of the potential is unimportant. Therefore, to study the two-color lattice, we use a Kronig-Penney-like potential with delta functions of two different strengths:

$$V(x) = V_0 \sum_{j=-\infty}^{+\infty} \left[(1-\Delta)\delta(x-2j) + (1+\Delta)\delta(x-2j+1)\right], \tag{3.93}$$

where $\Delta \in [0,1]$. The strengths of the two sublattices are $(1-\Delta)V_0$ and $(1+\Delta)V_0$, respectively. The form of Eq. (3.93) allows the potential to be tuned continuously from the one-color lattice of strength V_0 and period d ($\Delta = 0$) to the one-color lattice of strength $2V_0$ and period $2d$ ($\Delta = 1$). This holds the average potential strength constant. For $0 < \Delta < 1$ the potential is two-color. Figure 3.18 sketches the progression between the two lattices, where the delta functions are represented by square functions of fixed width and varying heights. We will show how period-doubled solutions of the $\Delta = 0$ lattice map onto Bloch-wave solutions of the $\Delta = 1$ lattice, including the swallowtails.

The stationary states of the NLS with the potential of Eq. (3.93) are determined in the same manner as was described in Sec. 3.10.3, with the addition of a second boundary condition. Period-doubled solutions can be obtained via the transformation $\Psi(x) = f_q(x)\exp(i2qx)$, while Bloch solutions were found via $\Psi(x) = f_q(x)\exp(iqx)$. In general, one can obtain solutions of the form $\Psi(x) = f_q(x)\exp(imqx)$, with m an integer; we focus on the period-doubled case, $m = 2$, and the Bloch wave case, $m = 1$.

We first illustrate period-doubled solutions for the lattice of Fig. 3.18(a), $\Delta = 0$. There are two types of period-doubled solutions, trivial and non-trivial. The trivial period-doubled solutions simply reproduce the Bloch waves. That is to say, solutions of period d are also trivially solutions of period $2d$. These are illustrated in Fig. 3.19(a) as thin curves for the case of weak nonlinearity. Period-doubled solutions extend across a Brillouin zone of half the quasi-momentum-domain as that of Bloch waves. Thus the domain of Fig. 3.19 ($q \in [0,1]$) is half that of Fig. 3.17 ($q \in [-1,1]$). The bands are required to be symmetric around the center of the Brillouin zone. One reflects

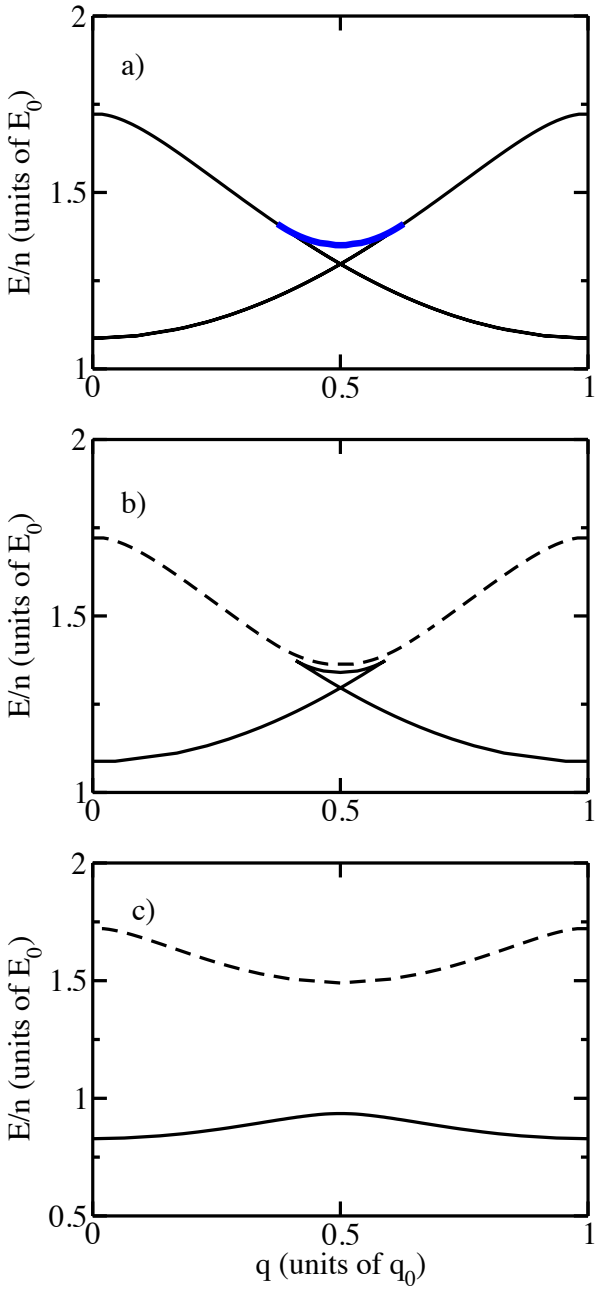

Figure 3.19: Band structure for a two-color lattice with weak nonlinearity, $gn = V_0$. (a) Shown are period-doubled solutions for a one-color lattice of period d and $\Delta = 0$ (Thin black curve: trivial solutions; thick blue curve: non-trivial); (b),(c) Bloch-wave solutions with period $2d$ (Solid curve: lowest band; dashed curve: second band). (b) A two-color lattice with $\Delta \ll 1$. Note that the central swallowtail is derived from the non-trivial period-doubled solution of panel (a). (c) A one-color lattice with $\Delta = 1$. The swallowtail has disappeared due to the weak nonlinearity. The lattices associated with (a)-(c) are sketched in Fig. 3.18.

the band in the right half of the Bloch Brillouin zone around its center at $q = 0.5$ to obtain the trivial period-doubled solutions. This leads to the two branches which make the form of an 'x' in Fig. 3.19(a) (thin black curves). The non-trivial period-doubled solutions are shown as a thick blue curve in Fig. 3.19(a). These form a saddle between the trivial solution branches. The form of the density for the non-trivial period-doubled solutions is shown as the solid curve in Fig. 3.21. The non-trivial solutions are caused by the nonlinearity in Eq. (3.1); they have no analog in the linear Schrödinger equation. Comparing Fig. 3.19 to the swallowtails illustrated in Fig. 3.17, we make the following conjecture: non-trivial period-doubled solutions for a lattice of period d appear as the saddle of the swallowtail for Bloch waves for a lattice of period $2d$.

This conjecture is supported by tuning Δ from zero to unity. We illustrate this tuning in the subsequent panels of Fig. 3.19. Figure 3.19(b) shows the case $\Delta \ll 1$. Figure 3.19(c) shows the endpoint, $\Delta = 1$. The shape of the lattice in the panels (a)-(c) is sketched in Fig. 3.18. In Fig. 3.19(b), the trivial and non-trivial period-doubled solutions of Fig. 3.19(a) separate into two bands. The lower band (solid curve) consists of the lower part of the trivial period-doubled solutions, with the non-trivial period-doubled solutions forming the upper edge of the swallowtail. The upper band (dashed curve) consists of the upper part of the trivial period-doubled solutions. One observes that there is a small gap between the two bands. Moreover, unlike in the case of the one-color lattice, one obtains a swallowtail even for weak nonlinearity. As Δ is increased, this gap increases. Figure 3.19(c) shows the case $\Delta = 1$. The system is now again in a weakly nonlinear regime with a one-color lattice. Thus the swallowtail disappears.

One observes that, in general, the first two Bloch-wave bands of a one-color lattice of period $2d$ (panel (c)) can be derived from the trivial period-doubled solutions of a lattice of period d (panel (a)) via a two-color intermediate lattice (panel (b)). This follows from the fact that the second Bloch-wave band has two density peaks per site.

In the strongly nonlinear regime, the swallowtail forms in a similar manner but

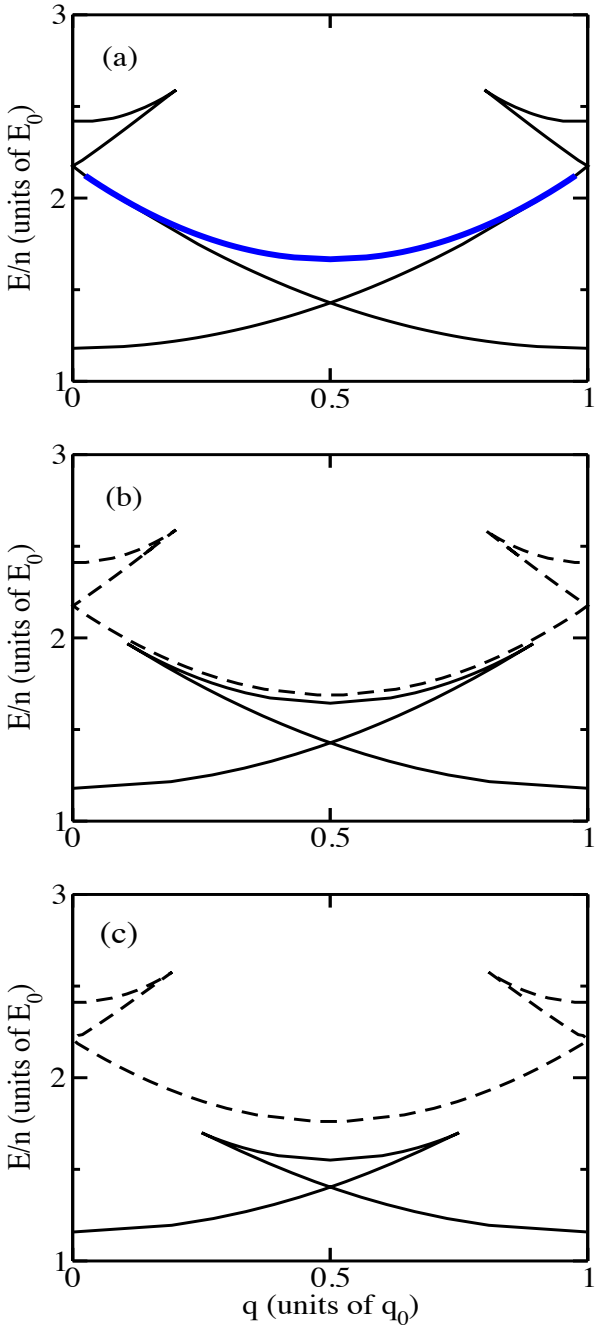

Figure 3.20: Same as Fig. 3.19 but for strong nonlinearity, $gn = 10V_0$. In (b), (c) note that the upper edge of the central swallowtail in the lower band is derived from the non-trivial period-doubled solution of panel (a) (blue thick curve). The lattices associated with (a)-(c) are sketched in Fig. 3.18.

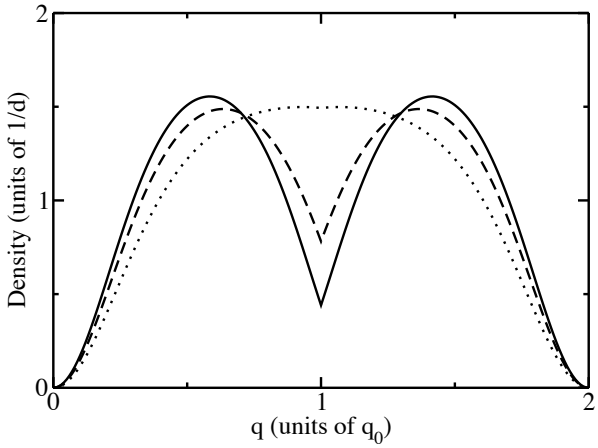

Figure 3.21: The condensate density profiles are illustrated for three cases: $\Delta = 0$, non-trivial period-doubled solutions (solid curve); $\Delta = 1/2$, upper edge of the swallowtail (dashed curve); and $\Delta = 1$, the lowest band (dotted curve). The parameters are $q = 0.5$ and $gn = V_0$, which is the regime of weak nonlinearity, as in Fig. 3.19.

does not disappear for $\Delta = 1$. We illustrate this sequence in Fig. 3.20, again for $\Delta = 0$, $\Delta \ll 1$, and $\Delta = 1$. One clearly sees that the upper edge of the swallowtail in the one-color lattice of period $2d$ is derived from the non-trivial period-doubled solutions of the one-color lattice of period d. The lower edge of the swallowtail is derived from the trivial period-doubled solutions.

This introduces a novel perspective on the origin of the swallowtails in the non-linear band structure. In the figures we illustrated the case of a repulsive condensate, as that is the most common experimentally. The same argument holds for attractive condensates, where the swallowtails form below, rather than above the bands. In particular, in our study of the one-color Kronig-Penney potential [153], we found it intriguing that no swallowtail formed on the lowest band for the attractive case.

Previous interpretations of swallowtails were based on the superfluid screening properties of the condensate [117]. In this argument, the condensate sees the quadratic free particle dispersion up to the sound speed. When written in the form of the Bloch ansatz, these quadratic curves repeat in each Brillouin zone. When the sound speed is such that the maximum quasi-momentum of each curve overlaps with the curve from

the adjoining Brillouin zone, one obtains swallowtails. This does not apply to attractive condensates, since the swallowtails form on the lower edge of the bands and not at all on the lowest band.

In contrast, our argument based on period-doubling applies to both repulsive and attractive condensates. For attractive nonlinearity, the non-trivial period-doubled states form a convex saddle on the lower edge of the 'x' of Fig. 3.19(a), rather than the upper edge. As Δ is tuned from zero to unity, the upper part of the 'x' separates from the lower part, carrying the swallowtail with it. Thus no swallowtail can form on the lowest band.

Thus, we understand swallowtails to be adiabatically connected to period-doubled solutions of a lattice of half the period. They originate in non-trivial period-doubling brought about by the nonlinear term in the NLS.

Finally, since the density is a key observable in experiments on BEC's, in Fig. 3.21 density profiles are illustrated for weak nonlinearity and $\Delta = 0,\ 1/2,\ 1$. The plot is made for the quasi-momentum $q = 0.5$ solution that lies at the center of the non-trivial period-doubled solution (thick blue curve) in Fig. 3.19(a), at the top of the central swallowtails on the lowest band in Fig. 3.19(b), and on the lower band in Fig. 3.19(c).

3.14 Stability Properties and Comparison with Experiments

Several important experiments have been performed with superfluid BEC's in optical lattices. In particular, an experiment by Fallani *et al.* [49, 42] studied the loss rate of the BEC as the quasi-momentum was varied. This loss rate is expected to be monotonically related to the instability time of the condensate. This observable can be modelled theoretically by adding white noise to an initial stationary state on the lattice in simulations. In this way, we investigate the nonlinear stability properties of Bloch-wave solutions to the two-color lattice. Note that unstable solutions which have lifetimes longer than experimental timescales will appear experimentally stable.

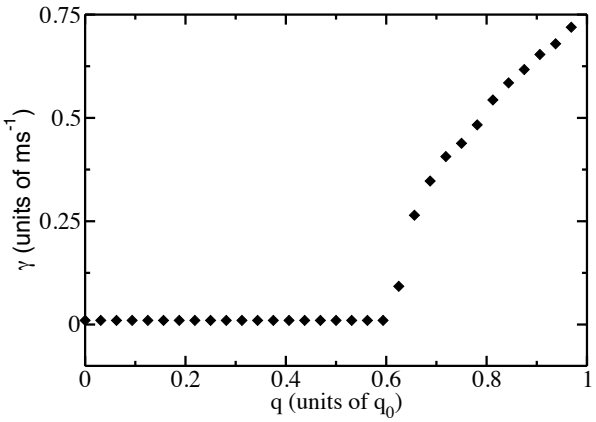

Figure 3.22: Shown is the inverse of the instability time $\gamma = T_i^{-1}$ of stationary states in the lowest band, as a function of the quasi-momentum. White noise was added to the initial state and the wave function was evolved numerically for the NLS with a one-color lattice and weak nonlinearity, $gn = V_0$.

In our simulations, Eq. (3.1) was dynamically evolved using a variable step fourth-order Runge-Kutta algorithm in time and a pseudospectral method in space. We chose periodic boundary conditions in one dimension, with a sufficient number of sites so that the results were independent of the ring circumference. Two schemes for delta functions on a grid were considered: point defects, and narrow square potentials covering several grid points. For square potentials less than one tenth the lattice period d, differences between the two schemes were negligible. Simulations were performed over time scales on the order of those relevant to the experiments, namely, hundreds of milliseconds. The lattice spacing d is taken to be 1 μm and the atomic mass to be that of ^{87}Rb.

The stability of the system is quantified by the variance in the Fourier spectrum,

$$\sigma(t) \equiv \frac{\sum (f(p,t) - f(p,0))^2}{2\sum (f(p,0))^2}\,, \tag{3.94}$$

where $f(p,t)$ is the Fourier component of the wave function at momentum p and time t. The variance approaches unity when the wave function has no component in common with the initial state and zero when then the wave function it is identical to the initial state. We define the instability time T_i to occur when the variance has increased to $\sigma = 0.5$.

A clear experimental observable is the rate of loss of atoms from the system, since the density of the sample can be imaged at successive times. This loss rate is expected to be monotonically related to the inverse time in which instabilities arise. Therefore, we present two relevant studies of the instability times of the condensate. First, the growth rate of the instability,

$$\gamma \equiv 1/T_i \,, \tag{3.95}$$

is determined for a one-color lattice and weak nonlinearity. This relates directly to the experiment of Fallani *et al.*. Second, the lowest positive quasi-momentum for which the system becomes unstable is evaluated as a function of Δ for the two-color lattice.

Figure 3.22 presents the results of the first study. The solutions are stable until the quasi-momentum where the nontrivial and trivial period-doubled solutions connect in the band structure (see Fig. 3.19(a), as well as Ref. [106]). Stability can also be determined from the effective mass of the system,

$$m^* \equiv \frac{1}{\partial^2 E/\partial^2 q} \,. \tag{3.96}$$

If the effective mass becomes negative, the NLS becomes effectively attractive. Since the ground state of an attractive condensate is localized, solutions with negative effective mass $m^* < 0$ are unstable. The point where the nontrivial and trivial period-doubled solutions connect corresponds to a change in the sign of the effective mass from positive to negative. Our figure qualitatively replicates the results found by Fallani *et al.* [50].

Figure 3.23 presents the second study. In particular, the smallest quasi-momentum for which the periodic system first becomes unstable in a time less than 100 ms is plotted. The two end points at $\Delta = 0$ and $\Delta = 1$ are easily determined, since those systems are one-color lattices. As per our discussion in the previous paragraph, the Bloch wave solutions become unstable at the point where the non-trivial period-doubled solutions connect to the Bloch-wave band. The two one-color lattice systems have the same ratio of nonlinearity to potential strength, since for $\Delta = 0$ the potential strength is V_0 and

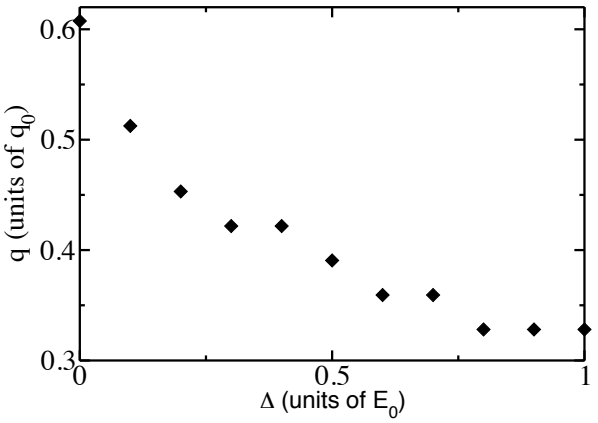

Figure 3.23: The lowest positive quasi-momentum for which the system becomes unstable. The parameter Δ is varied, tuning from a lattice with period d to one of period $2d$. The results of simulations of the NLS with weak nonlinearity, $gn = V_0$, are shown.

the number of atoms is n, while for $\Delta = 1$ they are $2V_0$ and $2n$. Thus the existence of the non-trivial period-doubled states scales with the length of the Brillouin zone. The absolute quasi-momentum where instability occurs then differs by a factor of two, since for a lattice of period $2d$ the Brillouin zone is half the length as for d. In Fig. 3.23, this is $q \sim 0.6$ for $\Delta = 0$ and $q \sim 0.3$ for $\Delta = 1$. In the case of the linear Schrödinger equation, the endpoints would be 0.5 and 0.25, respectively. Note that our simulations are accurate to within a few percent.

The intermediate points in Fig. 3.23, where $0 < \Delta < 1$ and one obtains a two-color lattice, can be understood by again considering where the effective mass becomes negative. As the energy band from the $\Delta = 0$ lattice separates into the first two bands of the $\Delta = 1$ lattice, the upper edge of the swallowtail shrinks. Recall that states on the lower edge of swallowtails are stable [153]. As Δ is increased, the swallowtail disappears, since the nonlinearity is weak. The quasi-momentum at which the band changes from concave up to concave down, i.e. where the effective mass changes sign, moves from right to left, as can be seen in the descending data points of Fig. 3.23. A similar argument holds for the case of strong nonlinearity.

3.15 Two-Color Lattice Conclusion

We have presented a novel way of understanding the appearance of swallowtails in nonlinear band structure. Swallowtails in a lattice of period $2d$ are adiabatically connected to the non-trivial period-doubled solutions of a lattice of period d. Non-trivial period-doubled solutions are caused by the nonlinearity in the mean field of the condensate [106]. They do not appear as solutions to the linear Schrödinger equation and therefore have no analog in linear band theory. Our way of understanding swallowtails is valid for both repulsive and attractive condensates, unlike previous explanations [117].

We used the two-color lattice to adiabatically connect the one-color lattice of period d and $2d$. We showed that swallowtails appear in the band structure of the two-color lattice even for weak nonlinearity, unlike in the one-color case. We then made explicit predictions for the onset of instability in the band structure for the one- and two-color lattices based on numerical simulations. Instability is experimentally observable as an increased loss rate due to heating of the condensate [50], and weak nonlinearity is the present regime of experimental investigation.

Our studies utilized a two-color Kronig-Penney potential. In order to justify the use of this model we compared analytic solutions to the one-color Kronig-Penney [153], Jacobi elliptic [23], and sinusoidal potentials [107]. We showed that each of these models resulted in a similar band structure. Moreover, by putting the exact solutions to the Jacobi elliptic potential in Bloch wave form, we were able to resolve a longstanding question concerning density offsets and stability in the work of Bronski *et al* [23, 24].

We note that there are other solution types than the ones we have considered. For instance, there are gap solitons [105, 104, 109] and time-periodic solutions [129, 128]. These can have novel features in the two-color lattice [104]. We emphasize that we have treated only the superfluid phase of cold bosons on a lattice [52, 64].

Nonlinearity often introduces solution types which do not appear in linear equa-

tions [84]. For instance, the plane wave solutions to the particle-on-a-ring problem, which are well known from linear quantum mechanics, have $2j$ nodes, where j is a positive definite integer. When attractive nonlinearity is added to this problem, so that one has the attractive NLS, the constant density, or $j = 0$ solution undergoes a bifurcation for a critical value of the nonlinearity. The ground state spontaneously develops a peak somewhere on the ring, while the constant density solution remains a stationary but excited state [27]. The NLS with a periodic potential has a similar feature. For a critical value of the nonlinearity, the bands form a cusp which then bifurcates into an upper and lower portion of the band, i.e., the swallowtail. The non-trivial period-doubled solutions are caused by this property.

In our previous work [153], we gave an instance of the same effect for the attractive NLS with a single repulsive impurity, i.e., a delta function with positive coefficient. There, for zero or weak nonlinearity there is no bound state and the solution is a pair of solitons propagating away from the impurity. At a critical value of the nonlinearity, this bifurcates into a travelling wave solution and a bound state. The latter occurs due to the dominance of the attractive nonlinearity over both the kinetic energy term and the repulsive effect of the impurity. This is the idea underlying the non-trivial period-doubled solutions on the lattice, which, in our Kronig-Penney formulation, have an "impurity" located in the center of each density peak.

Interestingly, the symmetry breaking in the above mentioned case of the nonlinear analog of the particle-on-a-ring problem occurs at exactly the same point even in the many body quantum field theory [88]. In this sense, it would be intriguing to determine in the many body quantum theory of weakly interacting bosons with an external periodic potential (a) whether swallowtails occur, and (b) if they do so at the same critical value of the nonlinearity as predicted by the mean field approximation.

Chapter 4

Atomtronics

A collection of ultracold atoms subject to a spatially periodic potential can exhibit behavior analogous to electrons in a lattice. This fact has been established in an impressive series of experiments with Bose-Einstein condensates and Fermi gases in optical lattices [5, 31, 62, 116, 41, 114, 135, 126, 54, 97]. The analogy between ultracold atoms in lattice potentials and electrons in crystals is manifestly a rich one. It extends to strongly interacting ultracold Bose gases which exhibit both superfluid and insulating behavior, and feature a gapped many-body energy spectrum. The tunability of interactions in optical lattices has led to the spectacular demonstration of these properties [64, 163].

Other interesting condensed matter systems that can be modeled in atomic gas experiments are electronic devices. Ruschhaupt and Muga [140] have described an atom device with diode-like behavior, and Micheli et. al. [111] have proposed a single-atom transistor that serves as a switch (see also [139, 141, 142, 37, 112]). Both of these devices depend on control and coherence at the single atom level. Moreover, Stickney et. al. [162] have recently demonstrated that a Bose-Einstein condensate in a triple well potential can exhibit behavior similar to that of a field effect transistor.

Our intent is to establish ultracold atom analogs of electronic materials and semiconductor devices that can be used to leverage the vast body of electronic knowledge and heuristic methods. From semiconductor materials and fundamental devices, the

analogy expands into what can be referred to as *atomtronics*. With diodes and transistors in hand, it is straightforward to conceive of atom amplifiers, oscillators, flip-flops, logic gates, and a host of other atomtronic circuit analogs to electronic circuits. Such a set of devices can serve as a toolbox for implementing and managing integrated circuits containing atom optical elements [137, 15, 157] or quantum computation components [20, 21, 161] and might be of particular interest in the context of rapidly advancing atom chip technologies [53, 132].

In this chapter, we introduce analogs of electronic materials, including metals, insulators, and semiconductors, in the context of ultracold strongly interacting bosons [156]. We use lattice defects to achieve behavior similar to doped P-type and N-type semiconductors. The interest is to adjoin P-type and N-type lattices to create diodes and then NPN or PNP structures to achieve behavior similar to that of bipolar junction transistors. We show that such heterogeneous structures can indeed be made to mimic their electronic counterparts.

Atoms in periodic structures and electrons in solid state crystals have much in common. In both systems, particle motion occurs by tunneling through the potential barrier separating two lattice sites. A particle, an electron or an atom, can delocalize over the entire lattice and sustain currents. In both systems, currents are created when there is a potential gradient which causes the particles to move from a region of higher potential to a region of lower potential. In electronics, potentials arise from electric fields. In atomtronics, potential gradients can be understood in terms of chemical potential gradients. The characteristics of both electronic and atomtronic devices are examined by using a battery to apply a potential difference across the system and observing the response in the current.

Different types of electronic conductors exist because electrons in a crystal structure occupy states of an energy spectrum that feature a band structure. The materials can carry a current, i.e. are conducting, only if the highest occupied energy band is

only partially filled with electrons. On the other hand, the system is an insulator if all occupied bands are full. These properties of electronic materials can be directly reproduced with weakly interacting fermionic atoms in periodic potentials.

Using fermionic atoms is not the only way in which analogs of electronic materials can be created. In this chapter, we focus on ultracold strongly interacting bosonic atoms in periodic structures. These systems can also be made to behave similarly to their electronic counterparts. Strong repulsive interactions prevent atoms from occupying the same lattice site, mimicking the fermionic behavior of electrons. Hence, a current can flow easily as long as there are empty sites available. However, once the filling reaches one atom per site, the system becomes an insulator. A large energy gap given by the repulsive onsite interaction must be overcome in order to add another particle to this configuration. Particles added in excess of a filling of one atom per site can again carry a current since they can move around freely above the filled layer of one atom per site. The system remains a conductor until it arrives at a filling of two atoms per site and becomes an insulator again. This is the same mechanism that drives the Mott-insulator superfluid transition.

These properties show that a strongly interacting Bose gas features a close analog of the band structure of electronic materials. The filling of the bands determines whether a material is a conductor or an insulator. There is, however, an important difference between atomtronic and electronic systems with respect to the band structure. The band structure of strongly interacting bosons does not describe states that can be occupied by a single particle independently of the configuration of others, but represents the energies of many-body states. While the energy gap is due to the Pauli exclusion principle combined with the single-particle band structure in the case of electrons, the gap arises from the onsite repulsive interaction between atoms in the bosonic case. In this chapter, we will speak of *many-body* energy bands in the case of bosonic systems to take account of this important difference. The many-body band structure of strongly

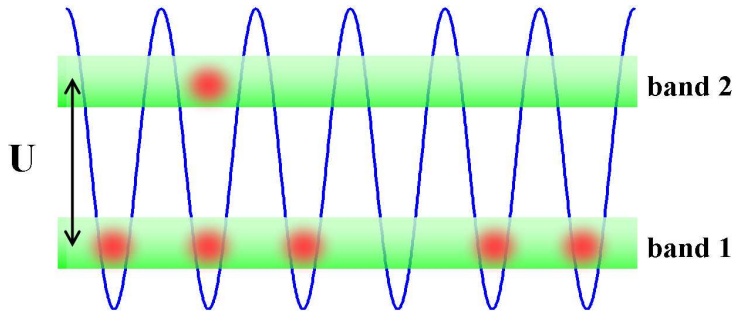

Figure 4.1: Schematic of the atomtronic many-body energy band structure of strongly interacting bosons in a lattice. The first band consists of all states with a filling of less than one atom per site while the second band contains all states with filling between one and two atoms per site. The two bands are separated by the onsite repulsive interaction U.

interacting bosons in a lattice is depicted schematically in Fig. 4.1. The lowest band is made up of states with between zero and one atom per site. The next band contains all states with one to two atoms per site. Higher bands are formed analogously. The highest occupied band of a conductor is only partially filled while insulators are characterized by full bands.

Apart from the many-body character of the band structure, a second important feature of the atomtronic system is that the atomtronic conductor exhibits superfluid rather than normal flow and in that aspect resembles an electronic superconductor.

In this chapter, the behavior of atomtronic materials in simple circuits is presented and we show how to use these materials to build more complex circuit devices, specifically diodes and bipolar junction transistors. The chapter is structured as follows. Section 4.1 introduces the Bose-Hubbard formalism that will be used to describe the atomtronic systems. In particular, it discusses the zero temperature phase diagram and the properties of an atomtronic battery. Doped atomtronic materials and the current-voltage behavior of atomtronic wires will be discussed in Sec. 4.3. A diode obtained by combining a P-type and an N-type atomtronic material with a voltage bias applied by a battery is examined in Sec. 4.4. Section 4.5 presents the atomic analog

of a semiconductor bipolar junction transistor. Finally, Sec. 4.6 contains remarks on possible applications, on the differences between atomtronic devices and their electronic counterparts and on future perspectives. Appendix C contains details of the calculation methods that were used throughout the chapter.

4.1 Quantum Phase Transition in the Bose-Hubbard Formalism

The zero temperature quantum phases of bosons in a lattice are key to understanding the different kinds of atomtronic materials. A system of repulsive bosons in a one-dimensional chain of lattice sites can be modeled with the Bose-Hubbard Hamiltonian

$$\hat{H} = \frac{U}{2}\sum_i \hat{n}_i(\hat{n}_i - 1) - J\sum_{\langle ij\rangle} \hat{a}_i^\dagger \hat{a}_j + \sum_i (\epsilon_i - \mu)\hat{n}_i \,, \tag{4.1}$$

where $\hat{a}_i$ is the annihilation operator for a particle at site i, $\hat{n}_i \equiv \hat{a}_i^\dagger \hat{a}_i$ is the number operator at site i, U is the onsite repulsive interaction strength, J is the hopping matrix element between nearest neighbors, $\langle ij\rangle$ labels nearest neighbors, ϵ_i is the external potential at site i and μ is the chemical potential of the system. The Bose-Hubbard Hamiltonian is obtained by retaining only the contributions of the lowest single particle Bloch band to the Hilbert space and by making a tight binding approximation (for a review see Ref. [179]). This yields an accurate description of an ultracold dilute Bose gas in a periodic potential at low energies. The zero temperature phase diagram of this Hamiltonian was first studied by Fisher, *et. al.*, [52].

For very large onsite repulsion, $U \gg J$, the system enters the regime of *fermionization* where bosons are impenetrable and only two Fock states, $|n_i\rangle$ and $|n_i + 1\rangle$, are needed at each site to accurately describe the system (two-state approximation). Note that this is equivalent to mapping bosonic operators onto fermionic ones via the Jordan-Wigner transformation [86, 143]. The data presented in this chapter is obtained by considering the system described by the Hamiltonian, Eq. (4.1), in the fermionized

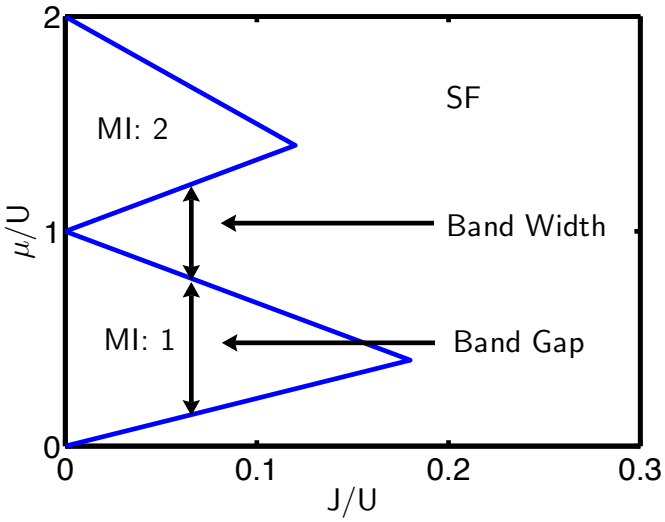

Figure 4.2: Zero-temperature phase diagram of a Bose gas obtained from Eq. (4.2) for an infinite one-dimensional lattice using the two-state approximation (fermionized regime, $U \gg J$). At large values of J/U the gas is superfluid (SF). Below a critical value of J/U the system enters a Mott-insulator phase (MI) for integer filling, while it remains superfluid for non-integer filling. The $MI:1$ Mott-insulator region has one atom per site and the $MI:2$ region has two atoms per site. The width of a Mott lobe at a given J/U gives the size of the band gap in the many-body band structure while the width of a band is given by the width of the superfluid region. The Mott lobe boundaries are linear due to the use of the two-state approximation.

regime. We have verified that the error resulting from the two-state approximation becomes negligible for $U \geq 100J$ (see also [12]).

The phase diagram of the Bose-Hubbard Hamiltonian contains information about the many-body band structure of the system. At zero temperature, the Bose-Hubbard model has two distinct phases, a Mott-insulating phase and a superfluid phase. Figure 4.2 presents the boundary between the conducting and insulating phases as a function of the hopping parameter J/U and the chemical potential μ/U. The Mott-insulating phase is entered below a critical value of J/U for an integer number of particles per site. In this phase, strong interactions completely block particle motion rendering the gas incompressible, that is $\partial n/\partial\mu = 0$, where n is the average filling of a site. The two lobes shown limit the Mott-insulator zones with one atom per site (lower lobe, MI:1) and two

atoms per site (upper lobe, MI:2). The remainder of the depicted part of the phase diagram is in the conducting superfluid phase, labeled SF. The superfluid phase is obtained for non-integer filling. No insulating phase exists for values of J/U larger than ~ 1. Note that the triangular, non-rounded, shape of the Mott lobes in Fig. 4.2 is due to the two-state approximation becoming increasingly inaccurate as J/U is increased.

Each value of μ/U and J/U maps onto a particular lattice filling, n. Figure 4.2 is obtained from the relation between these parameters in the superfluid phase for an infinite number of lattices sites and strong interactions ($J \ll U$) [123],

$$\mu = U(m-1) + (-1)^m 2mJ\cos(\pi n)\,, \tag{4.2}$$

where $m = 1, 2, \ldots$ is the band index and the filling n satisfies $(m-1) \leq n \leq m$. The superfluid-insulator phase boundaries presented in Fig. 4.2 are obtained by setting n to an integer and $m = n$ for the lower boundary and $m = n+1$ for the upper boundary. The expression Eq. (4.2) is derived using a Jordan-Wigner transformation approach within the two-state approximation. A more accurate model of the phase boundary can be calculated using a mean field model [98] to find that

$$\frac{\mu}{U} = \frac{J}{U}\left((2m-1/2) - J/U \pm \sqrt{(J/U)^2 - J/U(2m+1) + 1/4}\right)\,. \tag{4.3}$$

This is of a parabolic form and rounds the tips of the lobes.

Plotting the phase diagram as a function of μ/U rather than the number of particles is useful because in this way the gaps between many-body bands become visible. The size of the gaps are given by the widths of the insulating zones, whereas the sizes of the bands are given by the widths of the superfluid zones. Note that the size of the gaps depend on the value of J/U. In order to have access to both insulating and conducting phases, the ratio J/U must be small. If this ratio is too large there is no well defined gap and therefore no transition to an insulating phase for integer filling. The basic ideas presented in this chapter rely on this condition being satisfied.

They do not require the stronger condition $U \gg J$ for fermionization. The condition of fermionization is assumed merely to facilitate calculations.

Most atomic systems do not have a constant density throughout the system due to the ways in which the atoms are trapped. For instance, a harmonic trapping potential will cause more atoms to be in the center then at the edges. In this case, a local chemical potential, $\mu_i = \mu - V_i$, becomes important when determining the effects of the lattice. This can lead to insulating regions and superfluid regions all in the same system, traditionally in shell structures [64].

4.2 Atomtronic Battery

Just as for electronic circuits, the atomtronic version of a battery is crucial but it is also subtle. In this section, we identify the basic properties and actions of the atom analog of a battery.

Energy for electronic circuits is supplied by sources of electric potential. Furthermore, electric potentials are used to set the bias points of circuit elements to achieve their desired behavior. For simplicity, we will use the term battery to refer to a device that provides a fixed potential difference and can supply an electric current or atomic flux.

In the electronic case, one is interested in the electric potential difference, or the voltage, between two points. A specific potential difference between two points within a device or circuit is achieved by connecting those two points to the terminals of a battery. In an atomtronic circuit, the function of the battery is to hold the two contacts at different values of the chemical potential, say μ_L on the left and μ_R on the right. The applied voltage is then defined by

$$V \equiv \mu_L - \mu_R \,. \tag{4.4}$$

The current flows from higher to lower chemical potential. Chemical potential difference

in atomtronic system is analogous to electric potential difference in electronic systems. Note that the equilibrium value of the chemical potential is important since it sets the average filling of the lattice.

To understand the physics underlying this concept, note that bringing the system with chemical potential μ in contact with a battery pole of chemical potential $\mu_L > \mu$ leads to the injection of Δn particles. The magnitude of Δn is given by the difference in filling of states with chemical potentials μ and μ_L and can be determined from the phase diagram. The particle transfer increases with increasing μ_L within a superfluid region and becomes constant as μ_L is moved into a Mott insulating zone where the system is incompressible. In the fermionization regime, the magnitude of Δn is fixed by Eq. (4.2). Analogous reasoning applies to the removal of particles at the battery pole with $\mu_R < \mu$. While μ_R remains in superfluid region of the phase diagram, changes in the chemical potential will lead to changes in the atom transfer numbers. However, once μ_R enters the Mott insulator region of the phase diagram, small changes do not create changes in particle number transfer.

Feeding atoms into a circuit element through a contact at one end and removing them through a contact at the other end generates a current. After time-averaging, this current reaches a constant value if the carrier excess at one end is replenished through one contact with the battery at the same rate at which the deficit is maintained at the other end through the contact with the other pole of the battery. In addition to this time averaged current, there is also the presence of the shot noise associated with the time distributions of individual atoms entering or leaving the battery terminals.

Experimentally, a battery can be created by establishing two separate large systems which act as reservoirs, each with its own constant chemical potential. These may also be lattices or other experimentally plausible systems, such as large harmonic traps, containing a large number of atoms. Changing the frequency of the harmonic traps, or adjusting the lattice height, can be used to tune the chemical potentials of these reser-

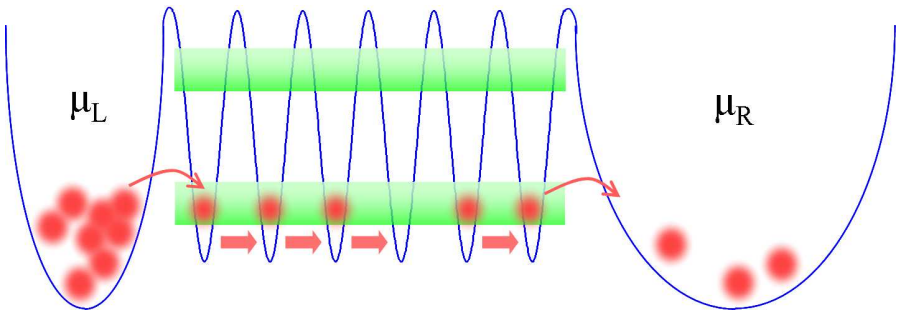

Figure 4.3: Schematic of atoms in a lattice connected to an atomtronic battery. A voltage is applied by connecting the system to two reservoirs, one of higher (left) and one of lower (right) chemical potential. An excess (deficit) of atoms is generated in the left (right) part of the system, giving rise to a current from left to right.

voirs. Each of these reservoirs can be connected to one end of the atomtronic system and current is then possible from the higher chemical potential system to the lower one. This configuration is displayed in Fig. 4.3. From a practical point of view, the chemical potentials of the battery poles can be maintained by transferring atoms, possibly classically, between the two poles. In addition to the structure and chemical potential of the reservoirs, the temperature of the reservoirs can play a role in the transfer of atoms between the wire and the battery terminals. Since a high temperature reservoir can wash out the effects of the quantum phase transition in the lattice, a low temperature reservoir is required. The temperature of the reservoir should be small enough so that excitations on the order of U are highly unlikely.

4.3 Atomtronic Conductors

An attractive feature of atomtronic materials is that their conductivity properties can be easily modified. The primary conductor for an atomtronic system is an optical lattice with no other external potentials. This corresponds to a wire in an electronic system. The properties of the wire are derived from the atomic filling and associated chemical potential. For chemical potentials in the superfluid region of the phase diagram, the wire conducts well. However, when the chemical potential is in the Mott zones, the

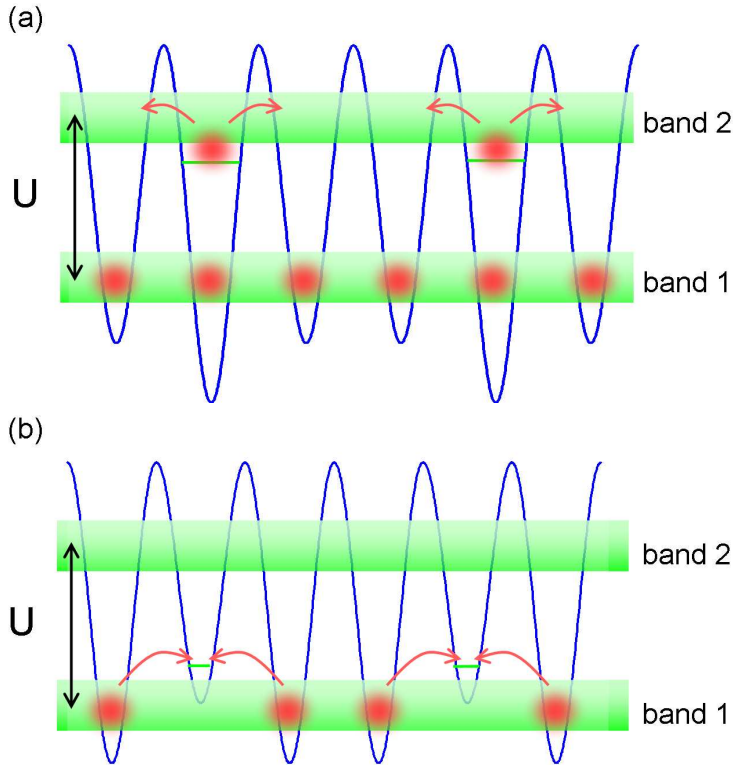

Figure 4.4: (a) Schematics of an N-doped lattice. The donor sites feature a level right below the first empty many-body band. An atom which occupies this level can easily be excited and move throughout the lattice. (b) Schematics of a P-doped lattice. Acceptor sites have a level right above the highest full band. Atoms can easily be excited into this level and allow for a hole to move throughout the lattice.

wire becomes an insulator. In this section, we first discuss the possibility of varying the conductivity of a wire by lattice doping as is done in semiconductor systems. The idea is that what is originally an insulator can be coaxed into behaving like a conductor just as in the electronic case. Secondly, we focus on the current-voltage characteristics of the different types of atomtronic materials.

4.3.1 Doped Materials

New materials with interesting properties can be designed by modifying the lattice in which the atoms are confined, and hence the many-body band structure. This can be done in various ways. In the case of an optical lattice, the periodicity of the lattice

can be modified by superimposing a periodic potential of different wavelength [124]. Disorder can be introduced by randomly modifying individual sites [78, 56, 149]. A further handle on the properties of the material is the symmetry of a two-dimensional or three-dimensional lattice [67, 147, 146]. Finally, it is conceivable to introduce a second atomic species, either bosonic or fermionic, and to modify the properties of the material via inter-species interactions.

The atom analog of the doping of a semiconductor is particularly interesting. The aim of doping is to create energy levels in the energy gap between two bands. N-type doping is associated with energy levels located close to the lower edge of the first empty band while P-type doping gives rise to levels close to the upper edge of the highest full band. Both are accomplished by modifying the potential at individual lattice sites. N-type doping is achieved by replacing some lattice sites with donor sites. These correspond to potential wells which are slightly deeper than those of the unmodified lattice. Analogously, P-type doping requires introducing acceptor sites of slightly shallower potential. The two potential configurations are shown in Fig. 4.4.

The advantage of doping is that it can turn an insulator into a conductor without having to excite particles across the band gap into the empty conduction band. In atomtronics, this means that doping shifts the insulator zone boundary in the phase diagram. Figure 4.5 compares the phase diagram of the undoped lattice with that of a N-doped and a P-doped lattice. N-type doping shifts the insulating zone downwards such that states that were previously in the insulating zone come to lie right above the insulating zone where the lattice has a full valence band and a few free carriers in the conduction band. Similarly, P-type doping shifts the insulating zone upwards such that states previously in the insulating region come to lie right below the insulating zone where the lattice has an almost full valence band with a few free hole carriers. In Fig. 4.5 the new insulating zones were derived for an infinite lattice where every third site was doped by $\Delta\epsilon = \pm 5J$ using a modified Jordan-Wigner transformation [123].

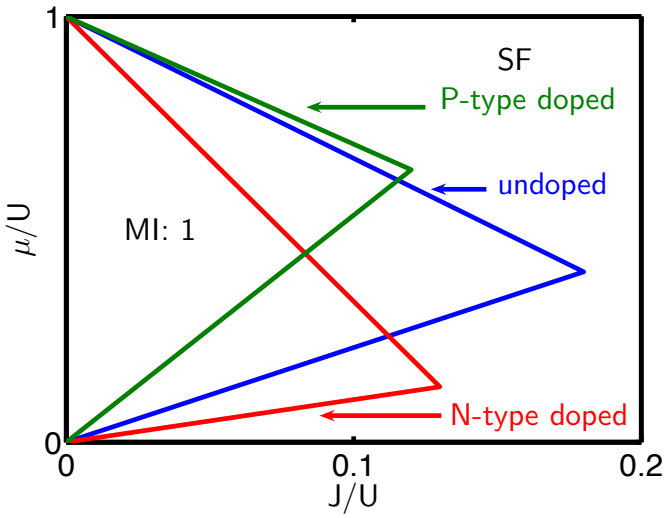

Figure 4.5: Zero-temperature phase diagram of a Bose gas in an undoped (blue), an N-doped (red) and a P-doped (green) lattice. The boundary of the lowest Mott insulator lobe with a filling of one atom per site is displayed as calculated using the two-state approximation. The results for the doped lattices were obtained by adding an energy of $\pm 5J$ to every third site in an infinite lattice using a modified Jordan-Wigner transformation. N-type doping turns an insulating state into a superfluid state with more than one atom per site. Similarly, P-type doping turns an insulating state into a superfluid state with less than one atom per site.

4.3.2 Material Current Properties

This section discusses the current response of atomtronic wires to an applied voltage. The magnitude of the current depends on the properties of the material and on the nature of the contact with the battery. The material can be in the Mott insulating phase or in the superfluid phase. In the Mott phase, a small voltage does not yield a current. Only at a large voltage, of the order of the gap U, is the battery able to generate a current by feeding particles into the next unoccupied band. If the material is in the superfluid phase, a small voltage is enough to generate a current. Due to the superfluid nature of the atomic carriers, this current is not slowed by friction. Hence, the ratio of voltage to current does not have the physical meaning usually associated with resistance, but reflects the limits on the current at a given voltage due to factors other

than dissipation. A primary limit is set by the hopping parameter J which quantifies how fast atoms can move from one site to the next. The value of the hopping parameter depends on the shape and the depth of the lattice. A further limit on the current is due to the interaction between atoms. Repulsion forces them to move in a highly correlated fashion. For this reason, the current does not grow linearly with the number of carriers at fixed voltage. Instead, the current per particle drops as more carriers are added and eventually goes to zero when the filling is one atom per site and the system becomes an insulator.

Apart from material dependent factors, the nature of the contact with the battery can set the maximum achievable current. If it is more difficult for atoms to pass through the contact than to hop from one lattice site to the next then the current is not limited by J but by the rate at which the battery can feed in and remove particles. This situation is encountered when operating a battery in a regime of very weak coupling. The same properties are present in electronic systems where there can be different types of contacts, such as rectifying and ohmic contacts [8]. In this chapter we focus on the regime of maximum currents where currents are limited by the hopping parameter J and are not influenced by the properties of the battery contact.

Our calculation of the current response is performed in several steps. First, the chemical potentials of the left and right batteries are chosen. These chemical potentials correspond to an average site filling. For a wire or a diode, a two well system is analyzed corresponding to a junction in the system. An initial state of N_L atoms on the left and N_R atoms on the right, as determined by the chemical potentials and Eq. (4.2), is set with a phase corresponding to the lowest energy state with this density configuration. The state is propagated in time. The calculated current is determined by the time average current during half of an oscillation. This calculation is motivated by properties of traveling waves in which many of these oscillations occur in sequence. See the Appendix for a further discussion of the calculation of currents.

Figure 4.6 presents the current as a function of voltage for lattices, or wires, of average filling $n = 1.1, 1.3, 1.5, 1.7, 1.9$. The calculation performed to obtain these current-voltage characteristic curves are described in the Appendix. At fixed filling, the current increases monotonically with increasing voltage. The maximum current attainable for a half-filled second band is $\sim 1.4\, J/\hbar$. The voltage in Fig. 4.6 is given in units of $\Delta\mu_{\max}$. This quantity denotes the chemical potential differences that yield the maximum currents. It corresponds to the chemical potential difference at which the system, for a given filling, enters an insulating regime at one of the two battery contacts.

The curves for fillings with an equal number of free particles and holes coincide, demonstrating the equivalence of hole and particle motion for $U \gg J$. The inset in Fig. 4.6 presents the currents at different average fillings, corresponding to different materials, at $\Delta\mu = \Delta\mu_{\max}$. The plot is symmetric around its maximum at half filling reflecting particle-hole symmetry. Note that the average current per free particle, i.e. holes at $n > 1/2$, is constant.

4.4 Atomtronic Diode

A diode is a circuit element that features a highly asymmetric current-voltage curve. It allows a large current to pass in one direction, but not in the other. The analog of an electronic diode is an atomtronic circuit element that lets an atomic current pass through when applying a voltage, $V = \mu_L - \mu_R$, while allowing no current or only a small saturation current for a voltage, $V = -(\mu_L - \mu_R)$.

In solid state electronics, diodes are built by setting up a PN-junction in which a P-type semiconductor is brought into contact with an N-type semiconductor. Electrons move through the junction until an equilibrium is reached. This process depletes the junction region of free charges, leaving behind the static charges of the donor and acceptor impurities. As illustrated in Fig. 4.7(a), this creates an effective potential step across the junction. When a reverse bias voltage is applied, the energy barrier is

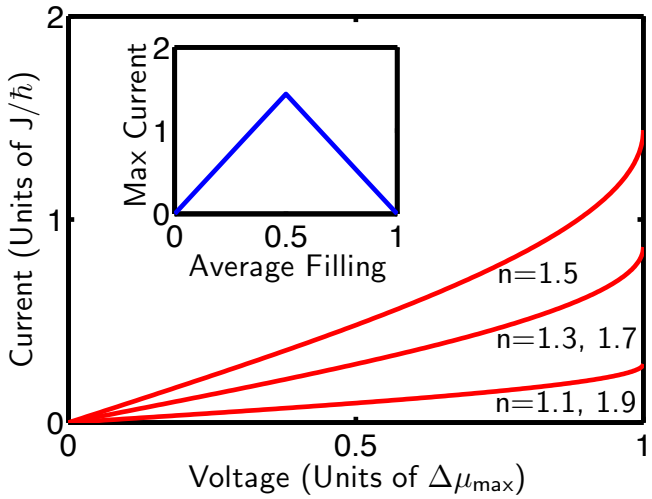

Figure 4.6: Current as a function of chemical potential difference (voltage) for different materials (different fillings n) in the fermionization regime where bosons are impenetrable. A wire with a certain number of atoms carries the same current as a wire with that number of holes (particle-hole symmetry). The chemical potential difference is given in units of $\Delta\mu_{\max}$. This quantity denotes the chemical potential differences that yield the maximum currents and corresponds to the chemical potential difference at which the system enters an insulating regime at one of the two battery contacts for a given n. Inset: Current as a function of filling at $\Delta\mu_{\max}$. Maximum currents are attained at half filling. Note the symmetry in the current due to the particle-hole symmetry.

increased, reducing the flux of electrons from N-type to P-type. At the same time the number of electrons that can fall down the step remains constant giving rise to a reverse bias saturation current that is independent of voltage (see Fig. 4.7 (b)). However, if the diode is forward biased, more electrons are able to move from the N-type to the P-type material than at equilibrium since the potential barrier is decreased by the forward bias voltage (see Fig. 4.7(c)). A detailed discussion of the diode behavior of a semiconductor PN-junction can for example be found in [8].

4.4.1 Diode PN-junction configuration

As discussed previously, we can design atomtronic wires whose conductivity properties can be described by locating the material's chemical potential in its phase diagram.

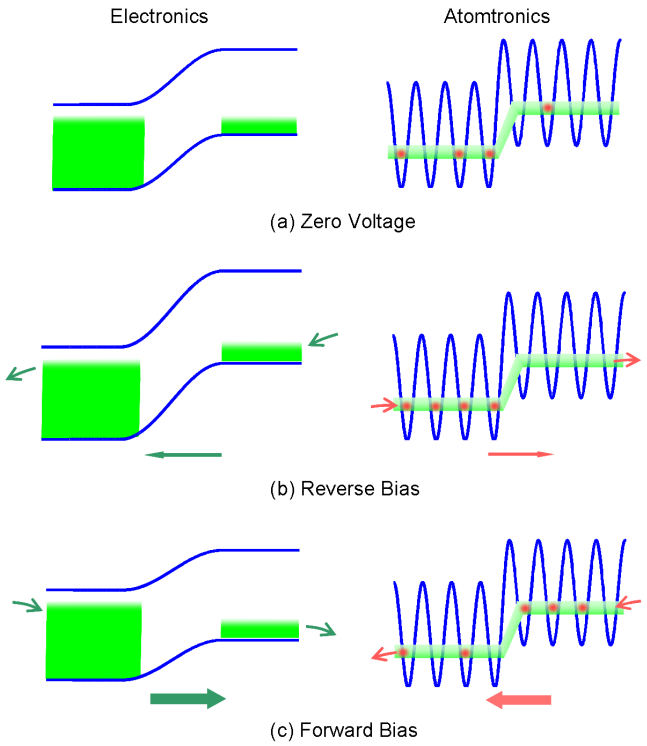

Figure 4.7: Schematic of the conduction band of an electronic (left panels) and atomtronic (right panels) PN-junction diode in (a) equilibrium, (b) reverse bias and (c) forward bias with N-type materials on the left and P-type on the right of each configuration. Left panels: The electronic system features a voltage dependent energy barrier at the junction leading to an increasing (decreasing) flux from the N-type to the P-type material as the junction is forward (reverse) biased while the current from P to N is independent of voltage. Right panels: The operation of an atomtronic diode is based on the existence of insulating phases where $\partial n/\partial \mu = 0$, i.e. a change in voltage does not lead to a change in particle transfer between battery and system. As a consequence, only a small current can flow from N-component to P-component through an atomtronic diode in reverse bias while in forward bias the particle transfer between battery and system can be varied over a large range.

Composite materials, such as PN-junctions, can be produced by connecting lattices of different doping. Another possibility of building a junction is to superimpose additional external potentials, for example a simple potential step. This has the effect of shifting the phase diagram of a part of the lattice upwards or downwards with respect to that of the rest. Since phase boundary effects are small, the state of the different components can be accurately described by the phase diagrams of the individual materials (see Ap-

pendix for details). This means that a local chemical potential can be associated with each component of the conductor that can be located in each material's phase diagram. Thereby, the local conductivity properties can be identified. Of course, at equilibrium, i.e. at zero voltage, the composite material is actually described by a single chemical potential μ but it is μ relative to the zero point energy of each lattice site that determines the filling of each site.

In the following, we focus on a junction created by an external potential step since this may be the easiest experimental realization of a diode. The potential step could be generated experimentally by exposing one part of the system to off-resonant laser light. The main characteristics of the diode behavior are not affected by this choice.

The conduction band of a semiconductor PN-junction features a small thermal electron population on the P-side and a considerably larger electron filling on the N-side. An example of an atomtronic equilibrium configuration with analogous features is represented by the squares in Fig. 4.8. The small (large) population of the second band in the P-type (N-type) material yields the analog of the small (large) thermal electron population of the conduction band in a semiconductor.

4.4.2 Diode current-voltage characteristics

To achieve diode characteristics, we exploit the possibility of undergoing a quantum phase transition between insulating and superfluid phases. The materials are configured such that the chemical potentials of the battery poles remain in the superfluid regime when hooking up the battery in one direction, but they easily enter insulating regimes when the voltage is applied in the opposite direction.

The effect of applying a voltage is illustrated in Fig. 4.8. Forward bias is achieved by connecting the P-side to the low voltage pole and the N-side to the high voltage pole of the battery. In this situation, the chemical potentials of the battery poles are located in the superfluid region of the phase diagram and atoms can flow from the P-component

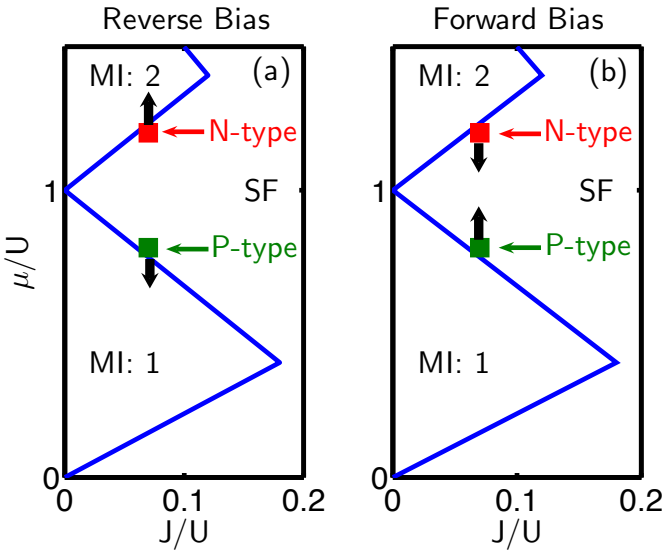

Figure 4.8: Phase diagram of the PN-junction configuration of an atomtronic diode. The small (large) population of the second many-body band in the P-type (N-type) material yields the analog of the small (large) thermal electron population of the conduction band in a semiconductor. The states of the P-type and N-type materials at zero voltage are represented by the squares. Arrows indicate the chemical potential difference (voltage) imposed to obtain a reverse (left) and a forward biased junction (right).

to the N-component. The larger the applied voltage, the larger the generated current. When the battery contacts are switched, the diode is reverse biased. As the voltage is increased a small current starts flowing. However, as soon as the voltage is large enough to make the battery chemical potentials enter the insulating zones, the current can not increase any further. As a consequence, the current-voltage curve is asymmetric. The remnant current obtained in reverse bias, the saturation current, becomes smaller as the components' initial states are moved closer to the insulating phase.

Figure 4.7 presents a schematic comparison of the conduction band of an electronic and an atomtronic diode obtained using a step potential. For the atomtronic diode, the fact that only a small current can flow in reverse bias is not due to the presence of a voltage-dependent energy barrier at the junction as in the electronic case. Instead, it arises from the battery chemical potentials moving into insulating zones corresponding to a full conduction band on the N-side and an empty conduction band on the P-side.

An important difference between electronic and atomtronic case is the opposite direction of current flow. In forward bias, atoms flow from the P-type to the N-type material as opposed to the other way around for electrons in a semiconductor.

Figure 4.9 displays the highly asymmetric current-voltage curve obtained from our calculation. The potential step is chosen such as to yield an equilibrium configuration with a filling of 1.99 and 1.01 atoms on the N-side and P-side respectively. In this configuration, we obtain a reverse saturation current of 0.14 $J/\hbar$ while in forward bias, currents can exceed 1.4 $J/\hbar$. Note that the current changes strongly in the vicinity of $V = 0$. This is reminiscent of the behavior of an electronic diode as the temperature approaches zero. Reducing the potential step lowers the population difference between P-type and N-type materials at equilibrium and leads to an increase in saturation current and to a decrease in the slope of the current-voltage curve around $V = 0$.

The diode currents have been calculated in the same manner as the currents carried by atomtronic wires except for the addition of the potential energy step between the two sites (see Appendix for details of calculations).

4.5 Atomtronic Transistor

As in electronics, the highly asymmetric current-voltage curve of atomtronic diodes can be exploited to build a transistor. Bipolar junction transistors (BJT) are circuit elements that can serve as amplifiers and switches. In electronics, they consist either of a thin P-type layer sandwiched between two N-type components (NPN) or a thin N-type layer between two P-type components (PNP). For our discussion, we consider an NPN configuration. A detailed discussion of semiconductor bipolar junction transistors can, for example, be found in [8]. The basic circuit schematic is displayed in Fig. 4.10. The voltage V_{BC} that is applied to the PN-junction formed by the middle component, the base, and one of the outer components, the collector, puts this junction into reverse bias. At the same time, the other junction formed by the base and the

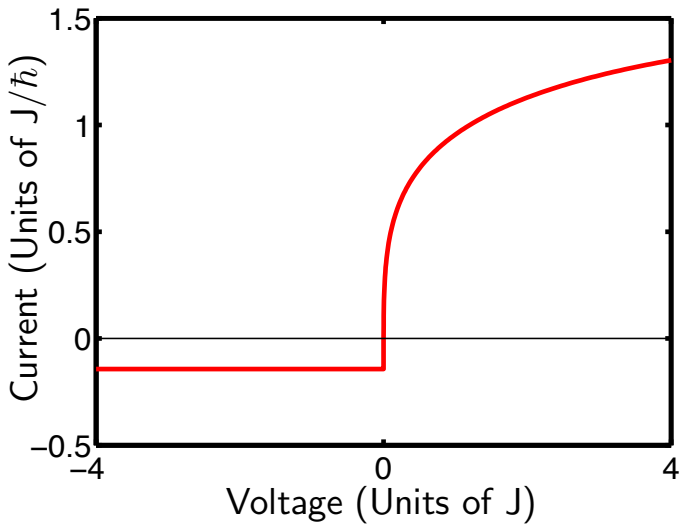

Figure 4.9: The characteristic current-voltage curve for an atomtronic diode. The larger the forward bias (voltage > 0), the higher the current of atoms flowing from the P-component and to the N-component. In reverse bias (voltage < 0) the current saturates since the particle transfer between battery and system can not be increased beyond a certain small value when the battery pole chemical potentials enter insulating zones where $\partial n/\partial \mu = 0$.

other outer component, the emitter, is put into forward bias by applying a voltage V_{EB}. The key idea is to use the voltage V_{EB} to control the current I_C leaving the collector element and thereby achieve differential gain in I_C relative to the base current I_B. At $V_{EB} = 0$ one is simply dealing with the reverse biased base-collector junction. In this case, the currents I_C and I_B both equal the small reverse bias saturation current of the base-collector junction. The collector current I_C grows drastically when V_{EB} is increased such that the emitter-base junction is forward biased. This effect relies on the base region being very thin. The forward bias gives rise to a flow of electrons from the emitter into the base region, thereby significantly increasing the number of electrons at the base-collector junction. Recall that at $V_{EB} = 0$, the base is depleted of electrons by the reverse bias V_{BC}. The emitter-base junction thus serves to greatly modify the number of carriers in the base that are subjected to the base-collector reverse bias. This leads to an increase of I_C beyond the saturation current. Since the base is extremely

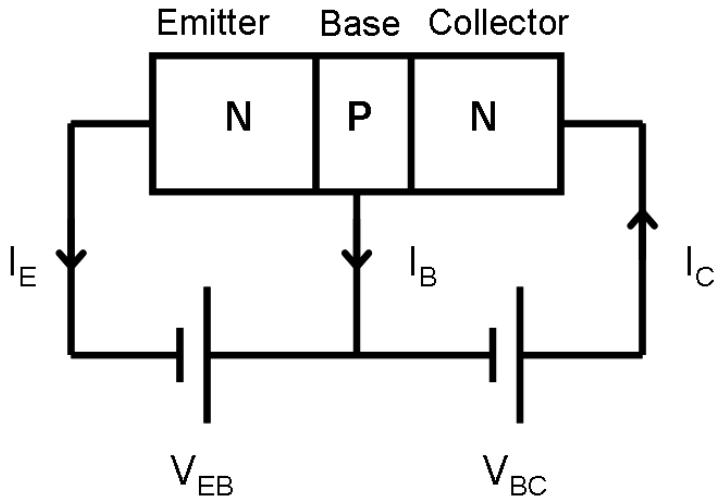

Figure 4.10: Circuit schematic of an electronic or atomtronic bipolar junction transistor of the NPN-type. A thin P-type component (base) is sandwiched between two N-type components (emitter and collector). The key feature is that the voltage V_{EB} can be used to obtain gain in the collector current I_C relative to the base current I_B.

thin there is less opportunity for the electrons to leave the base compared to entering the collector. Because of this, most of the current that enters the base from the emitter moves on to the collector instead of it leaving out the base terminal. Therefore the relative changes in the current from the base I_B and from the collector I_C yields a large differential gain dI_C/dI_B.

These key features of an electronic transistor can be translated into atomtronics with atoms taking the place of electrons. The important point is to mimic the carrier densities and thus the fillings of the three components. This can be achieved by doping or, equivalently, by using potential steps. As with the diode, we focus on the latter implementation. The atomtronic transistor can be created by setting up a configuration such that for zero voltage the conduction bands of the left and right regions have a large filling compared to the sandwiched thin base region. The phase diagram for such an arrangement is depicted in Fig. 4.11(a), where the squares represent the equilibrium configuration, while the arrows indicate the way the battery chemical potentials are

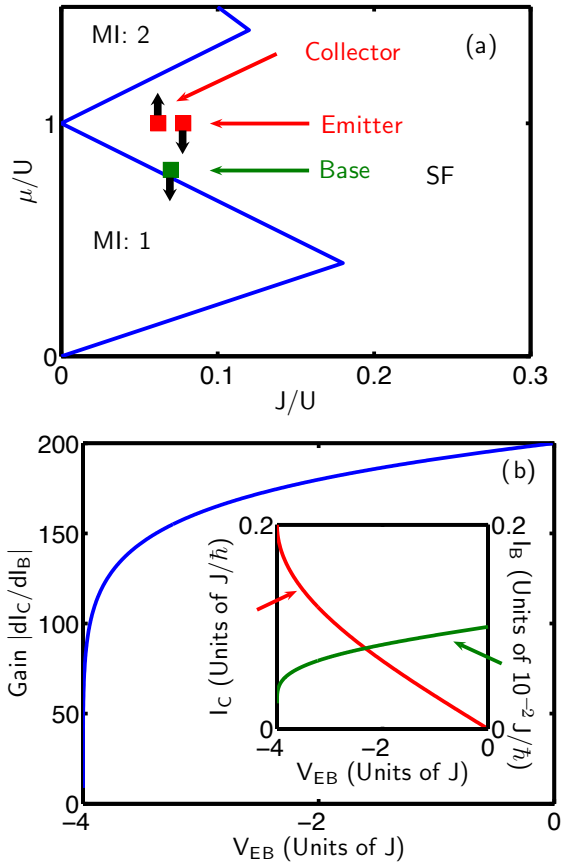

Figure 4.11: (a) The squares indicate the equilibrium configuration of an atomtronic bipolar junction transistor in the phase diagram while the arrows show the direction in which the chemical potentials of the battery contacts are varied. (b) Differential gain dI_C/dI_B as a function of emitter-base voltage V_{EB}. Inset: Base current and collector current as a function of emitter base voltage. The voltage is changed by varying the emitter contact potential from $\mu(n_E = 1)$ to $\mu(n_E = 1.5)$. The base contact is kept at $\mu(n_B = 1)$ right below its equilibrium value $\mu(n_B = 1.005)$ while the collector contact is kept at the equilibrium value $\mu(n_C = 1.5)$.

tuned. A small voltage is applied to the collector-base junction such that a small current flows from the collector into the base. When the emitter battery chemical potential μ_E is lowered, atoms move from base to emitter and leave through the emitter, giving rise to a non-zero emitter current I_E. As a back-effect, this leads to an increase in I_C since the fast removal of atoms from the base through the emitter allows more atoms to move into the base from the collector.

Meanwhile, the base current I_B becomes smaller the further the emitter chemical potential μ_E is lowered. This is due to the base being very thin relative to the emitter and the collector, so atoms traverse preferentially from collector to emitter rather than leaving out the base contributing to I_B. The effect of the forward bias V_{EB} on the base current I_B is thus opposite to its effect on I_C. Therefore, our atomtronic transistor features an inverted amplification in which a small decrease in the base current goes along with a large increase in the collector current (negative gain).

An example for the behavior of the currents in an atomtronic transistor is given in Fig. 4.11(b). The equilibrium configuration has 1.5 atoms per site in emitter and collector and 1.005 atoms per site in the base. In Fig. 4.11(b) we plot data obtained for the individual currents I_C and I_B upon variation of the emitter chemical potential μ_E while keeping the base battery contact at a chemical potential $\mu(n_B = 1)$ in the $n = 1$ Mott-insulating zone and the collector contact at $\mu(n_C = 1.5)$. To demonstrate differential gain we display the quantity $|dI_C/dI_B|$ as a function of V_{EB}. The details of the calculation are presented in the Appendix.

4.6 Atomtronics Conclusions

We have shown how strongly interacting ultracold bosonic gases in periodic potentials can be used as conductors and insulators in a circuit and how they can be employed to build atomtronic analogs of diodes and bipolar junction transistors. From here, the implementation of an atom amplifier is immediate. An atom amplifier is a device that allows control of a large atomic current with a small one. The transistor presented above directly serves this purpose since small changes in the base current bring along large changes in the collector current. It is straight-forward to conceive of more complex devices such as a flip flop, a bistable device that uses cross negative feedback between two transistors.

The similarity in qualitative behavior goes along with a number of significant

differences in the underlying physics. Firstly, in the atomic case the energy gap results from interactions rather than from statistics as in electronics. Secondly, the atomic currents are superfluid. As a consequence, the ratio between voltage and current has the meaning of a dissipationless resistance. Further differences arise in both diodes and transistors. Our atomtronic diode does not feature a depletion layer, i.e. it does not exhibit a voltage-dependent energy barrier at the junction. The asymmetry in the current-voltage curve results from voltage-sign dependent quantum phase transitions to an insulating phase. As a consequence, atoms flow from P-type to N-type in forward bias rather than flowing, as in electronics, from N-type to P-type. Note that this difference can not be resolved by drawing the analogy between atom holes and electrons rather than atoms and electrons since this would also require relabeling the N-type material as P-type and vice versa and hence the current direction would again be reversed in comparison to the electronic case. Due to the difference in diode behavior the atomic collector current in a transistor flows from collector into base and the emitter current flows from base into emitter, i.e. opposite to electronic flow in a NPN transistor. A significant difference in the qualitative behavior of electronic and atomtronic transistor is given by the gain being negative in the atomtronic case. The collector current increases as base current decreases. We expect that this does not affect the functionality of devices based on the operation of bipolar junction transistors. Yet, an adaptation of their design will be necessary.

The data presented in this chapter is obtained from calculations for a one-dimensional lattice. This choice is of an entirely practical nature. The basic ideas also hold for two- and three-dimensional cubic lattices and extend to other lattice geometries that make transitions between superfluid and insulating phases upon changes of the chemical potential.

Working with higher-dimensional lattices increases the magnitude of the currents that can be achieved. In an one-dimensional optical lattice with an experimentally

realizable depth of $10\,E_R$ the hopping parameter $J \sim 0.02E_R$, where $E_R = \hbar^2\pi^2/2md^2$ is the recoil energy which is fixed by the lattice period d. For $87Rb$ and a lattice period of $d = 400nm$, the recoil energy is $E_R = (2\pi\hbar)3.55kHz$ yielding currents on the scale $J/\hbar \sim 2\pi 71Hz$. This implies, that the currents through a three-dimensional lattice of the same period and depth with a cross-section of 10×10 sites are of the order $100 \times 2\pi 71Hz$.

Experiments aimed at atomtronic devices will be challenging given the current status of ultracold atom technology. Among other challenges is the need to combine atomic potentials that have typically been demonstrated in isolated systems, and, moreover, is the need to spatially cascade regions in which atoms undergo nonlinear interactions. An optical lattice, for example, might well serve as the basis for fabricating atomtronic P-type and N-type materials. Alternatively, lattice potentials could be created by passing current through micro-fabricated wires on a chip surface. And perhaps coupling an atom magnetic waveguide to an optical or non-optical lattice as a means of transporting atoms to and from the lattice can set the stage for atom diode experiments. In principle, atom chips provide the means for supporting different types of atomic potentials on a single substrate. The lattice systems used in atomtronic circuits do not necessarily have to support coherent currents. The important feature is that the system's tendency to accept or not accept particle transfer from the battery exhibits the incompressibility associated with the Mott insulating phase. We have provided a conceptual framework of semiconductor material and device analogs that can serve as building blocks to more sophisticated atomtronic devices and circuits. A discussion of actual atomtronic device implementation necessarily goes beyond the scope of this work. Pepino, et. al., have further developed methods for constructing devices from multiple transistors, such as quantum logic gates [125].

Finally, it is important to keep in mind that this chapter develops atomtronics within the Bose-Hubbard model. This model provides an excellent description of ongo-

ing experiments with ultracold bosonic atoms in optical lattices. Other Hamiltonians might offer alternative ways of drawing the analogy with electronics. A natural choice for further study are Hamiltonians describing bosons with beyond onsite interactions and Hamiltonians for fermionic gases.

Chapter 5

Photons Interacting in a Cavity

The interactions between light and matter can be examined from several perspectives. The previous chapters showed how the properties of atoms can be altered by the presence of an electromagnetic field. The intensity of the electromagnetic field, in the form of an optical lattice, is able to enhance the effects of atomic two-body interactions relative to the kinetic energy of the atoms. In this chapter, the interactions between light and atoms are examined from the perspective of the properties of the photons. In the presence of an atomic field, photons can exhibit many interesting properties, the most famous of which is lasing. Effective photon-photon interactions mediated by atoms can also arise. This chapter presents the Hamiltonian that is used to describe the properties of a collection of photons confined to a cavity filled with a nonlinear medium. The nonlinear medium could be created in several ways. For instance, a Rydberg gas of atoms or the deposition of a nonlinear crystal can be used. For the description of this system, it is useful to consider the medium as a collection of two-level atoms.

In this chapter, a model of a photon fluid confined to a nonlinear Fabry-Perot cavity will be presented. First, the bare modes of the cavity are briefly discussed. Then the Hamiltonian of the photon fluid is derived by examining the nonlinear polarizability of the nonlinear atomic medium. Several properties of a photon fluid are then examined.

5.1 Photon Modes of the Cavity

In deriving the Hamiltonian that describes the evolution of a collection of photons confined to a cavity interacting via atomic coupling, it is important to accurately describe the bare modes of the cavity. These photon modes which are associated with a vacuum cavity with perfectly conducting walls will be used as the basis states of the system. The system is then an electromagnetic field in a cavity, which we may take to be a box of lengths l_x, l_y, and l_z. The walls of the cavity will be considered perfect conductors and the interior of the cavity will have no electric polarizability or magnetization. Maxwell's equations and the boundary conditions completely define the system.

Each mode of the cavity is identified by three quantum numbers, n_i, one for each direction, and a polarization direction. As long as none of the n's are zero, there are two independent polarizations for each set of quantum numbers. If an n is zero , then there is only one possible polarization. Note that if two or more of the n's are zero, then the field vanishes. If n_i is zero, then the polarization is in the i direction.

5.2 Quantum Hamiltonian

Here we construct the quantum Hamiltonian for an electromagnetic field interacting with a nonlinear medium. The energy density of an electromagnetic field in a medium is given by

$$U = \frac{1}{2}\left(\vec{E}\cdot\vec{D} + \vec{B}\cdot\vec{H}\right) , \tag{5.1}$$

where $\vec{D} \equiv \epsilon_0\vec{E} + \vec{P}$ and $\vec{H} \equiv \vec{B}/\mu_0 - \vec{M}$, $\vec{P}$ is the polarization, and $\vec{M}$ is the magnetization. If the the medium has zero magnetization, the Hamiltonian is given by

$$H = \frac{1}{2}\int_V \left(\epsilon_0\vec{E}\cdot\vec{E} + \vec{B}\cdot\vec{B}/\mu_0 + \vec{E}\cdot\vec{P}_{nl}\right) , \tag{5.2}$$

where $\vec{P}_{nl} \equiv \vec{P} - \epsilon_0\vec{E}$ is the nonlinear part of the polarization. It will be this polarization that must be calculated by examining the interactions of the photons and the medium in

the cavity. It is then straight forward to use traditional second quantization techniques on the photon modes to obtain the Hamiltonian

$$\hat{H} = \sum_i \left(\hbar\omega \left(\hat{a}_i^\dagger \hat{a}_i + \frac{1}{2} \right) + \frac{1}{4} \int_V \left(\hat{E}_i \cdot \hat{P}_{nl} + \hat{P}_{nl} \cdot \hat{E}_i \right) \right) , \tag{5.3}$$

where

$$\vec{E}_i = \hat{a}_i \vec{E}_i^- e^{-i\omega_i t} + \hat{a}_i^\dagger \vec{E}_i^+ e^{i\omega_i t} , \tag{5.4}$$

is the electric field operator of mode i with energy $\hbar\omega_i$, $\hat{a}_i$ is the annihilation operator for a photon in mode i, and $\vec{E}_i^- = \vec{E}_i^{+*}$ contains the spatial dependence of the mode.

5.2.1 Polarization of Atoms

The dipole moment characterizes the polarization of the medium. We will therefore calculate the dipole moment of an atoms that creates the nonlinearity polarization. It is useful to return momentarily to a classical description of the multi-mode light field,

$$\vec{E} = \sum_i \vec{E}_i \cos(\omega_i t) . \tag{5.5}$$

where mode i has energy $\hbar\omega_i$, and later we will quantize the photons,

$$\vec{E}_i \rightarrow \hat{a}_i \vec{E}_i + \hat{a}_i^\dagger \vec{E}_i^* , \tag{5.6}$$

The polarization of a two level atom is given by

$$\vec{P} \equiv Tr(e\hat{r}\hat{\rho}) \tag{5.7}$$

$$= e \sum_C \sum_{ij} \langle j|C|i\rangle \rho_{ij} \hat{C} , \tag{5.8}$$

where $C \in \{x, y, z\}$ represents each direction and $\hat{\rho}$ is the density matrix decribing the atomic degrees of freedom. This formula simplifies since only states of differing parity are connected. We are therefore left with,

$$\vec{P} = e \sum_C \sum_e \langle g|C|e\rangle \rho_{eg} \hat{C} + c.c. \tag{5.9}$$

$$= \sum_e \rho_{eg} \sum_C e\langle g|C|e\rangle \hat{C} + c.c. \tag{5.10}$$

$$= \sum_e \rho_{eg} \vec{d}^{e*} + c.c. , \tag{5.11}$$

where $\vec{d^e} \equiv \langle e|e\vec{r}|g\rangle$ is the dipole moment between ground state g and excited state e.

It is now necessary to calculate the components of the density matrix. The Hamiltonian describing the interaction between the atom and the photons, without spontaneous emission, is given by

$$\hat{H} = \hbar\omega_e \sum_e |e\rangle\langle e| + \hbar\omega_g |g\rangle\langle g| + \sum_e V_{eg}|e\rangle\langle g| + \sum_e V_{ge}|g\rangle\langle e| \tag{5.12}$$

where ω_e is the energy of the excited state, ω_g is the energy of the ground state, and

$$V_{eg} = -\vec{d^e} \cdot \vec{E}\,. \tag{5.13}$$

The dipole approximation can be used since the wavelength of the electromagnetic field is much larger than the atomic size and so the electric field can be assumed to have the value at the center of the atom. Note that this is the same Hamiltonian that was used to describe the creation of an optical lattice earlier in this thesis and the same approximations used still hold such as the use of the dipole approximation and the rotating-wave approximation.

The density matrix equation of motion in which spontaneous emission from the excited states to the ground state is allowed is given by

$$\dot{\hat{\rho}} = -\frac{i}{\hbar}\left[\hat{H}, \hat{\rho}\right] - \frac{\Gamma}{2}\sum_i \left[\hat{\sigma}^i_+\hat{\sigma}^i_-\hat{\rho} + \hat{\rho}\hat{\sigma}^i_+\hat{\sigma}^i_- - 2\hat{\sigma}^i_-\hat{\rho}\hat{\sigma}^i_+\right], \tag{5.14}$$

where Γ is the spontaneous emission rate, $\hat{\sigma}^i_+$ is the raising operator from the ground state g to the excited state i and $\hat{\sigma}_-$ is the lowering operator. The effects of spontaneous emission is found by following a traditional master equation formalism and ending with terms of the Lindbladt form as seen in Eq. (5.14).

The density matrix equation of motion, Eq. (5.14), can be rewritten in terms of the individual components. The matrix elements can be broken up into three sets, whose equations are given by

$$\dot{\rho}_{eg} = -\left(\frac{\Gamma}{2} + i\Omega\right)\rho_{eg} - \frac{i}{\hbar}\left(V_{eg}\rho_{gg} - \sum_f V_{fg}\rho_{ef}\right), \tag{5.15}$$

$$\dot{\rho}_{ef} = -\Gamma\rho_{ef} - \frac{i}{\hbar}\left(V_{eg}\rho_{gf} - V_{gf}\rho_{eg}\right) , \tag{5.16}$$

$$\dot{\rho}_{gg} = \sum_e \left(\Gamma\rho_{ee} + \left[\frac{i}{\hbar}V_{eg}\rho_{ge} + c.c.\right]\right) , \tag{5.17}$$

where $\Omega \equiv \omega_e - \omega_g$ is the atomic transition frequency and both e and f refer to excited states.

Just as the electric field is composed of a set of frequency dependent terms, the elements of the density matrix can be expanded in a Fourier series,

$$\rho_{eg} = \sum_n \rho_{eg}^n e^{-i\omega_n t} , \tag{5.18}$$

for example. Since the interaction terms V_{eg} are linear in the electric field, expanding in a Fourier series removes the temporal components of the density matrix equations of motion. It is then possible to write the density matrix elements in a series expansion of the electric field modes, e.g.,

$$\rho_{eg}^n = \rho_{eg}^{n(0)} + \sum_{ijf_1f_2} \rho_{eg}^{n(ij)} \left(\vec{E}_i \cdot \vec{d}^{f_1}\right)\left(\vec{E}_j \cdot \vec{d}^{f_2}\right) + \cdots . \tag{5.19}$$

As long as the population of the atomic excited state is small, terms beyond second order can be neglected. This corresponds to an electric field that is far-detuned from the atomic transition. The elements of the density matrix can be solved for and replaced back into the equation for the polarization, Eq. (5.11). Under these assumptions, the polarization of the atoms up to the first two nonvanishing orders of electric field is given by

$$\begin{aligned}
\vec{P} = {} & in\sum_i D(\omega_c)\frac{|\vec{d}|^2}{2\hbar}e^{-i\omega_i t}\vec{E}_i \\
& -in\sum_{ijk} D(\omega_k+\omega_j-\omega_i)\frac{|\vec{d}|^4}{8\hbar^3}\frac{D^*(\omega_i)+D(\omega_j)}{\Gamma - i(\omega_j-\omega_i)}e^{-i(\omega_k+\omega_j-\omega_i)t}(\vec{E}_i^* \cdot \vec{E}_j)\vec{E}_k \\
& -in\sum_{ijk} D(\omega_k+\omega_j-\omega_i)\frac{|\vec{d}|^4}{8\hbar^3}\frac{D^*(\omega_i)+D(\omega_k)}{\Gamma - i(\omega_k-\omega_i)}e^{-i(\omega_k+\omega_j-\omega_i)t}(\vec{E}_i^* \cdot \vec{E}_j)\vec{E}_k \\
& +c.c. ,
\end{aligned} \tag{5.20}$$

where n is the atomic density,

$$D(\omega) \equiv \frac{1}{\frac{\Gamma}{2} + i(\Omega - \omega)}\,, \tag{5.21}$$

is a detuning factor, and Ω is the atomic transition frequency. Note that this is still a spatially dependent polarization.

5.2.2 Fourth Order Hamiltonian

It is now possible to create the Hamiltonian describing the atom-mediated photon-photon interactions. In the rotating-wave approximation, only energy conserving terms remain. By replacing the polarization from Eq. (5.21) into the original Hamiltonian of Eq. (5.3) and using the quantized form of the light from Eq. (5.6), a new Hamiltonian up to the two lowest orders of the electric field is found. The Hamiltonian is then given by

$$H \;=\; \sum_i \hbar\omega_i \left(1 + \Delta_i\right) \hat{a}_i^\dagger \hat{a}_i + \sum_{ijkl} \Gamma_{ijkl} \hat{a}_i^\dagger \hat{a}_j^\dagger \hat{a}_k \hat{a}_l \tag{5.22}$$

where the Hamiltonian has been written in proper normal ordering. The factor Δ_i is an adjustment of the mode energies due to the linear polarizability of the medium and can be approximated by $\Delta_i \approx \Delta_0$ and incorporated into the bare mode frequencies since $(\omega_i - \omega_0)/\Gamma \ll 1$. The process of a single photon temporarily interacting with an atom and quickly leaving creates this polarization and is dependent on the parameters of the medium. For the fourth order term, we need only consider the zeroth order contribution to Γ_{ijkl}, since again $(\omega_i - \omega_0)/\Gamma \ll 1$. This term becomes

$$\Gamma_{ijkl} \;\approx\; -n \frac{L_0^2 \Omega_0 \omega_0^2 |\vec{d}|^4}{16\epsilon^2 \hbar} \int_V (\vec{E}_i \cdot \vec{E}_k^*)(\vec{E}_j^* \cdot \vec{E}_l)\,, \tag{5.23}$$

where

$$L_0 \equiv \frac{1}{\frac{\Gamma^2}{4} + (\Omega - \omega_0)^2}\,, \tag{5.24}$$

and depends on the overlap integral of photons wave functions. Note that the approximations to the coupling terms do not have to be explicitly made and can for a general system be frequency dependent.

The presence of the overlap integrals in Eq. (5.23) leads to several properties of the system since they describe the rates at which photons can interact, if at all. Only if the addition or subtraction of the quantum numbers for each mode can be set equal to zero in each direction is an interaction allowed. This can be understood from the perspective that a standing wave can be thought of as two counter-propagating waves with opposite momentum. Therefore, even though the full mode has zero momentum since it is trapped in a cavity, one of the waves can still interact with a wave from another mode. Only if this collision satisfies momentum conservation is the interaction allowed. This is how momentum conservation plays a role in the photonic collisions. The quantum number can also be thought of being related to the standard deviation of the momentum of the mode.

There are three types of interactions that occur. The first kind are nonlinear self-interaction terms of the form,

$$V \propto \hat{a}_i^\dagger \hat{a}_i^\dagger \hat{a}_i \hat{a}_i \,. \tag{5.25}$$

These interactions create a mean-field energy shift in the photon modes. Interactions of the form,

$$V \propto \hat{a}_i^\dagger \hat{a}_j^\dagger \hat{a}_j \hat{a}_i \,, \tag{5.26}$$

conserve the number of photons in each mode and again lead to a mean field energy shift but are due to the interactions of two different modes. Self interactions are a subset of these interactions. Interactions of the form,

$$V \propto \hat{a}_i^\dagger \hat{a}_j^\dagger \hat{a}_k \hat{a}_l \,, \tag{5.27}$$

actually change the photon mode populations, and are the only ones to do so. These types of interactions are those associated with effects such as four wave mixing.

5.3 Photon Fluid

A weakly interacting photon gas has become known as a photon fluid [33]. This fluid possesses the same Bogoliubov dispersion relation for elementary excitations as that of a weakly interacting Bose gas of atoms. In addition, the photonic system possesses a well defined chemical potential, which noninteracting photons lack. These properties imply that the photon fluid system admits a superfluid state of light.

The Bogoliubov excitations can easily be seen by examining the Hamiltonian of the photon fluid, which can be expressed as,

$$\hat{H} = \sum_{p} \hbar\omega(p)\hat{a}_p^\dagger \hat{a}_p + \sum_{kpq} V(k)\hat{a}_{p+k}^\dagger \hat{a}_{q-k}^\dagger \hat{a}_p \hat{a}_q \,, \tag{5.28}$$

where

$$\omega(k) = c\sqrt{k_x^2 + k_y^2 + k_z^2}\,. \tag{5.29}$$

This describes the scattering of photons with momentum transfer k. The free energy of a photon is then given by

$$E = c\sqrt{p_\perp^2 + m^2c^2} \tag{5.30}$$

where $p_\perp^2 \equiv \hbar\sqrt{k_x^2 + k_y^2}$ and $mc \equiv \hbar k_z = \hbar n\pi/L$. If $p_\perp^2 \ll p_z^2$, then the energy can be approximated by a Taylor expansion to yield,

$$E \approx mc^2 + \frac{p_\perp^2}{2m}\,. \tag{5.31}$$

The zero-point energy can be offset to remove the constant mc^2 factor. For a large number of photons in the ground state mode, $N_0 \gg N_i$, a mean-field approximation can be made in which $\hat{a}_0 = \sqrt{N_0}$. In this case, the Hamiltonian becomes,

$$\hat{H} = \sum_{p>0} \epsilon'(p)\hat{a}_p^\dagger \hat{a}_p + N_0 \sum_{p>0} V(p)\left(\hat{a}_{+p}^\dagger \hat{a}_{-p}^\dagger + \hat{a}_{+p}\hat{a}_{-p}\right) + V(0)N_0^2 \tag{5.32}$$

where

$$\epsilon'(p) \equiv \left(\frac{p_\perp^2}{2m} + N_0 V(p) + N_0 V(0)\right)\,, \tag{5.33}$$

and collisions of two high energy photons has been neglected since their populations are very small, $N_0^2 \gg N_0 N_i$.

It is possible to diagonalize this quadratic form of the Hamiltonian using traditional Bogoliubov methods. With the canonical transformation,

$$\hat{\alpha}_p = u_p \hat{a}_p + v_p \hat{a}_{-p}^\dagger \tag{5.34}$$

$$\hat{\alpha}_p^\dagger = u_p \hat{a}_p^\dagger + v_p \hat{a}_{-p} \tag{5.35}$$

in which $u_p^2 - v_p^2 = 1$, the Hamiltonian becomes

$$\hat{H} = constant + \sum_p \omega'(p) \left(\hat{\alpha}_p^\dagger \hat{\alpha}_p + \frac{1}{2} \right) \tag{5.36}$$

with

$$\hbar\omega'(p) = \sqrt{\frac{p^2 N_0 V(p)}{m} + \frac{p^4}{4m^2}} \,. \tag{5.37}$$

This is the same form as the traditional Bogoliubov dispersion relation. When the momentum is small, the excitation spectrum is linear and, therefore, excitations behave as phonons. For larger momenta, the quasi-particles have a quadratic dispersion relation and behave as massive, nonrelativistic free particles. This transition occurs at a momentum of approximately

$$p_c = 2\sqrt{m N_0 V(p_c)} \,. \tag{5.38}$$

Figure 5.1 presents the excitation spectrum with the assumption of a constant interaction strength, $V(p) = V(0)$. For small momenta, the spectrum is given by

$$\hbar\omega = p\sqrt{\frac{NV}{m}} \,, \tag{5.39}$$

and for large momenta the spectrum becomes quadratic

$$\hbar\omega = \frac{p^2}{2m} + NV \,. \tag{5.40}$$

Large momentum excitations are essentially massive free particles with a mean-field interaction energy offset.

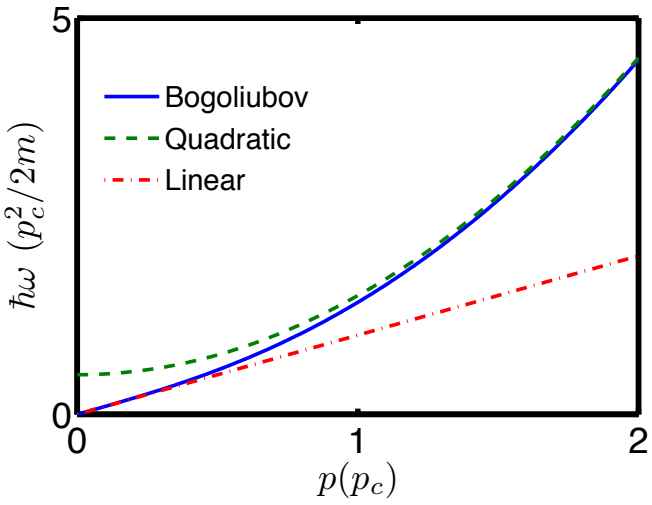

Figure 5.1: The solid line is the dispersion relation for excitations of the ground state of a photon fluid. The dashed curve is the quadratic free-particle spectrum associated with high energy excitations. The dash-dot curve is the characteristic linear component of the spectrum which describes phonon-like excitations.

The Bogoliubov dispersion relation implies that the photon fluid should exhibit the property of superfluidity in which dissipationless flow occurs. The transition between dissipation less flow and turbulent flow should occur at a well defined critical velocity. In addition, the occurrence of quantized vortices would be a sign of superfluidity.

The photon fluid has another property that distinguishes it from traditional states of light. The chemical potential of a photon fluid is nonvanishing, since,

$$\mu = \frac{\partial \langle \Psi | H | \Psi \rangle}{\partial N} \neq 0\,. \tag{5.41}$$

In the limit of large photon number and low temperature, the energy of the condensate is dominated by the photon-photon interactions in the ground state mode,

$$E \approx N^2 V(0)\,, \tag{5.42}$$

which leads to a chemical potential of,

$$\mu \approx N V(0)\,. \tag{5.43}$$

The chemical potential is due to the atom-mediated photon-photon interactions which are not present in traditional systems of light.

Chapter 6

Evaporative Cooling of a Photon Fluid to Quantum Degeneracy

The phenomenon of coherence has played a crucial role in many areas of physics, in particular with the various states of light [59, 58, 159]. The extraordinarily long coherence time is the fundamental property that distinguishes laser light from ordinary light. The extensive coherence properties of matter have recently been investigated in trapped ultracold atoms by studying de Broglie matter waves in Bose-Einstein condensates [6, 39, 19]. Coherence is a ubiquitous phenomenon: many other systems, such as a collection of polaritons [11], also show similar coherent attributes.

In the case of atoms, coherence presents itself when the atomic gas has been condensed to quantum degeneracy. Condensation is often achieved using the technique of evaporative cooling in which the highest energy atoms are forced to escape the trap, and those that remain rethermalize through binary collisions at lower and lower temperature. In a nonequilibrium system, continuous evaporative cooling may generate a coherent atom laser [77]. In this chapter, we demonstrate how evaporative cooling and Bose stimulated emission can be used to condense a photon fluid into a quantum degenerate superfluid [155]. In a general sense, a photon fluid is a collection of spatially localized photons which, through their interactions via a nonlinear medium, exhibit hydrodynamic or similar fluidic behavior.

A condensed photon fluid should possess superfluid properties such as coherence, phase rigidity, quantized vortices, a critical Landau velocity, and the usual Bogoliubov

dispersion [33]. This is distinct from a normal laser, where the effective photon interactions are so weak that they are unimportant. Another significant difference with usual lasers is that it is not necessary to have a population inversion of an internal atomic state, and instead the phase-space compression to produce a macroscopically occupied mode relies on an inversion of photon cavity mode populations with respect to the traditional Planck distribution. Since the relevant modes of the system are determined by the structural properties of the cavity and not atomic quantities, the frequency of the coherent field could be highly tunable.

Two high-reflectivity mirrors placed close together form a Fabry-Perot cavity and support many photon modes. The closeness of the mirrors creates a cavity mode volume which has a high aspect ratio, with large energy gaps between modes which have adjacent longitudinal quantum numbers and small energy gaps between modes which have adjacent transverse quantum numbers. We utilize this to pump the cavity such that only one longitudinal quantum number is relevant, and the modes considered are distinguished only by their transverse degrees of freedom. Photons in vacuum interact weakly, therefore, it is necessary to incorporate a nonlinear medium, such as an atomic Rydberg gas or nonlinear crystal, into the cavity to allow for atom-mediated photon-photon interactions. Since the longitudinal degree of freedom is frozen out by having a small cavity length, an intriguing link exists between this systems and condensation in two-dimensions with the well-known physics of the Berezinskii-Kosterlitz-Thouless transition, which has recently been investigated in atomic gases [69, 150].

6.1 System Dynamics

The photon fluid in a Fabry-Perot cavity is governed by the Hamiltonian

$$\hat{H} = \sum_i \hbar\omega_i \hat{a}_i^\dagger \hat{a}_i + \sum_{ijkl} \hbar\Gamma^C_{ijkl} \hat{a}_i^\dagger \hat{a}_j^\dagger \hat{a}_k \hat{a}_l \,, \tag{6.1}$$

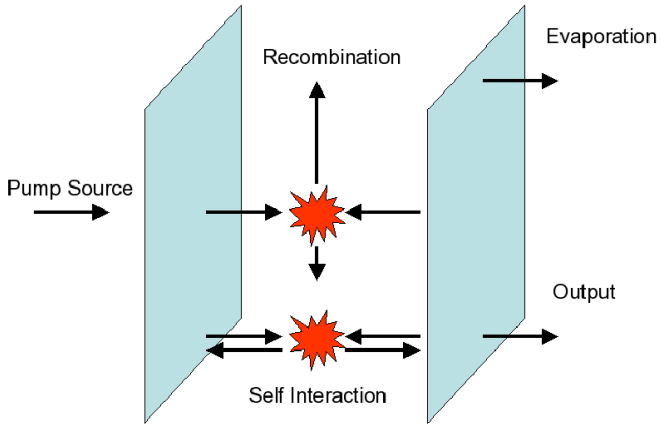

Figure 6.1: The five primary processes that occur in the Fabry-Perot cavity are presented. Photons enter the system from a pumping source. While in the cavity, the photons recombine and self-interact. Finally, the photons can leave the cavity through evaporation or output coupling. The combination of these processes allows for a conditions suitable for the evaporative cooling of a photon fluid.

where $\hat{a}_i$ is the annihilation operator for a photon in mode i with energy $\hbar\omega_i$, and Γ^C_{ijkl} is the scattering or collision (C) rate for photons from modes k and l into modes i and j. Note that the mode energy $\hbar\omega_i$ contains the bare mode energy of the photons as well as the energy due to the linear polarization of the medium in the cavity. The collision rates are due to the nonlinear polarizability of the medium in the cavity. This is the Hamiltonian that was derived and examined in the previous chapter. There are two kinds of interactions, as illustrated in Fig. 6.1. Terms which do not change populations give rise to a self-interaction energy and leave the photons in the same mode they entered in, e.g. $\hat{a}_0^\dagger \hat{a}_1^\dagger \hat{a}_1 \hat{a}_0$. Population transfer is due to recombination terms, such as $\hat{a}_0^\dagger \hat{a}_2^\dagger \hat{a}_1 \hat{a}_1$. The self-interaction terms will later be shown to have a dispersive effect on the coherence of the photons. The recombination terms will have a crucial role in developing a system capable of evaporative cooling methods.

Photons can also enter and leave the cavity through irreversible pumping and decay, which is not described by the Hamiltonian in Eq. (6.1). Pumping and decay can be incorporated into the system dynamics through the quantum master equation

formalism [110]

$$\frac{\partial\hat{\rho}}{\partial t} = -\frac{i}{\hbar}[\hat{H},\hat{\rho}] + \sum_i \Gamma_i^P \hat{L}[\hat{a}_i^\dagger] + \sum_i \Gamma_i^D \hat{L}[\hat{a}_i]\,, \tag{6.2}$$

where $\hat{\rho}$ is the density matrix operator of the system, Γ_i^P is the pumping rate (P) and Γ_i^D is the decay rate (D) for mode i, and the Lindbladt superoperator is

$$\hat{L}[\hat{O}] \equiv 2\hat{O}\hat{\rho}\hat{O}^\dagger - \hat{O}^\dagger\hat{O}\hat{\rho} - \hat{\rho}\hat{O}^\dagger\hat{O}\,. \tag{6.3}$$

The pumping rates across the spectrum of system modes are dependent on the pumping source, which for simplicity we take to be constant across all relevant modes, $\Gamma_i^P \to \Gamma^P$. It is possible to consider a pumping source that has a particular width or broadness in the modes being pumped. This can correspond to a narrow or broad bandwidth laser that pumps the system. The pumping width corresponds to a particular energy spectrum of modes being pumped. This can be implemented by considering all modes below a given energy pumped with the same pumping strength, Γ^P. The remaining modes can then be considered to remain unpumped.

Evaporative cooling requires a decay rate from the cavity which is strongly dependent on the energy. A mirror with a frequency dependent reflectivity, which allows modes to decay at different rates, can be utilized. A reflectivity which drops for large frequencies can create conditions where high energy photons leave the cavity faster than low energy photons. Since a high energy photon carries away more than the average photon energy, subsequent rethermalization through photon interactions should reduce the system temperature, in much the same way as in the evaporative cooling of atoms.

We implement energy dependent reflectivity by dividing the decay rates into two classes. High energy photons (H) are described by a decay rate of Γ^H and low energy photons (L) by a decay rate of Γ^L with $\Gamma^H \gg \Gamma^L$. The large decay rate of the high energy modes means they can be eliminated in the following way. Consider an interaction in which photons from modes i and j create a photon of low energy in mode k and a photon of high energy in mode l. The rapid decay of mode l causes this process to be effectively

irreversible. This is described most simply by extracting such processes which involve a high energy mode from the reversible $\hat{H}$ term in Eq. 6.2, and adding them back to the density matrix evolution as an irreversible term of superoperator form

$$\Gamma^E \hat{L}[\hat{a}_k^\dagger \hat{a}_i \hat{a}_j]\,, \tag{6.4}$$

where $\Gamma^E \equiv (\Gamma^C)^2/\Gamma^H$ is the evaporation rate (E), taken to be constant. This evaporation rate comes from the master equation formalism in which the correlation

$$\langle \hat{a}_l(t)\hat{a}_l^\dagger(0) = e^{-\Gamma^R t}\,, \tag{6.5}$$

expresses the fast recombination rate involved. The system Hilbert space is now reduced and the high energy modes no longer appear in the theory explicitly.

Even with these simplifications, the problem is still intractable in general. The dimensionality of the Hilbert space grows exponentially with the number of photons in the lower energy modes of the system; the number of states of a system with N photons in M modes scales as

$$\frac{(N+M)!}{N!M!}\,. \tag{6.6}$$

Most of this complexity is uninteresting from the point of view of evaporative cooling of photons since it arises from all possible pathways to redistribute and entangle photons amongst the lowest energy modes. Consequently, we divide the system into what we will refer to as plaquettes, each plaquette consisting of a pair of modes i and j, which may interact to produce a photon in the lowest energy mode $k = 0$, and a photon in a high energy mode l which is lost through the mirrors rapidly. Adding the contributions from D distinct plaquettes as an incoherent sum of pumping rates into the ground state, the density matrix equation of motion in the interaction picture is

$$\begin{aligned} \frac{\partial\hat{\rho}}{\partial t} &= +\Gamma^P \sum_i \hat{L}[\hat{a}_i^\dagger] + \Gamma^L \sum_i \hat{L}[\hat{a}_i] \\ &\quad -i\Gamma^C \sum_i [\hat{a}_0^\dagger \hat{a}_i^\dagger \hat{a}_i \hat{a}_0, \hat{\rho}] + \Gamma^E \sum_{\langle ij\rangle} \hat{L}[\hat{a}_0^\dagger \hat{a}_i \hat{a}_j]\,, \end{aligned} \tag{6.7}$$

where the sum over $\langle i,j\rangle$ implies modes i and j are from the same plaquette.

Amongst the populations, the evolution time scales are not all equivalent. If only one or no atoms are in a plaquette, a slow evolution takes place on time scales governed by Γ^P and Γ^L. If two atoms are in a plaquette, however, and providing $\Gamma^E \gg \Gamma^P, \Gamma^L$, they will rapidly collide and form a ground state photon and a high energy photon which will evaporate away. Consistent with this is that we may neglect the possibility of three or more photons in a plaquette.

The basis states needed then describe the number of photons in each plaquette and the number of photons in the lowest energy mode. The precise occupation of the modes is not important, only how many plaquettes have a given number of photons. For instance, an arbitrary basis state $|\Psi\rangle$ can be uniquely identified with a reduced computational state described by

$$|\Psi\rangle \rightarrow |n, abcd\rangle \equiv |n, (00)^a (01)^b (11)^c (02)^d\rangle\,, \tag{6.8}$$

where n is the number of ground state photons, a is the number of plaquettes with no photons, b is the number of plaquettes with one photon, and c and d are the number of plaquettes with two photons in different modes or the same mode, respectively. When considering the normalization of the wave function it is necessary to consider the multiplicity of basis states that all correspond to the same computational basis state.

6.2 Photon Number Distribution

The photon number distribution is an important quantity to characterize the photon state since a coherent state has a Poissonian distribution while a thermal state has an exponentially decaying distribution. The populations of all states $|\Psi\rangle$ that can be expressed as $|n, abcd\rangle$ are given by

$$P_{n,abcd} \equiv \langle\Psi|\rho|\Psi\rangle\,. \tag{6.9}$$

We now take advantage of the natural separation of time scales by adiabatically eliminating the fast processes. This is implemented by solving for the fast variables in steady state and substituting back into the equations for the slow variables. The populations of states with a plaquette with two photons are then approximately given by their steady state values

$$P_{n,ab10} = \frac{2}{n+1}\frac{\Gamma^P}{\Gamma^E}P_{n,a(b+1)00}\,, \tag{6.10}$$

$$P_{n,ab01} = \frac{1}{n+1}\frac{\Gamma^P}{\Gamma^E}P_{n,a(b+1)00}\,, \tag{6.11}$$

as determined by Eq. 6.7 and Eq. 6.9. The evolution of the remaining populations is then determined by

$$\begin{aligned}\frac{\partial P_{n,a}}{\partial t} = & -2(n+D-a)\Gamma^L P_{n,a} \\ & -2(n+1+3D-a))\Gamma^P P_{n,a} \\ & +2(n+1)\Gamma^L P_{n+1,a} + 2n\Gamma^P P_{n-1,a} \\ & +2(D-a)\Gamma^P P_{n,a+1} + 4a\Gamma^L P_{n,a-1} \\ & +12a\Gamma^P P_{n-1,a-1}\,,\end{aligned} \tag{6.12}$$

where $P_{n,a} \equiv P_{n,a(D-a)00}$. When normalizing the populations it is necessary to properly weight the individual computational basis states,

$$1 = P_{n,D} + \sum_{a=0}^{D-1} \frac{2^{D-a}D!}{a!(D-a-1)!}\left(\frac{1}{D-a} + \frac{2}{n+1}\frac{\Gamma^P}{\Gamma^E}\right)P_{n,a}\,, \tag{6.13}$$

due to the many basis states that correspond to the same computational basis state.

The number distribution of photons in the low energy mode is highly dependent on the incoherent pumping rate and the number of plaquettes pumped. The pumping rate can be designated by an effective temperature, T,

$$e^{-\hbar\omega/k_BT} \equiv \frac{\Gamma^P}{\Gamma^L} = \frac{\bar{n}}{\bar{n}+1}\,, \tag{6.14}$$

where $\bar{n}$ is the number of photons that would be in each mode if the modes were isolated and non-interacting and ω is the bare mode energy. This temperature corresponds to

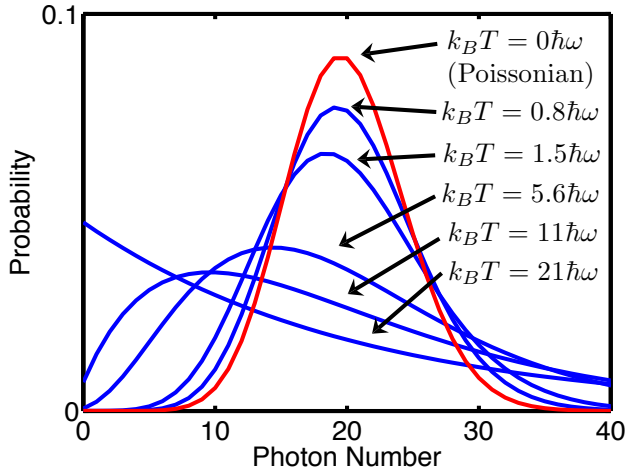

Figure 6.2: Photon number probability distribution of the lowest energy photon mode. As the pumping power per mode is decreased and more modes are pumped, denoted by decreasing T, the distributions change from an exponential decay to Poissonian, indicating a transition from a thermal to a superfluid state. The systems are described by $D = \{0, 1, 3, 20, 60\}$ pumped plaquettes and a pumping rate that sets 20 photons in the lowest energy mode.

the occupancy of the external pumping modes. In order to make effective comparison between different temperatures, we hold constant the average number of photons in the lowest energy mode, and vary both the temperature and correspondingly the energy width of the pump in order to maintain this condition. It would be expected that for an intense, narrow bandwidth pump connected only with the lowest energy mode of the cavity, the high temperature and incoherent characteristics of the pump would be imprinted on the photons in that mode. However, for a weaker but broader pump, in which a wider spectrum of modes are pumped but at a slower rate so that the average photon number remains the same, the lowest energy mode is not as influenced by the temperature of the pumping modes. The occupation of the lowest energy mode is due mainly to the recombination and stimulated emission which should create a coherent system.

Figure 6.2 presents the number distributions of photons in the lowest energy mode during steady state operation for systems with 20 photons in the low energy

mode. With a large effective temperature, as denoted in the figure by $k_B T = 21\hbar\omega$, the number distribution is essentially what would be expected for a thermal source. As the effective temperature decreases, by decreasing the pumping strength and increasing the number of pumped plaquettes, the effects of bosonic amplification dramatically increase. This leads to a nearly Poissonian number distribution associated with zero temperature condensates. The key to converting the incoherent thermal pump into a coherent system is that the occupation of the lowest energy mode comes from stimulated emission from higher energy modes and not the thermal pump. With over half of the photons in the lowest energy mode, the photons have entered quantum degeneracy and formed a condensate.

6.3 Photon Spectrum

The spectrum of the photons is also an important quantity to examine as it provides the coherence time and spectral width. Since the mode separation is greater than the collisional interaction energy and the system is in steady state, the fluctuation spectrum is determined by

$$S(\nu) \quad = \quad \int_{-\infty}^{\infty} d\tau e^{-i\nu\tau} \frac{\left\langle \hat{a}_0^\dagger(\tau)\hat{a}_0(0) \right\rangle}{\left\langle \hat{a}_0^\dagger(0)\hat{a}_0(0) \right\rangle}\,, \tag{6.15}$$

which is the Fourier transform of a two-time correlation function. The correlation function can be expressed as

$$\langle \hat{a}_0^\dagger(t)\hat{a}_0(0)\rangle = \sum_{n,\{i\}} \sqrt{n} C_{n,\{i\}}(t)\,, \tag{6.16}$$

with

$$C_{n,\{i\}}(t) \equiv Tr[\hat{\rho}|n,\{i\}\rangle\langle n-1,\{i\}|(t)\hat{a}_0(0)]\,, \tag{6.17}$$

where n is the number of ground state photons and $\{i\}$ represents the configuration of the remaining modes. According to the quantum regression theorem [110], the equation

of motion for the quantity $C_{n,\{i\}}$ is given by

$$\frac{\partial C_{n,\{i\}}}{\partial t} = \sum_{m\{j\}} M_{n\{i\}m\{j\}} C_{m,\{j\}} \,, \tag{6.18}$$

where the matrix elements are determined from the off-diagonal density matrix equation of motion

$$\frac{\partial \rho_{n\{i\},(n-1)\{i\}}}{\partial t} = \sum_{m\{j\}} M_{n\{i\}m\{j\}} \rho_{(m-1)\{j\},m\{j\}} \,, \tag{6.19}$$

as given by Eq. 6.7. Since this is a reduced set of the full density matrix equations of motion it is merely necessary to replace these matrix elements into Eq. (6.18) with the initial condition $C_{n,\{i\}}(0) = \sqrt{n} P_{n,abcd}(0)$ where $|n,\{i\}\rangle$ corresponds to the reduced basis state $|n, abcd\rangle$. As with the populations, it is convenient to work in the reduced computational basis states. Therefore, we consider quantities of the form

$$C_{n,abcd}(t) \equiv Tr[\hat{\rho}|n,abcd\rangle\langle n-1,abcd|(t)\hat{a}_0(0)] \,. \tag{6.20}$$

States with two excited photons in one plaquette are given by their steady state values

$$C_{n,ab10} = \frac{4\Gamma^P C_{n,ab+100}}{(2n+1)\Gamma^E + i(2n+b)\Gamma^C} \,, \tag{6.21}$$

$$C_{n,ab01} = \frac{4\Gamma^P C_{n,ab+100}}{2(2n+1)\Gamma^E + i(2n+b)\Gamma^C} \,. \tag{6.22}$$

The remaining terms are found by the equation of motion

$$\begin{aligned}
\frac{\partial C_{n,a}}{\partial t} = & -\Gamma^P(2n-1+6D-2a)C_{n,a} \\
& -\Gamma^L(2D-2a+2n-1)C_{n,a} \\
& -i(2n-2+D-a)\Gamma^C C_{n,a} \\
& +2\sqrt{n(n-1)}\Gamma^P C_{n-1,a} \\
& +2\sqrt{n(n+1)}\Gamma^L C_{n+1,a} \\
& +2\Gamma^P(D-a)C_{n,a+1} + 4\Gamma^L a C_{n,a-1} \\
& +\frac{8a\sqrt{n(n-1)}\Gamma^E\Gamma^P C_{n-1,a-1}}{(2n-1)\Gamma^E + i(2n+D-a-2)\Gamma^C} \\
& +\frac{32a\sqrt{n(n-1)}\Gamma^E\Gamma^P C_{n-1,a-1}}{2(2n-1)\Gamma^E + i(2n+D-a-2)\Gamma^C} \,,
\end{aligned} \tag{6.23}$$

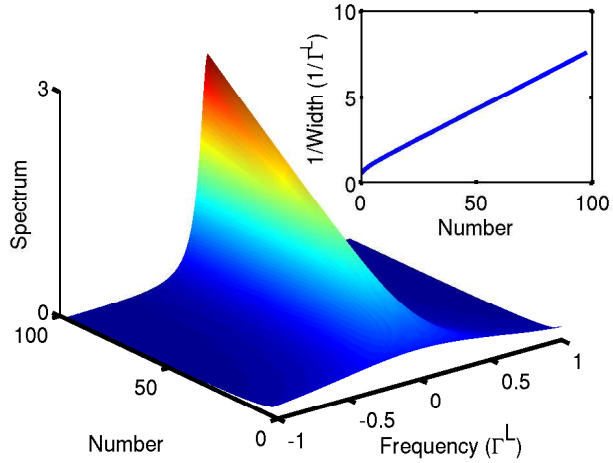

Figure 6.3: The spectrum is presented with vanishing collision rates. As the photon number is increased, the spectral width narrows. In the inset, the inverse of the spectral width is proportional to average photon number as expected from the Schawlow-Townes linewidth.

where $C_{n,a} \equiv C_{n,a(D-a)00}$ and initial condition $C_{n,a}(0) = \sqrt{n}P_{n,a}(0)$. With this terminology,

$$\langle \hat{a}_0^\dagger(t)\hat{a}_0(0) = \sum_{a=0}^{D} \frac{2^{D-a-1}(D-1)!}{a!(D-a-1)!} C_{n,a}(t)\,, \tag{6.24}$$

which deals with the multiple number of basis states that correspond to the same computational basis state. Note that collisional terms, with prefactor Γ^C, and evaporation terms, with prefactor Γ^E, are now present, contrary to the equations of motion for the populations.

There are two driving forces of decoherence, incoherent transfer through the mirrors and phase dispersion due to collisions, which both limit coherence time. The decoherence due to transfer through the mirrors can be examined by setting a vanishing collision rate. Due to bosonic amplification, the photons are able to support a state with a spectral width much narrower than that given by the linewidth of the photon decay.

Figure 6.3 presents the spectrum for vanishing collision rates for systems with 20 pumped plaquettes and different average photon numbers. As the photon number is

increased due to a higher pumping rate, the spectral width decreases due to Bosonic amplification. The spectral width can be much narrower than the width associated with the decay rate through the mirrors. As shown in the inset of Fig. 6.3, the spectral width, defined as half width at half maximum, is inversely proportional to the average photon number as expected by the Schawlow-Townes linewidth [148].

The effects of non-vanishing collision rates are of course an important aspect of the system. Figure 6.4 presents the fluctuation spectrum for a system with an average of 100 photons as the collision rate is increased. There is a mean-field interaction energy shift of the frequency since the energy of the photons is no longer just the bare mode energy. The spectral width rapidly grows as the collision rate becomes larger. One possible way to remedy this problem is to create a system that has a small collision rate for the low energy photons but still possesses a large recombination rate for the high energy photons. Such a system can be manufactured by creating a spatially dependent nonlinear medium. The low energy photons are more localized to the center of the cavity than the high energy photons. Therefore, if the medium is less dense in the center of the trap than toward the edges, the cavity will allow for fast recombinations of high energy photons to promote rapid evaporative cooling but small collision rates for low energy photons to promote coherent evolution.

6.4 Summary and Outlook

In this chapter, we examined the application of evaporative cooling to a photon fluid trapped in a Fabry-Perot cavity. The evaporation occurs due to an energy dependent reflectivity of the cavity mirrors. The presence of atom-mediated photon-photon interactions creates a situation in which rethermalization can occur. The amplification of the lowest energy mode due to stimulated emission can create a coherent system, even though the cavity is pumped with an incoherent source.

The condensation of a photon fluid using evaporative cooling provides a new

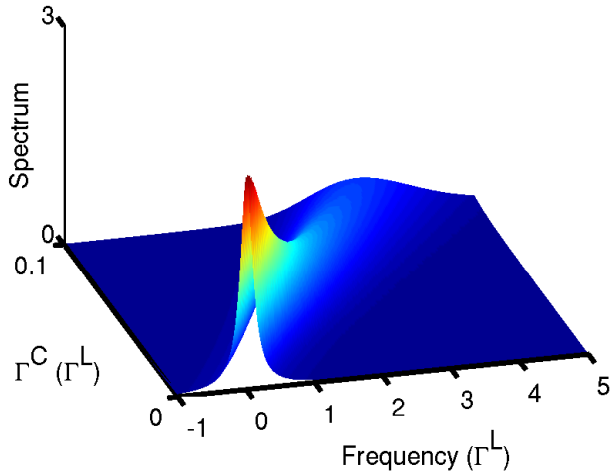

Figure 6.4: The spectrum is presented for systems with different collision rates. Larger the collision rates lead to wider spectra. The spectrum is also increased from the bare mode energy due to mean-field interaction shifts.

mechanism for creating a high-intensity narrow-spectrum coherent beam of light. Unlike a laser, the photon fluid, due to the presence of interactions, is expected to be superfluid and should possess for example classic properties such as phase rigidity and the ability to support quantized vortices. The key to the evaporative cooling mechanism in a photon fluid is that the population of the lowest energy mode be due to the stimulated emission from higher modes. The photon number distribution of the lowest energy mode then becomes Poissonian instead of exponentially decaying, a signature of a transition from a thermal to a coherent field. The spectrum of the photons also points towards a long coherence time. The width of the spectrum narrows as the inverse of the photon population as expected from the Schawlow-Townes linewidth.

Future work includes examining larger systems and models that more completely describe experimental systems. The specific energy structure of the cavity modes can alter the precise coherence times. After creating a condensed photon fluid, it would be instructive to examine the many superfluid properties that it should possess.

Appendix A

Jacobian Elliptic Functions

A brief review of the Jacobian elliptic functions [1, 113] is given. Of the 12 elliptic functions, there are only six that are normalizable. Of these six, only three represent a different physical form, *sn*, *cn* and *dn*. However, they are still related by,

$$\mathrm{cn}^2(x,k) = 1-\mathrm{sn}^2(x,k)\,, \tag{A.1}$$

$$\mathrm{dn}^2(x,k) = 1-k^2\,\mathrm{sn}^2(x,k)\,, \tag{A.2}$$

where k is the elliptic modulus. The six non-normalizable elliptic functions can also be reduced through a phase shift to three with different forms, *ns*, *ds*, and *cs*, which are also related by,

$$\mathrm{cs}^2(x,k) = \mathrm{ns}^2(x,k)-1\,, \tag{A.3}$$

$$\mathrm{ds}^2(x,k) = \mathrm{ns}^2(x,k)-k^2\,. \tag{A.4}$$

The normalizable and nonnormalizable functions can be related through

$$\mathrm{sn}^2(iK(1-k^2)+x,k) = k^2\ \mathrm{ns}^2(x,k)\,, \tag{A.5}$$

where $K(x)$ is the complete elliptic integral of the first kind. Therefore, the square of any elliptic function can be related linearly to $sn^2(x,k)$.

In the limit that $k \to 0$, the Jacobi elliptic functions approach the traditional trigonometric functions. The *sn* function becomes the sine function. The *cn* function

approaches the cosine function. The dn function approaches unity. As $k \to 1$, the Jacobi elliptic functions become the hyperbolic functions. sn becomes the hyperbolic tangent function. Both the cn and dn functions approach the hyperbolic secant function. The period of these functions, as given by $4K(k)$, goes from 2π to infinity as k goes from zero to one.

Appendix B

Completeness of Constant Potential Solution Set

It is possible to prove that Eq. (3.9) is a Jacobian elliptic integral of the first kind and can therefore be inverted to produce the Jacobian elliptic functions. If arbitrary parameters are used, Eq. (3.9) becomes,

$$\int \frac{1}{\sqrt{A_3\rho^3 + A_2\rho^2 + A_1\rho + A_0}}\,\mathrm{d}\rho = x + x_0\,, \tag{B.1}$$

where the A_i's are real constants. The cubic polynomial can be factored to give,

$$\int \frac{1}{\sqrt{(\rho + B_1)(\rho + B_2)(\rho + B_3)}}\,\mathrm{d}\rho = x + x_0\,, \tag{B.2}$$

where at least one of the constants B_i must be real. Without loss of generality we may take the real constant as B_1. The substitution $\rho = y^2 - B_1$ is then made in Eq. (B.2) to yield

$$\int \frac{2}{\sqrt{(y^2 + (B_2 - B_1))(y^2 + (B_3 - B_1))}}\,\mathrm{d}y = x + x_0\,. \tag{B.3}$$

This is the general form of the elliptic integral of the first kind [1] and therefore gives

$$C_1\mathrm{el}^{-1}(C_2 y, C_3) = x + x_0\,, \tag{B.4}$$

where the C_i's are constants and el is one of the twelve elliptic functions. This can be inverted and ρ replaced to produce

$$\sqrt{\rho + B_1} = C_2^{-1}\mathrm{el}(C_1^{-1}(x + x_0), C_3)\,, \tag{B.5}$$

or finally,

$$\rho = C_2^{-2}\mathrm{el}^2(C_1^{-1}(x + x_0), C_3) - B_1\,. \tag{B.6}$$

Since the square of any elliptic function can be related linearly to the square of sn, only one independent solution of the form

$$\rho = A\,\mathrm{sn}^2(bx + x_0, k) + B\,, \tag{B.7}$$

need be considered.

Appendix C

Atomtronics Calculational Details

In the following, we discuss the calculation of the current-voltage characteristics presented in Figs. 4.6, 4.9 and 4.11. The role of the system size is considered in section C.1. The results of this discussion justify the use of small systems in the calculation of the current response to a given voltage. Our approach is developed in sections C.2, C.3 and C.4. These three sections discuss the effect of the battery on the system, the character of the resulting current carrying state and the way these two aspects are used as a starting-point in formulating our method to calculate the current-voltage characteristics. The details of the algorithm used for wires and diodes are laid out in section C.5. Finally, the calculation for the transistor is discussed in C.6.

C.1 Small System Considerations

There are three primary concerns about the system size when performing calculations with a small lattices: effects on the phase diagram, effects at the boundary between two phases and effects on the current. All of these effects we find to be small.

Although phase diagrams of ultracold bosons in lattices, strictly speaking, refer to infinite systems, it is possible to describe phase diagrams for much smaller systems in a similar manner. For example, phase diagrams can be created for systems that are only four or six sites large. For a small system, the Mott insulator phase can be defined as a state with an integer filling of the lattice. The superfluid phase is defined

by a state with noninteger filling of the lattice. Note that adding an extra atom to a small system does require slightly more energy than adding an extra atom to an infinite system because in a large system the atom can distribute itself among more sites than for a small system. This, however, does not appreciably affect the characteristics of the different phases. The phase diagrams for small systems are similar to that presented for an infinite system in Fig. 4.2. The tip of the lobe is moved only slightly and the width of the superfluid region, where the lattice has non-integer filling and number fluctuations are large, only changes from $2J$ for a system of only two sites to $4J$ for an infinite lattice. The width of the superfluid region is already $3.2J$ for six sites. In addition, the number fluctuations characteristic of superfluid and insulating phase do not depend on the system size and only vary on the order of a few percent between small and large systems of the same filling. Similarly, the doped phase diagrams presented in Fig. 4.5 do not change considerably when calculated for small systems. The phase diagrams of these systems all possess the same qualitative feature that the insulating zone of the N-type doped lattice is pushed downwards while the insulating zone of the P-type doped lattice is pushed upwards. In conclusion, we find that small systems can be used to replicate the infinite lattice relations $\mu(n)$ plotted in Figs. 4.2 and 4.5.

Adjoining P-type and N-type materials creates a junction at which boundary effects could alter each component. However, we have found that the boundary only minimally affects one to two sites of each component in the limit $U \gg J$. We have examined the ground state of a PN configuration that extends over 20 lattice sites and compared each side with P-type and N-type materials in the absence of a junction. The difference in the occupation numbers and their fluctuations between the two systems is on the order of a few percent for the first site at the junction and is down to a tenth of a percent by the third site. In conclusion, using the expression $\mu(n)$ of P-type and N-type materials to describe each side of a PN-junction individually in a small system is justified because boundary effects due to the interface between the two materials are

small.

Finally, the third reason why small systems can be used to model larger systems is that the net current is not significantly affected by the size of the system. We have verified this numerically by comparing the exact dynamical evolution in one-dimensional lattices of between two and ten sites at constant filling with periodic boundary conditions. In the initial state, the density is modulated with period $2d$ and there is a constant phase difference between neighboring sites. This initial state is an example of the kind of running wave that would be created by a battery (as will be discussed below). The evolution of this state with the Hamiltonian Eq. (4.1) within the two-state approximation yields a net current that does not significantly depend on the number of lattice sites. This property is reminiscent of the current carried by a Bloch state which is independent of the system size at fixed quasi-momentum. A good estimate of the current response can therefore be obtained by considering a very small number of links. In this way, it is possible to circumvent calculating the dynamics of a large lattice. Note that even within the two-state approximation such a dynamical calculation is feasible only for systems with a small number of sites.

C.2 Battery Contacts

To power a circuit, the system is connected to an atomtronic battery by bringing two reservoirs of different chemical potential μ_L and μ_R into contact with the two ends of the lattice. The values of μ_L and μ_R determine the particle transfer Δn which is injected through one contact and removed through the other. The transfer Δn follows from the relations $\mu_L(n + \Delta n)$ and $\mu_R(n - \Delta n)$ with n the filling of the system at zero voltage. Note, the chemical potentials μ_L and μ_R should be chosen appropriately to ensure that the average filling is kept at n.

The net current obtained by applying a voltage is given by the average number of particles passing through the system per unit time after a transient time has passed.

The net current not only depends on the particle transfer Δn as determined by the values of μ, μ_L and μ_R, but also on the strength of the coupling between battery and system. The latter is set by the properties of the battery contact and determines the rate at which transfers of magnitude Δn take place.

C.3 Maximum current solution

The maximum current is obtained when subsequent transfers of the battery are separated by the time it takes for one transfer of Δn to free up the site to which the battery is connected. Such a situation is achieved for transfer rates that are close to $J/\hbar$. This is the regime we focus on. It yields the largest currents and reveals the limits on the currents that are due to the properties of the material rather than due to the properties of the battery contact.

The state reached after a time of transient behavior takes the form of a running density wave. The maxima (minima) of the wave take the value $n + \Delta n$ ($n - \Delta n$) and, hence, the wave amplitude depends on the voltage. The wavelength is given by twice the lattice period at maximum current. Note that in the limit of small voltages, the wave created by the contact with the battery can be described by the elementary excitations of the gas.

C.4 Current Response Calculation

The computation of the full dynamics of a realistic system would require a simulation of a large lattice interacting with several reservoirs, one at each battery contact. Instead, we use a simplified small-system approach. This approach does not allow us to describe the transient behavior. We expect the duration of the transient to be set by the time it takes for the particle transfer Δn from the battery to traverse the $(M-1)$ links of a lattice with M sites. Hence, the transient should occur on the time scale of $(M-1)(\hbar/J)$.

Our calculation of the current response is performed in several steps. First, the chemical potentials of the left and right batteries are chosen. These chemical potentials correspond to a average site filling. For a wire or a diode, a two well system is analyzed corresponding a junction in the system. An initial state of N_L atoms on the left and N_R atoms on the right, as determined by the chemical potentials and Eq. (4.2), is set with a phase corresponding to the lowest energy state with this density configuration. The state is propagated in time. The calculated current is determined by the time average current during half of an oscillation. This calculation corresponds to the current of a traveling wave with min and max densities of N_L and N_R.

C.5 Atomtronic Wires and Diodes

As discussed above in C.1, currents can be calculated by considering small systems. As a consequence, for a simple atomtronic wire the second step of the calculation, i.e. the calculation of the net current carried by a wave of amplitude Δn and wavelength $2d$, can be carried out by considering a single link.

In an atomtronic diode, it is the interface region rather than the bulk P-type or N-type material that poses the biggest obstacle for atom flow and thus determines the net current. The current calculation can be reduced down to just this single interface link since the evolution is little affected by adding further surrounding sites.

For a given transfer from the battery Δn, the current response of a single link is calculated using an initial state with $n_R = n+\Delta n$ particles on the right and $n_L = n-\Delta n$ particles on the left. The initial phase relation between the two sites is chosen so as to produce the lowest energy configuration that has the given filling on each site. We then compute the dynamical evolution yielding the time-dependent current $i(t)$. The net current I is obtained by calculating the time average of $i(t)$ over the time interval Δt and maximizing it with respect to Δt. With ν the frequency of the density oscillation, the time it takes for $2\Delta n$ particles to move from the initially higher populated site to

its neighbor is given by $1/2\nu$. Hence, the result for the net current is approximately given by $I = 4\Delta n\nu$.

To calculate the currents through an atomtronic wire (see Sec. 4.3) we consider a single link in the absence of additional external potentials with an equilibrium occupation $1 < n < 2$. The evolution of the two site system yields the time-dependent current

$$i(t) = \frac{2J}{\hbar}(n_R - n_L)\ \sin(4Jt/\hbar)\,. \tag{C.1}$$

To obtain the net current we maximize the time average of Eq. (C.1) over a time interval Δt. This yields

$$I = 1.45\frac{J}{\hbar}(n_R - n_L) \tag{C.2}$$

with $\Delta t = 0.58\hbar/J$. This result is close to the value $I = 4\Delta n\nu$ with the Rabi frequency $\nu = 2J/\hbar\pi$. From the result for the relation $I(\Delta n)$ we obtain the current-voltage dependence $I(\Delta\mu)$ using Eq. (4.2) for an infinite lattice.

The current characteristics of a diode (see section 4.4) is calculated in the same way with a potential step included between the two lattice sites. This potential step ensures that the two sides have the desired difference in occupation at equilibrium. In this configuration, the calculation yields a slightly more complicated current relation.

C.6 Transistor

The calculation for the transistor are performed in a similar way as that for a wire or a diode. Similar to the case of the diode, the current response to particle transfer from the battery is determined by the atom flux through the two interfaces between emitter/base and base/collector. Moreover, as discussed earlier, the current response has a small dependence on the number of links. Therefore, the current can be calculated by considering a three-site system, the two links representing the two links at the two interfaces of the NPN system. An external potential is added to raise the middle site

playing the role of the base while the outer sites represent the emitter and collector.

The initial state is prepared as the lowest energy state with n_E atoms in the emitter and $n_C = 1.5$ atoms in the collector. The filling on the base is determined from the height of the potential on the base and the condition of being in the lowest energy state with fillings n_E and n_C on the emitter and collector. At equilibrium, the base is occupied by $n_B = 1.005$ atoms. The current of atoms passing through the base from collector to emitter is given by $i_C = (i_{CB} + i_{BE})/2$ with i_{CB} the current from collector to base and i_{BE} the current from base to emitter. As in the previous sections, we calculate the net collector current I_C by maximizing the time average of i_C. Since we are interested in the μ_E-dependence of I_C at fixed V_{BC}, the initial collector occupation is kept fixed at $n_C = 1.5$ while the emitter occupation n_E is varied in the range $1 \leq n_E < 1.5$.

The base current is set to be $I_B = \Gamma(n_B - 1)$, where Γ must satisfy the condition $\Gamma \ll J/\hbar$. The quantity Γ describes the weak coupling with the battery at the base contact which is due to the thinness of the base. The data for I_B displayed in Fig. 4.11(b) is obtained using $\Gamma = 0.01J/\hbar$. The number of current carriers involved in I_B is given by $(n_B - 1)$ because the chemical potential of the base contact is set to be in the $n = 1$ insulator region. Note that our calculation neglects the effect of I_B on I_C. This is justified because the weak coupling at the base contact implies that the reduction of n_B by I_B is small. Overall, the transistor current gain relies on two factors. The base region must be thin and the emitter must have an equilibrium filling significantly larger than the base.

Bibliography

[1] M. Abramowitz and I. A. Stegun, editors. Handbook of Mathematical Functions. National Bureau of Standards, Washington, D.C., 1964.

[2] S. A. Alexander and R. L. Coldwell. Solution of the kronig-penney model using variational monte carlo. Int. J. Quantum Chem., 86(4):325, Feb. 2002.

[3] J. F. Allen and A. D. Misner. Flow of liquid helium ii. Nature, 141:75, 1938.

[4] S. L. Altmann. Band Theory of Metals: The Elements. Pergamon PRess, Oxford, 1970.

[5] B. P. Anderson and M. A. Kasevich. Macroscopic quantum interference from atomic tunnel arrays. Science, 282(5394):1686–1689, 1998.

[6] M. H. Anderson, J. R. Ensher, M. R. Matthews, C. E. Wieman, and E. A. Cornell. Observation of bose-einstein condensation in a dilute atomic vapor. Science, 269:198, July 1995.

[7] T. Anker, M. Albiez, B. Eiermann, M. Taglieber, and M. K. Oberthaler. Linear and nonlinear dynamics of matter wave packets in periodic potentials. Opt. Express, 12(1):11, Jan. 2004.

[8] P. D. Ankrum, editor. Semiconductor Electronics. Prentice-Hall, Englewood-Cliffs, N.J., 1971.

[9] N. W. Ashcroft and N. D. Mermin. Solid State Physics. W. B. Saunders Company, 1976.

[10] G. E. Astrakharchik and L. P. Pitaevskii. Motion of a heavy impurity through a bose-einstein condensate. Phys. Rev. A, 70:013608, July 2004.

[11] R. Balili, V. Hartwell, D. Snoke, L. Pfeiffer, and K. West. Bose-einstein condensation of microcavity polaritons in a trap. Science, 326:1007, 2007.

[12] R. Bhat, M. Holland, and L. Carr. Bose-Einstein Condensates in Rotating Lattices. Physical Review Letters, 96(6):60405, 2006.

[13] R. Bhat, B. Peden, B. Seaman, M. Krämer, L. Carr, and M. Holland. Quantized vortex states of strongly interacting bosons in a rotating optical lattice. Physical Review A, 74(6):63606, 2006.

[14] M. M. Bogdan, A. S. Kovalev, and I. V. Gerasimchuk. Dynamics and stability of localized modes in nonlinear media with point defects. Low Temp. Phys., 23(2):145–152, Feb. 1997.

[15] K. Bongs and K. Sengstock. Physics with coherent matter waves. Reports on Progress in Physics, 67(6):907–963, 2004.

[16] S. N. Bose. Plancks gesetz und lichtquantenhypothese. Z. Phys., 26:178, 1924.

[17] F. Bowman. Introduction to Elliptic Functions, with Applications. Dover, New York, 1961.

[18] C. C. Bradley, C. A. Sackett, and R. G. Hulet. Analysis of in situ images of bose-einstein condensates of lithium. Phys. Rev. A, 55:3951, 1997.

[19] C. C. Bradley, C. A. Scakett, J. J. Tollett, and R. G. Hulet. Evidence of bose-einstein condensation in an atomic gs with attractive interactions. Phys. Rev. Lett., 75(9):1687–1690, Aug 1995.

[20] G. Brennen, C. Caves, P. Jessen, and I. Deutsch. Quantum Logic Gates in Optical Lattices. Physical Review Letters, 82(5):1060–1063, 1999.

[21] H. Briegel, T. Calarco, D. Jaksch, J. Cirac, and P. Zoller. Quantum computing with neutral atoms. Journal of Modern Optics, 47(2-3):415–451, 2000.

[22] J. C. Bronski, L. D. Carr, R. Carretero-González, B. Deconinck, J. N. Kutz, and K. Promislow. Stability of attractive bose-einstein condensates in a periodic potential. Phys. Rev. E, 64:056615–1–9, 2001.

[23] J. C. Bronski, L. D. Carr, B. Deconinck, and J. N. Kutz. Bose-einstein condensates in standing waves: The cubic nonlinear schrodinger equation with a periodic potential. Phys. Rev. Lett., 86(8):1402, Feb. 2001.

[24] J. C. Bronski, L. D. Carr, B. Deconinck, J. N. Kutz, and K. Promislow. Stability of repulsive bose-einstein condensates in a periodic potential. Phys. Rev. E, 63:036612, Feb. 2001.

[25] P. Capuzzi and E. S. Hernandez. ^{3}he impurity in a bose-einstein condensate. Phys. Rev. S, 62:023603, 2000.

[26] L. D. Carr, C. W. Clark, and W. P. Reinhardt. Stationary solutions of the one-dimensional nonlinear schrodinger equation. i. case of repulsive nonlinearity. Phys. Rev. A, 62:063610, December 2000.

[27] L. D. Carr, C. W. Clark, and W. P. Reinhardt. Stationary solutions of the one-dimensional nonlinear schrodinger equation. ii. case of attractive nonlinearity. Phys. Rev. A, 62:063611, December 2000.

[28] L. D. Carr, J. N. Kutz, and W. P. Reinhardt. Stability of stationary states in the cubic nonlinear schrdinger equation: Applications to the bose-einstein condensate. Phys. Rev. E, 63:066604, May 2001.

[29] L. D. Carr, M. A. Leung, and W. P. Reinhardt. Dynamics of the bose-einstein condensate: quasi-one-dimension and beyond. J. Phys. B, 33:3983, 2000.

[30] L. D. Carr, K. W. Mahmud, and W. P. Reinhardt. Tunable tunneling: An application of stationary states of bose-einstein condensates in traps of finit depth. Phys. Rev. A, 64:033603–1–9, 2001.

[31] F. Cataliotti, S. Burger, C. Fort, P. Maddaloni, F. Miardi, A. Trombettoni, A. Smerzi, and M. Inguscio. Josephson junction arrays with bose-einstein condensates. Science, 293(5531):842, 2001.

[32] R. M. Cavalcanti, P. Giacconi, G. Pupillo, and R. Soldati. Bose-einstein condensation in the presence of a uniform field and a pointlike impurity. Phys. Rev. A, 65:053606, 2002.

[33] R. Y. Chiao and J. Boyce. Bogoliubov dispersion relation and the possibility of superfluidity for weakly interacting photons in a two-dimensional photon fluid. Phys. Rev. A, 60(5):4114–4121, November 1999.

[34] A. P. Chikkatur, A. Gorlitz, D. M. Stamper-Kurn, S. Inouye, S. Gupta, and W. Ketterle. Suppression and enhancement of impurity scattering in a bose-einstein condensate. Phys. Rev. Let., 85(3):483, 2000.

[35] D. N. Christodoulides, F. Lederer, and Y. Silberberg. Discretizing light behavior in linear and nonlinear waveguide lattices. Nature (London), 424(6950):817, August 2003.

[36] C. Conti, M. Peccianti, and G. Assanto. Route to nonlocality and observation of accessible solitons. Phys. Rev. Let., 91(7):073901, 2003.

[37] A. Daley, S. Clark, D. Jaksch, and P. Zoller. Numerical analysis of coherent many-body currents in a single atom transistor. Physical Review A, 72(4):43618, 2005.

[38] F. Dalfovo, S. Giorgini, L. P. Pitaevskii, and S. Stringari. Theory of bose-einstein condensation in trapped gases. Rev. Mod. Phys., 71:463, April 1999.

[39] K. B. Davis, M. O. Mewes, M. R. Andrews, N. J. Vandruten, D. S. Durfee, D. M. Kurn, and W. Ketterle. Bose-einstein condensation in a gas of sodium atoms. Phys. Rev. Lett., 75(22):3969–3973, Nov. 1995.

[40] B. Deconinck, B. A. Frigyik, and J. N. Kutz. Dynamics and stability of bose-einstein condensates: The nonlinear schrodinger equation with periodic potential. J. Nonlinear Sci., 12:169–205, 2002.

[41] J. Denschlag, J. Simsarian, H. Haeffner, C. McKenzie, A. Browaeys, D. Cho, K. Helmerson, S. Rolston, and W. Phillips. A bose-einstein condensate in an optical lattice. Journal of Physics B Atomic Molecular and Optical Physics, 35(14):3095–3110, 2002.

[42] L. DeSarlo, L. Fallani, J. E. Lye, M. Modugno, R. Saers, C. Fort, and M. Inguscio. Unstable regimes for a bose-einstein condensate in an optical lattice. e-print cond-mat/0412279v1, 2004.

[43] D. Diakonov, L. M. Jensen, C. J. Pethick, and H. Smith. Loop structure of the lowest bloch band for a bose-einstein condensate. Phys. Rev. A, 66:013604, 2002.

[44] E. A. Donley, N. R. Claussen, S. T. Thompson, and C. E. Wieman. Atom-molecule coherence in a bose-einstein condensate. Nature, 417:529, 2002.

[45] B. Eiermann, T. Anker, M. Albiez, M. Taglieber, P. Treutlein, K. P. Marzlin, and M. K. Oberthaler. Bright bose-einstein gap solitons of atoms with repulsive interaction. Phys. Rev. A, 92(23):230401, 2004.

[46] B. Eiermann, P. Treutlein, T. Anker, M. Albiez, M. Taglieber, K.-P. Marzlin, and M. K. Oberthaler. Dispersion management for atomic matter waves. Phys. Rev. Lett., 91(6):060402, 2003.

[47] A. Einstein. Quantentheorie des einatomigen idealen gases. Sitzungsber. Kgl. Preuss. Akad. Wiss., page 261, 1924.

[48] T. Esslinger and K. Molmer. Atoms and molecules in lattices: Bose-einsten condensates built on a shared vacuum. Phys. Rev. Lett., 90(16):160406, Apr. 2003.

[49] L. Fallani, F. S. Cataliotti, J. Catani, C. Fort, M. Modugno, M. Zawada, and M. Inguscio. Optically induced lensing effect on a bose-einstein condensate expanding in a moving lattice. Phys. Rev. Lett., 91(24):240205, Dec. 2003.

[50] L. Fallani, L. De Sarlo, J. E. Lye, M. Modugno, R. Saers, S. Fort, and M. Inguscio. Observation of dynamical instability for a bose-einstein condensate in a moving 1d optical lattice. Phys. Rev. Lett., 93(14):140406, Oct. 2004.

[51] J. Felber, R. Gahler, and C. Rausch. Matter waves at a vibrating surface: Transition from quantum-mechanical to classical behavior. Phys. Rev. A, 53(1):319, 1996.

[52] M. P. A. Fisher, P. B. Weichman, G. Grinstein, and D. S. Fisher. Boson localization and the superfluid-insulator transition. Phys. Rev. B, 40:546–570, 1989.

[53] R. Folman, P. Kruger, J. Schmiedmayer, J. Denschlag, and C. Henkel. Microscopic atom optics: From wires to an atom chip. Adv. At. Mol. Opt. Phys, 48:263, 2002.

[54] C. Fort, F. Cataliotti, J. Catani, L. De Sarlo, L. Fallani, J. Lye, M. Modugno, R. Saers, and M. Inguscio. Dynamics of bloch matter waves and its breakdown: a bose–einstein condensate in a moving 1d optical lattice. Laser Physics, 15(3):447–453, 2005.

[55] Y. B. Gaididei, P. L. Christiansen, K. O. Rasmussen, and M. Johansson. Two-dimensional effects in nonlinear kronig-penney models. Phys. Rev. B, 55(20):55, May 1997.

[56] H. Gimperlein, S. Wessel, J. Schmiedmayer, and L. Santos. Ultracold atoms in optical lattices with random on-site interactions. Phys Rev Lett, 95(17):170401, 2005.

[57] M. Girardeau. Relationship between systems of impenetrable bosons and fermions in one dimension. J. Math. Phys., 1:516, 1960.

[58] R. J. Glauber. Coherent and incoherent states of the radiation field. Phys. Rev., 131(6):2766–2788, September 1963.

[59] R. J. Glauber. The quantum theory of optical coherence. Phys. Rev., 130(6):2529–2539, June 1963.

[60] J. P. Gordon. Interaction forces among solitons in optical fibers. Opt. Lett., 8:596–598, 1983.

[61] J. P. Gordon and H. A. Haus. Random walk of coherently amplified solitons in optical fiber transmission. Opt. Lett., 11:665–667, 1986.

[62] M. Greiner, I. Bloch, O. Mandel, T. Hänsch, and T. Esslinger. Exploring phase coherence in a 2d lattice of bose-einstein condensates. Phys. Rev. Lett., 87(16):160405, 2001.

[63] M. Greiner, I. Bloch, O. Mandel, T. W. Hansch, and T. Esslinger. Bose-einstein condensates in 1d and 2d optical lattices. Appl. Phys. B, 73, 2001.

[64] M. Greiner, O. Mandel, T. Esslinger, T. W. Hansch, and I. Bloch. Quantum phase transition from a superfluid to a mott insulator in an ultracold gas of atoms. Nature, 415:39, Jan. 2002.

[65] E. P. Gross. Structure of a quantized vortex in boson systems. Nuovo Cimento, 20:454, 1961.

[66] G. Grynberg, B. Lounis, P. Vererk, J. Y. Courtois, and C. Salomon. Quantized motion of cold cesium atoms in two- and three-dimensional optical potentials. Phys. Rev. Lett., 70:2249, 1993.

[67] G. Grynberg and C. Robilliard. Cold atoms in dissipative optical lattices. Physics Reports, 355(5):335–451, 2001.

[68] L. Guidoni, C. Triche, P. Verkerk, and G. Grynberg. Quasiperiodic optical lattices. Phys. Rev. Lett., 79(18):3363–3366, Nov 3 1997.

[69] Z. Hadzibabic, P. Kruger, M. Cheneau, B. Battelier, and J. Dalibard. Berezinskii-kosterlitz-thouless crossover in a trapped atomic gas. Nature, 441:1118–1121, June 2006.

[70] E. W. Hagley, L. Deng, M. Kozuma, J. Wen, K. Helmerson, S. L. Rolston, and W. D. Phillips. A well-collimated quasi-continuous atom laser. Science, 238(5408):1706–1709, Mar 1999.

[71] V. Hakim. Nonlinear schrodinger flow past an obstacle in one dimenstion. Phys. Rev. E, 55(3):2835, March 1997.

[72] J. Harms and J. P. Toennies. Experimental evidence for the transmission of 3he atoms through superfluid 4he droplets. Phys. Rev. Let., 83(2):344, 1998.

[73] H. Hasimoto and H. Ono. Nonlinear modulation of gravity waves. J. Phys. Sco. Jpn, 33:805, 1972.

[74] H. Haus and W. S. Wong. Solitons in optical communications. Rev. Mod. Phys., 68:423–444, 1996.

[75] A. Hemmerich and T. W. Hänsch. Two-dimesional atomic crystal bound by light. Phys. Rev. Lett., 70:410, 1993.

[76] K. M. Hilligsoe, M. K. Oberthaer, and K.-P. Marzlin. Stability of gap solitons in a bose-einstein condensate. Phys. Rev. A, 66:063605, Dec. 2002.

[77] M. Holland, K. Burnett, C. Gardiner, J. I. Cirac, and P. Koller. Theory of an atom laser. Phys. Rev. A, 54(3):R1757, September 1996.

[78] P. Horak, J. Courtois, and G. Grynberg. Atom cooling and trapping by disorder. Physical Review A, 58(5):3953–3962, 1998.

[79] E. Infeld and G. Rowlands. On the stability of electron plasma waves. J. Phys. A, 12(11):2255–2262, 1979.

[80] E. Infeld and G. Rowlands. Nonlinear Waves, Solitons and Chaos. Cambridge University Press, United Kingdom, 2nd edition, 2000.

[81] A. Inouye, M. R. Andrews, J. Stenger, H.-J. Miesner, D. M. Stamper-Kurn, and W. Ketterle. Observation of feshbach resonances in a bose-einstein condensate. Nature, 392:151, March 1998.

[82] D. Jacksch, A. Brude, J. I. Cirac, C. W. Gardiner, and P. Zoller. Cold bosonic atoms in optical lattices. Phys. Rev. Lett., 81(15):3108, Oct. 1998.

[83] J. D. Jackson. Classical Electrodynamics. Wiley, New York, 1999.

[84] R. Jackson and M. Weinstein. Geometric Analysis of Bifurcation and Symmetry Breaking in a GrossPitaevskii Equation. Journal of Statistical Physics, 116(1):881–905, 2004.

[85] D. Jaksch, C. Bruder, J. I. Cirac, C. W. Gardiner, and P. Zoller. Cold bosonic atoms in optical lattices. Phys. Rev. Lett., 81(15):3108, Oct. 1998.

[86] P. Jordan and E. Wigner. Uber das PaulischeAquivalenzverbot. Z. Physik, 47:631–651, 1928.

[87] P. Kapitza. Viscosity of liquid helium below the λ-point. Nature, 141:74, 1938.

[88] G. Kavoulakis. Bose-Einstein condensates with attractive interactions on a ring. Physical Review A, 67(1):11601, 2003.

[89] P. G. Kevrekidis, R. Carretero-Gonzalez, G. Theocharis, D. J. Frantzeskakis, and B. A. Malomed. Stability of dark solitons in a bose-einstein condensate trapped in an optical lattice. Phys. Rev. A, 68:035602, 2003.

[90] H. Kimble, M. Dagenais, and L. Mandel. Photon Antibunching in Resonance Fluorescence. Physical Review Letters, 39(11):691–695, 1977.

[91] H. Kimble and L. Mandel. Theory of resonance fluorescence. Physical Review A, 13(6):2123–2144, 1976.

[92] Y. S. Kivshar. Soliton scattering by impurities in hydrogen-bonded chains. Phys. Rev. A, 43(6):3117, March 1991.

[93] Y. S. Kivshar, T. J. Alexander, and S. K. Turitsyn. Nonlinear modes of a macroscopic quantum oscillator. Phys. Lett. A, 278(4):225–230, 2001.

[94] Y. S. Kivshar, Z. Fei, and L. Luis Vzquez. Resonant soliton-impurity interactions. Phys. Rev. Lett., 67(10):1177, September 1991.

[95] Y. S. Kivshar and B. Luther-Davies. Dark optical solitons: Physics and applications. Physics Reports, 298:81–197, 1998.

[96] A. G. Klein, P. Prager, P. J. Wagenfeld, H.and Ellis, and T. M. Sabine. Diffraction of neutrons and x-rays by a vibrating quartz crystal. Appl. Phys. Lett., 10(10):294, 1967.

[97] M. Köhl, H. Moritz, T. Stöferle, K. Günter, and T. Esslinger. Fermionic atoms in a three dimensional optical lattice: Observing fermi surfaces, dynamics, and interactions. Physical Review Letters, 94(8):80403, 2005.

[98] W. Krauth, M. Caffarel, and J. Bouchaud. Gutzwiller wave function for a model of strongly interacting bosons. Physical Review B, 45(6):3137–3140, 1992.

[99] P. Leboeuf, N. Pavloff, and S. Sinha. Solitonic transmission of bose-einstein matter waves. Phys. Rev. A, 68:063608, Dec 2003.

[100] A. J. Leggett. Bose-einstein condensation in the alkali gases: Some fundamental concepts. Rev. Mod. Phys., 73(2):307, April 2001.

[101] G. Lenz, P. Meystre, and E. M. Wright. Nonlinear atom optics: General formalism and atomic solitons. Phys. Rev. A, 50(2):1681, 1994.

[102] W. Li and A. Smerzi. Nonlinear kronig-penney model. Phys. Rev. E, 70(1):016605, July 2004.

[103] F. London. The λ-phenomenon of liquid helium and the bose-einstein degeneracy. Nature, 141:643, 1938.

[104] P. J. Y. Louis, E. A. Ostrovskaya, and Y. S. Kivshar. Dispersion control for matter waves and gap solitons in optical superlattices. Phys. Rev. A, 71(2):023612, Feb 2005.

[105] P. J. Y. Louis, E. A. Ostrovskaya, M. Savage, Craig, and Y. S. Kivshar. Bose-einstein condensates in optical lattices: Band-gap structure and solitons. Phys. Rev. A, 67:013602, Jan. 2003.

[106] M. Machholm, A. Nicolin, C. J. PEthick, and H. Smith. Spatial period doubling in bose-einstein condensates in an optical lattice. Phys. Rev. A, 69:043604, 2004.

[107] M. Machholm, C. J. Pethick, and H. Smith. Band structure, elementary excitations, and stability of a bose-einstein condensate in a periodic potential. Phys. Rev. A, 67(5):053613, May 2003.

[108] P. Massignan and M. Modugno. One-dimensional model for the dynamics and expansion of elongated bose-einstein condensates. Phys. Rev. A, 67:023614, 2003.

[109] I. M. Merhasin, B. V. Gisin, R. Driben, and B. A. Malomed. Finite-band solitons in the kronig-penney model with the cubic-quintic nonlinearity. Phys. Rev. E, 71(1):016613, Jan 2005.

[110] P. Meystre and M. Sargent III. Elements of Quantum Optics. Springer, Berlin, 3rd edition, 1998.

[111] A. Micheli, A. Daley, D. Jaksch, and P. Zoller. Single Atom Transistor in a 1D Optical Lattice. Physical Review Letters, 93(14):140408, 2004.

[112] A. Micheli and P. Zoller. Single-atom mirror for one-dimensional atomic lattice gases. Physical Review A, 73(4):43613, 2006.

[113] L. M. Milne-Thomson. Jacobian Elliptic Function Tables. Dover Publications Inc., New York, 1950.

[114] G. Modugno, F. Ferlaino, R. Heidemann, G. Roati, and M. Inguscio. Production of a fermi gas of atoms in an optical lattice. Physical Review A, 68(1):11601, 2003.

[115] H. Moritz, T. Stöferle, M. Köhl, and T. Esslinger. Exciting collective oscillations in a trapped 1d gas. Phys. Rev. Lett., 91:250402, 2003.

[116] O. Morsch, J. Müller, M. Cristiani, D. Ciampini, and E. Arimondo. Bloch oscillations and mean-field effects of bose-einstein condensates in 1d optical lattices. Physical Review Letters, 87(14):140402, 2001.

[117] E. J. Mueller. Superfluidity and mean-field energy loops: Hysteric behavior in bose condensates. Phys. Rev. A, 66(6):063603, Dec 2002.

[118] J. G. Muga and M. Buttiker. Time dependence of evanescent quantum waves. Phys. Rev. A, 62:023808, 2000.

[119] M. Olshanii. Atomic scattering in the presence of an external confinement and a gas of impenetrable bosons. Phys. Rev. Lett., 81:938–941, 1998.

[120] E. A. Ostrovskaya and Y. S. Kivshar. Localization of two-component bose-einstein condensates in optical lattices. Phys. Rev. Lett., 92(18):180405, May 2004.

[121] Y. B. Ovchinnikov, J. H. Müller, M. R. Doery, E. J. D. Vredenbregt, K. Helmerson, S. L. Rolston, and W. D. Phillips. Diffraction of a released bose-einstein condensate by a pulsed standing light wave. Phys. Rev. Lett., 83(2):284, July 1999.

[122] N. Pavloff. Breakdown of superfluidity of an atom laser past an obstacle. Phys. Rev. A, 66:013610, July 2002.

[123] B. Peden, R. Bhat, M. Krämer, and M. Holland. Quasi-angular momentum of Bose and Fermi gases in rotating optical lattices. Journal of Physics B: Atomic, Molecular and Optical Physics, 40(18):3725–3744, 2007.

[124] S. Peil, J. V. Porto, B. L. Tolra, J. M. Obrecht, B. E. King, M. Subbotin, S. L. Rolston, and W. D. Phillips. Patterned loading of a bose-einstein condensate into an optical lattice. Phys. Rev. A, 67(5):051603, May 2003.

[125] R. Pepino, J. Cooper, D. Anderson, and M. Holland. Atomtronic circuits of diodes and transistors. cond-mat/0705.3268, 2007.

[126] L. Pezzè, L. Pitaevskii, A. Smerzi, S. Stringari, G. Modugno, E. de Mirandes, F. Ferlaino, H. Ott, G. Roati, and M. Inguscio. Insulating behavior of a trapped ideal fermi gas. Physical Review Letters, 93(12):120401, 2004.

[127] L. P. Pitaevskii. Vortex lines in an imperfect bose gas. Zh. Eksp. Teor. Fiz., 40:646, 1961.

[128] M. A. Porter and P. Cvitanovic. Modulated amplitude waves in bose-einstein condensates. Phys. Rev. E, 69(4):047201, Apr 2004.

[129] M. A. Porter, P. G. Kevrekidis, and B. A. Malomed. Resonant and non-resonant modulated amplitude waves for binary bose-einstein condensates in optical lattices. Physica D, 196:106–123, Sep. 2004.

[130] A. Radouani. Soliton and phonon production by an oscillating obstacle in a quasi-one-dimensional trapped repulsive bose-einstein condensate. Phys. Rev. A, 70:013602, July 2004.

[131] C. A. Regal, M. Greiner, and D. S. Jin. Observation of resonance condensation of fermionic atom pairs. Phys. Rev. Lett, 92:040403, 2004.

[132] J. Reichel. Microchip traps and Bose–Einstein condensation. Applied Physics B: Lasers and Optics, 74(6):469–487, 2002.

[133] A. M. Rey. Ultracold bosonic atoms in optical lattices. PhD thesis, University of Maryland at College Park, 2004.

[134] A. M. Rey, K. Burnett, R. Roth, M. Edwards, C. J. Williams, and C. W. Clark. Bogoliubov approach to superfluidity of atoms in an optical lattice. J. Phys. B, 36(5):825–841, Mar. 2003.

[135] G. Roati, E. de Mirandes, F. Ferlaino, H. Ott, G. Modugno, and M. Inguscio. Atom interferometry with trapped fermi gases. Physical Review Letters, 92(23):230402, 2004.

[136] J. L. Roberts, N. R. Claussen, J. P. Burke, Jr., C. H. Greene, E. A. Cornell, and C. E. Wieman. Resonant magnetic field control of elastic scattering in cold 85rb. Phys. Rev. Let., 81:5109, 1998.

[137] S. Rolston and W. Phillips. Nonlinear and quantum atom optics. Nature, 416(6877):219–224, 2002.

[138] R. Roth and K. Burnett. Phase diagram of bosonic atoms in two-color superlattices. Phys. Rev. A, 68(2):023604, Aug 2003.

[139] A. Ruschhaupt, F. Delgado, and J. Muga. Velocity selection of ultra-cold atoms with Fabry–Perot laser devices: improvements and limits. Journal of Physics B: Atomic, Molecular, and Optical Physics, 38(15):2665–2674, 2005.

[140] A. Ruschhaupt and J. Muga. Atom diode: A laser device for a unidirectional transmission of ground-state atoms. Physical Review A, 70(6):61604, 2004.

[141] A. Ruschhaupt and J. Muga. Adiabatic interpretation of a two-level atom diode, a laser device for unidirectional transmission of ground-state atoms. Physical Review A, 73(1):13608, 2006.

[142] A. Ruschhaupt, J. Muga, and M. Raizen. One-photon atomic cooling with an optical Maxwell demon valve. Journal of Physics B: Atomic, Molecular and Optical Physics, 39(18):3833–3838, 2006.

[143] S. Sachdev, editor. Quantum Phase Transitions. CAmbridge Univ. Press, 1999, Cambridge.

[144] J. Sacher, D. Baums, P. Panknin, W. Elsasser, and E. O. Gobel. Intensity instabilities of semiconductor-lasers under current modulation, external light injection, and delayed feedback. Phys. Rev. A, 45(3):1893–1905, Feb 1 1992.

[145] L. Salasnich, A. Parola, and L. Reatto. Effective wave equations for the dynamics of cigar-shaped and disk-shaped bose condensates. Phys. Rev. A, 65(4):043614, Apr 2002.

[146] L. Sanchez-Palencia and L. Santos. Bose-Einstein condensates in optical quasicrystal lattices. Physical Review A, 72(5):53607, 2005.

[147] L. Santos, M. Baranov, J. Cirac, H. Everts, H. Fehrmann, and M. Lewenstein. Atomic Quantum Gases in Kagomé Lattices. Physical Review Letters, 93(3):30601, 2004.

[148] A. L. Schawlow and C. H. Townes. Infared and opitcal masers. Phys. Rev., 112(6):1940–1949, Dec. 1958.

[149] T. Schulte, S. Drenkelforth, J. Kruse, W. Ertmer, J. Arlt, K. Sacha, J. Zakrzewski, and M. Lewenstein. Routes towards Anderson localization of Bose-Einstein condensates in disordered optical lattices. Phys. Rev. Lett., 95:170411, 2005.

[150] V. Schweikhard, S. Tung, and E. A. Cornell. Vortex proliferation in the berezinskii-kosterlitz-thouless regime on a two-dimensional lattice of bose-einstein condensates. Phys. Rev. Lett., 99:030401, 2007.

[151] M. M. Scott, Y. K. Fetisov, V. T. Synogach, and C. E. Patton. Suppression of microwave magnetic envelope solitons by continuous wave magnetostatic wave signals. J. Appl. Phys., 88:4232, 2000.

[152] B. T. Seaman, L. D. Carr, and M. J. Holland. Effect of a potential step or impurity on the bose-einstein condensate mean field. Phys. Rev. A, 71(3):033609, March 2005. cond-mat/0410345.

[153] B. T. Seaman, L. D. Carr, and M. J. Holland. Nonlinear band structure in bose einstein condensates: The nonlinear schrödinger equation with a kronig-penney potential. Phys. Rev. A, 71(3):033622, March 2005.

[154] B. T. Seaman, L. D. Carr, and M. J. Holland. Period doubling, two-color lattices, and the growth of swallowtails in bose-einstein condensates. Phys. Rev. A, 72(3):033602, March 2005.

[155] B. T. Seaman and M. J. Holland. Evaporative cooling of a photon fluid to quantum degeneracy. submitted to Phys. Rev. Lett., 2008. condmat.

[156] B. T. Seaman, M. Krämer, D. Z. Anderson, and M. J. Holland. Atomtronics: Ultracold-atom analogs of electronic devices. Phys. Rev. A, 75(2):023615, 2007.

[157] C. P. Search and P. Meystre. Nonlinear and quantum optics of atomic and molecular fields. PROGRESS IN OPTICS, 47:139, 2005.

[158] T. B. Simpson, J. M. Liu, A. Gavrielides, V. Kovanis, and P. M. Alsing. Period-doubling route to chaos in a semiconductor-laser subject to optical injection. Appl. Phys. Lett., 64(26):3539–3541, Jun 27 1994.

[159] R. E. Slusher, L. W. Hollberg, B. Yurke, J. C. Mertz, and J. F. Valley. Observation of squeezed states generated by four-wave mixing in an optical cavity. Phys. Rev. Lett, 55(22):2409–2412, November 1985.

[160] K. Stasiewicz, P. K. Shukla, G. Gustafsson, S. Buchert, B. Lavraud, B. Thide, and Z. Klos. Slow magnetosonic solitons detected by the cluster spacecraft. Phys. Rev. Let., 90(8):085002, 2003.

[161] A. Steane. Quantum computing. Reports on Progress in Physics, 61(2):117–173, 1998.

[162] J. Stickney, D. Anderson, and A. Zozulya. Transistorlike behavior of a Bose-Einstein condensate in a triple-well potential. Physical Review A, 75(1 B), 2007.

[163] T. Stöferle, H. Moritz, C. Schori, M. Köhl, and T. Esslinger. Transition from a Strongly Interacting 1D Superfluid to a Mott Insulator. Physical Review Letters, 92(13):130403, 2004.

[164] A. A. Sukhorukov and Y. S. Kivshar. Nonlinear localized waves in a periodic medium. Phys. Rev. E, 87(8):083901, Aug. 2001.

[165] A. A. Sukhorukov and Y. S. Kivshar. Spatial optical solitons in nonlinear photonic crystals. Phys. Rev. E, 65(3):036609, Mar. 2001.

[166] C. Sulem and P. L. Sulem. Nonlinear Schrödinger Equations: Self-focusing Instability and Wave Collapse. Springer-Verlag, New York, 1999.

[167] V. I. Talanov. Self-focusing of wave beams in nonlinear media. Zh. Eksp. Teor. Fiz., 2:31, 1965.

[168] D. Taras-Semchuk and J. M. F. Gunn. Superfluid flow past an array of scatterers. Phys. Rev. B, 60(18):13139, November 1999.

[169] E. Taylor and E. Zaremba. Bogoliubov sound speed in periodically modulated bose-einstein condensates. Phys. Rev. A, 68(5):053611, Nov. 2003.

[170] S. Theodorakis and E. Leontidis. Bound states in a nonlinear kronig-penney model. J. Phys. A, 30(13):4835–4849, July 1997.

[171] R. A. Usmanov and L. B. Ioffe. Theoretical investigation of a protected quantum bit in a small josephson junction array with tetrahedral symmetry. Phys. Rev. B, 69(21):214513, Jun 2004.

[172] J. Villavicencio, R. Romo, and S. S. y. Silva. Quantum-wave evolution in a step potential barrier. Phys. Rev. A, 66:042110, 2002.

[173] B. Wu, R. B. Diener, and Q. Niu. Bloch waves and bloch bands of bose-einstein condensates in optical lattices. Phys. Rev. A, 65:025601, 2002.

[174] B. Wu and Q. Niu. Nonlinear landua-zener tunneling. Phys. Rev. A, 61:023402, 2000.

[175] B. Wu and Q. Niu. Landau and dynamical instabilities of the superflow of bose-einstein condensates in optical lattices. Phys. Rev. A, 64:061603, 2001.

[176] H. C. Yuen and B. M. Lake. Nonlinear deep water waves: Theory and experiment. Phys. Fluids, 18(8):956–960, Aug. 1975.

[177] V. E. Zakharov and A. B. Shabat. Exact theory of two-dimensional self-focusing and one-dimensional self-modulation of waves in nonlinear media. Zh. Eksp. Teor. Fiz., 61:118, 1971.

[178] V. E. Zakharov and A. B. Shabat. Interaction between solitons in a stable medium. Zh. Eksp. Teor. Fiz., 64:1627, 1973.

[179] W. Zwerger. Mott-hubbard transition of cold atoms in optical lattices. Journal of Optics B: Quantum and Semiclassical Optics, 5(2):S9–S16, 2003.